Draft: February 16, 2026

Fragmented Aperture Antennas

Computational Design of Antenna Structure

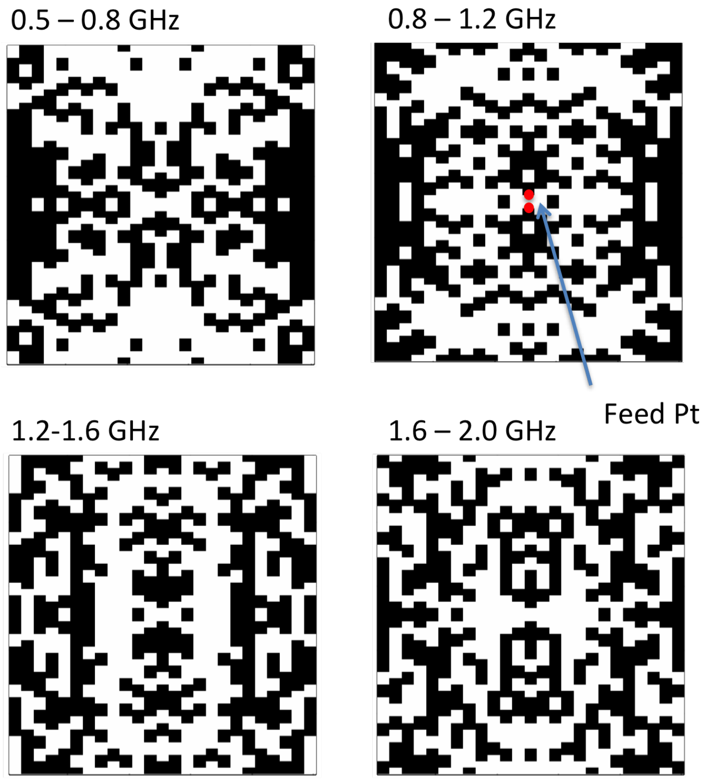

Dr. James G. Maloney

Inventor of the Fragmented Aperture Antenna

Copyright Notice and Fair Use Statement

Copyright and Permissions

This book, *Fragmented Aperture Antennas*, is provided freely for educational and research purposes. It is not sold commercially and is distributed as an open educational resource to advance knowledge in the field of computational antenna design.

Use of Published Figures and Data

This work includes figures, data, and results from previously published scientific papers to provide comprehensive documentation of the historical development and current state of fragmented aperture antenna technology. All such materials are used in accordance with established principles of fair use under U.S. Copyright Law (17 U.S.C. § 107) and international copyright conventions.

Fair Use Rationale

The use of published materials in this work satisfies the four-factor test for fair use:

1. **Purpose and Character:** This book is a non-commercial, educational work that provides scholarly analysis and historical documentation of fragmented aperture antenna technology. Materials are used to illustrate technical concepts and validate scientific claims within a transformative educational context.

2. **Nature of the Work:** Materials used are factual, scientific, and technical in nature, consisting primarily of measurement data, simulation results, and engineering diagrams from published research papers.

3. **Amount and Substantiality:** Only a small number of figures (typically 2–4) are reproduced from any single publication, representing a minor portion of the original works and only what is necessary for educational purposes.

4. **Market Effect:** This non-commercial educational work does not compete with or substitute for the original publications. Indeed, proper citation and discussion are intended to increase awareness of and citations to the original research.

Good Faith Permission Efforts

The author has made good faith efforts to contact authors and publishers of all referenced works to request permission for figure reproduction. Where permission has been explicitly granted, this is noted in the figure caption. Where permission could not be obtained after reasonable attempts, materials are included under fair use provisions as described above.

Attributions and Citations

All reproduced figures, data, and materials are accompanied by:

- Complete bibliographic citations
- Explicit attribution to all original authors
- Copyright notices as specified by publishers
- DOI or other persistent identifiers where available

These attributions serve both to comply with academic standards and to direct readers to the original sources for complete context.

Compliance and Removal Requests

The author respects the intellectual property rights of all researchers and publishers. If any copyright holder believes that material has been used inappropriately or wishes to request removal:

Contact: Dr. James G. Maloney
Email: [YOUR EMAIL ADDRESS]

Upon receiving a substantiated request, the author will promptly:

1. Review the concern in good faith
2. Remove or replace the material if appropriate
3. Provide revised versions of the book as necessary

This book is hosted on GitHub and other platforms to facilitate rapid updates in response to any concerns.

Author's Original Work

Portions of this book reproduce figures and data from the author's own previously published papers. As the original creator of this content, the author retains rights to reuse this material regardless of publication agreements. These works include:

- Maloney, J. G., et al., "Switched fragmented aperture antennas," *IEEE Antennas and Propagation Society International Symposium*, 2000.

- Maloney, J. G., et al., "A Fragmented Aperture GPS Antenna," *IEEE International Symposium on Antennas and Propagation*, 2007.
- Maloney, J. G., et al., "Wide-scan phased arrays of fragmented aperture antennas," *Proc. AMTA*, 2011.
- Maloney, J. G., et al., "Genetic algorithm analysis of a 24-bit fragmented aperture phased array," *Proc. AMTA*, 2013.

Open Educational Resource

This book is provided as an open educational resource to:

- Document the historical development of fragmented aperture technology
- Provide educational materials for students and researchers
- Advance scientific knowledge in computational antenna design
- Preserve technical knowledge for future generations

The work is distributed freely without charge and without commercial intent.

No Warranty

Acknowledgment of Copyright Holders

The author gratefully acknowledges the following publishers and their contributions to scientific knowledge:

- **IEEE** (Institute of Electrical and Electronics Engineers)
- **IET** (Institution of Engineering and Technology)
- **Electromagnetics Academy**
- **AMTA** (Antenna Measurement Techniques Association)

And the many researchers whose work is cited throughout this book. Their contributions to the field of antenna engineering have made this comprehensive reference possible.

Version: 1.0
Last Updated: February 20, 2026

This document will be updated to reflect any permission grants received after publication.

Acknowledgments: Permissions Granted

Permissions Granted

The author gratefully acknowledges the following researchers and institutions who graciously granted permission to reproduce figures from their published work:

Permissions Received

[This section will be updated as permissions are received from external researchers.]

Materials Used Under Fair Use

The following materials are used under fair use provisions (17 U.S.C. § 107) where permission could not be obtained after good faith attempts to contact authors. If any copyright holder listed below wishes to grant explicit permission retroactively, please contact the author.

[This section will list specific figures and papers used under fair use after permission attempts.]

Collaborative Spirit

These permissions, whether explicitly granted or used under fair use provisions, demonstrate the collaborative spirit of the scientific community. The author deeply appreciates the willingness of researchers to share their work for educational purposes, and hopes this book will increase awareness of and citations to their important contributions.

Contents

List of Figures

List of Tables

Dedicated to my children Kelsey, Emily, Grace and Sam.

Acknowledgements

Over the years, I have had the pleasure to work with many smart individuals who each contributed to the development of Fragmented Aperture Antennas.

For my whole career, Prof. Glenn Smith has always be a major supporter of my research efforts. Starting with teaching me how to do research during my Ph.D. thesis, to discussing many research issues over coffee during my university lab years, to co-authoring many book chapters with me, to helping invent the Fragmented Aperture, Dr Smith became a treasured collaborator and friend.

In the early years, I had the good fortune to work with one of the brightest minds, Dr. Morris Kesler. Morris was also one of the co-inventors of the Fragmented Aperture. Morris also assisted me in writing book chapters on Modeling Periodic Structures that are used in the analysis and design of phased array antennas and other periodic structures.

I had many conversations with Dr. Eric Kuster when stuck on a research topic, and his non-engineer view point was very helpful to me over the years.

I would like to thank Mr. Paul Friederich, Dr. Lon Pringle, Mr. Jim Acree for their dedicated support as project directors for both the research on Fragmented Apertures and for helping advocate for customer solutions based on Fragmented Apertures.

In the later years, the development of Fragmented Aperture solutions for many diverse applications were impacted by the assistance of Mr. Brad Baker, Mr. Kevin Cook, Dr. Doug Denison, Ms. Lynn Fountain, Mr. James Fraley, Mr. David Landgren, and Dr. Todd Lee.

The fabrication of many of the Fragmented Apertures relied heavily on the machining skills of the best machinist I ever met, Mr. Kurt Weismayer. Without Kurt's skills, many of the antennas certainly would not have been built exactly, and the measured RF performance would have been in worse agreement with the model predictions.

I also have greatly enjoyed working closely with Dr. John Schultz over the last 10+ years. Collaborating with John on many research projects has been rewarding and always a pleasure.

Lastly, I want to thank Ms. Rebecca Schultz and Dr. Kate Maloney for allowing me to assist Compass Technology Groups research efforts over the last few years. Also, I would like to thank them for their support in further developing the Fragment Aperture antenna.

Chapter 1

Introduction to Fragmented Aperture Antennas

1.1 Overview

This book describes a class of antennas called Fragmented Aperture Antennas. Unlike traditional antennas whose physical shapes are guided by analytical insight and engineering intuition, fragmented aperture antennas are designed computationally. A planar conducting surface is divided into many sub-wavelength regions, or pixels, each of which may be either conducting or non-conducting. A genetic algorithm, working in concert with a full-wave electromagnetic simulation, determines which pixels should be conducting and which should not, so as to best satisfy a given set of antenna performance requirements. The resulting antenna structures are complex, non-intuitive metallic patterns that often approach the theoretical limits of antenna performance for a given aperture size.

The fragmented aperture concept was invented in the late 1990s [1], and the term "Fragmented Aperture Antenna" was coined by the author upon visual inspection of the optimized designs, which consistently showed metallic pixels forming many connected and disconnected fragments across the aperture surface. The original concept was disclosed in U.S. Patent 6,323,809 [2]. Since then, the concept has been extended to reconfigurable antennas [3], ultra-wideband phased arrays with bandwidths exceeding 33:1 [4], and wide-scanning array designs [5]. Other research groups have successfully adopted the approach for broadband phased array element design using genetic algorithms [6] and fragmented antennas based on coupled small radiating elements [7]. Fragmented aperture antennas have been successfully designed, fabricated, and measured for a wide variety of applications spanning frequencies from UHF through millimeter wave.

This introductory chapter provides background on fundamental antenna concepts, motivates the need for a computational approach to antenna design, introduces the fragmented aperture concept, and concludes with a roadmap for the remainder of the book.

1.2 Antenna Fundamentals

An antenna is a transducer between guided electromagnetic waves, such as those on a transmission line or waveguide, and free-space electromagnetic waves that propagate away from the antenna. When used for transmission, an antenna converts a guided signal into radiation; when used for reception, it captures incident radiation and converts it into a guided signal. By the principle of reciprocity, the properties of an antenna are the same whether it is transmitting or receiving [8].

Several key parameters characterize the performance of an antenna:

1.2.1 Radiation Pattern

The radiation pattern describes the spatial distribution of electromagnetic energy radiated by an antenna as a function of direction. It is typically represented as a plot of radiated power (or field strength) versus angle, normalized to the direction of maximum radiation. Important features of the radiation pattern include the main beam (or main lobe), which is the angular region of strongest radiation; the sidelobes, which are regions of lesser radiation surrounding the main beam; and the back lobe, which is radiation in the direction opposite the main beam. The beamwidth, usually defined as the angular width between the half-power (-3 dB) points of the main beam, quantifies how directional the antenna is.

1.2.2 Directivity and Gain

Directivity is a measure of how effectively an antenna concentrates radiated energy in a particular direction compared to an isotropic radiator (a hypothetical antenna that radiates equally in all directions). The directivity D in a given direction is defined as the ratio of the radiation intensity in that direction to the radiation intensity averaged over all directions:

$$D = \frac{U(\theta, \phi)}{U_{\text{avg}}} = \frac{4\pi U(\theta, \phi)}{P_{\text{rad}}} \tag{1.1}$$

where $U(\theta, \phi)$ is the radiation intensity (power per unit solid angle) and P_{rad} is the total radiated power.

Gain is closely related to directivity but also accounts for losses within the antenna. The gain G is related to the directivity D by the radiation efficiency η:

$$G = \eta\, D \tag{1.2}$$

where η accounts for ohmic and dielectric losses in the antenna structure.

In practice, it is often useful to work with the *realized gain*, which further accounts for impedance mismatch between the antenna and its feed:

$$G_{\text{realized}} = (1 - |\Gamma|^2)\, G \tag{1.3}$$

where Γ is the voltage reflection coefficient at the antenna terminals. The realized gain captures the overall effectiveness of the antenna in converting guided-wave power into radiation in a given direction.

1.2.3 Aperture and Aperture Efficiency

A fundamental result in antenna theory relates the maximum achievable gain of an antenna to its physical aperture area A:

$$G_{\text{max}} = \frac{4\pi A}{\lambda^2} \tag{1.4}$$

where λ is the free-space wavelength. This result applies to a uniformly illuminated aperture radiating into one hemisphere (i.e., with a ground plane or reflector behind it). For an aperture that radiates equally into both hemispheres (no ground plane), the limit becomes $2\pi A/\lambda^2$.

The aperture efficiency η_a describes how closely an antenna approaches this theoretical limit:

$$\eta_a = \frac{G}{G_{\text{max}}} = \frac{G\lambda^2}{4\pi A} \tag{1.5}$$

Traditional antenna designs rarely achieve aperture efficiencies above 50–70$\%$. As will be shown throughout this book, fragmented aperture antennas routinely approach the theoretical aperture gain limit, often achieving efficiencies that exceed those of conventional designs.

1.2.4 Bandwidth

Every antenna has a finite bandwidth over which it operates satisfactorily. Bandwidth may be defined in terms of several criteria, but the most common is the impedance bandwidth: the range of frequencies over which the antenna maintains an acceptable impedance match to its feed line. A common threshold is a voltage standing wave ratio (VSWR) of 2:1, corresponding to a return loss of approximately 10 dB, meaning that no more than 10$\%$ of the incident power is reflected back to the source. More demanding applications may require a VSWR below 1.5:1 (return loss better than 14 dB) or even 1.3:1.

Bandwidth can be expressed as a ratio of the upper to lower frequency limits (e.g., 10:1 bandwidth for an antenna operating from 1 to 10 GHz) or as a fractional bandwidth:

$$\text{BW}_{\text{frac}} = \frac{f_H - f_L}{f_c} \tag{1.6}$$

where f_H and f_L are the upper and lower frequency limits and f_c is the center frequency. Antennas with bandwidths of 2:1 or greater are often called wideband, while those exceeding roughly 10:1 are called ultra-wideband.

Achieving wide bandwidth while maintaining high gain and an acceptable impedance match is one of the central challenges in antenna design and a particular strength of the fragmented aperture approach.

1.2.5 Polarization

The polarization of an antenna describes the orientation of the electric field vector of the radiated wave. Common polarizations include linear (vertical or horizontal), circular (right-hand or left-hand), and elliptical. The polarization of the radiated field is determined by the currents flowing on the antenna structure, and achieving a desired polarization is an important design goal. Fragmented aperture antennas can be designed for any of these polarizations, including cases where the polarization varies with beam direction.

1.3 Antenna Arrays

A single antenna element has a radiation pattern determined by its geometry and size. To achieve higher gain, narrower beams, or the ability to steer the beam electronically, multiple antenna elements are arranged in an array. In an array, the signals from the individual elements combine coherently, and the resulting radiation pattern is the product of the individual element pattern and the array factor, which depends on the element spacing, number of elements, and the relative amplitude and phase of the excitation at each element.

Electronic beam steering is accomplished by adjusting the relative phases of the signals at each element. This is the basis of the phased array, which can rapidly redirect its beam without physically moving the antenna. Phased arrays are essential in modern radar, communications, and electronic warfare systems.

However, the design of wideband phased arrays presents significant challenges. Mutual coupling between array elements—the electromagnetic interaction between neighboring elements—can cause scan blindness, a condition where the array is poorly matched at certain combinations of frequency and scan angle. Traditional array design approaches attempt to minimize mutual coupling, but as will be shown in this book, the fragmented aperture approach embraces mutual coupling, and in some cases exploits direct electrical connections between elements to achieve bandwidths that far exceed those of conventional array elements.

1.4 Limitations of Traditional Antenna Design

Traditional antenna design relies on a library of known antenna types—dipoles, patches, horns, spirals, log-periodic structures, and others—each with well-understood behavior that can be predicted analytically or with simple numerical models. The designer selects an antenna type appropriate for the application and then adjusts a relatively small number of geometric parameters (lengths, widths, feed positions, spacings) to optimize performance.

This approach has been enormously successful and has produced the antenna designs in widespread use today. However, it is inherently constrained by the set of geometries that have been studied and understood. The designer is limited to exploring variations within known antenna topologies. The number of degrees of freedom available for optimization is small—typically fewer than a dozen parameters—and the design space is correspondingly limited.

Consider, by contrast, an antenna aperture divided into a grid of 200 sub-wavelength pixels, each of which may be independently set to conducting or non-conducting. This seemingly simple description defines a design space of $2^{200} \approx 10^{60}$ possible antenna geometries. The vast majority of these configurations have never been conceived by any antenna designer, and many of them produce antenna characteristics that are unlike any known antenna type. The challenge, of course, is finding the configurations that produce useful antennas among this enormous number of possibilities.

This is precisely the challenge that the fragmented aperture design approach addresses.

1.5 The Fragmented Aperture Concept

The fragmented aperture antenna design approach combines three essential elements:

1. **A pixelated aperture.** The antenna surface is divided into a grid of sub-wavelength regions, or pixels. Each pixel is assigned a binary state: conducting (metal) or non-conducting (absent). The set of all pixel states defines the antenna geometry. Early fragmented apertures used rectangular pixels on a rectilinear grid, but as described in Chapter 3, improved pixel shapes and lattice geometries have been developed to address fabrication challenges.

2. **A full-wave electromagnetic simulation.** A rigorous numerical solution of Maxwell's equations is used to predict the antenna performance for any given pixel configuration. The finite-difference time-domain (FDTD) method has been used exclusively in the author's work because a single time-domain simulation efficiently produces antenna characteristics across the entire frequency band of interest. A detailed description of the FDTD method as applied to antennas is provided in Appendix A.

3. **An evolutionary optimization algorithm.** Because the design space is far too large for exhaustive search, a genetic algorithm (GA) is used to efficiently explore the space of possible pixel configurations. The GA maintains a population of candidate antenna designs, evaluates each design using the FDTD simulation, and evolves the population over many generations using selection, crossover, and mutation operations. The algorithm converges toward designs that best satisfy the specified performance goals.

The result of this design process is an antenna whose physical structure has been computationally optimized to meet a particular set of performance requirements. The antenna shapes that emerge from this process are invariably complex and non-intuitive. Inspection of the metallic regions on the aperture reveals many interconnected and isolated fragments of conductor—hence the name *fragmented aperture*.

A critical advantage of this approach is that the full-wave simulation captures all of the relevant physics: mutual coupling, surface wave effects, feed interactions, dielectric loading, and diffraction from edges and discontinuities. The optimizer therefore has access to the true electromagnetic behavior of each candidate design, not an approximate or simplified model. This is what allows fragmented aperture designs to routinely approach theoretical performance limits.

1.6 Novelty and Significance

The fragmented aperture antenna represents a fundamentally different philosophy of antenna design. Rather than starting from an analytical understanding of how a particular geometric shape radiates and then perturbing that shape to improve performance, the fragmented aperture approach starts from a general description of the design space (the set of all possible pixel configurations) and uses computation to discover structures that meet the desired specifications. In this sense, the antenna structure itself is the output of the design process, not the input.

This computational approach to designing antenna structure has produced several notable results:

- Single-element fragmented aperture antennas that approach the theoretical aperture gain limit $2\pi A/\lambda^2$ for apertures without a ground plane, across bandwidths exceeding an octave.
- Reconfigurable fragmented aperture antennas (Agile Aperture Antennas) that can electronically switch between different operating modes—changing beam direction, bandwidth, or polarization—by opening and closing switched links between metallic pads.
- Ultra-wideband phased array elements based on the fragmented aperture concept that achieve bandwidths of 33:1, with preliminary work suggesting that 100:1 bandwidths are achievable. A key insight enabling these designs was that electrical connections between array elements should be exploited rather than avoided.
- Improved pixel geometries that eliminate the fabrication issue of "diagonal touching"—a problem that plagued early fragmented aperture designs and caused poor agreement between modeled and measured antenna performance.
- An improved mutation algorithm for the genetic algorithm that significantly accelerates convergence for designs with large numbers of pixels.

These results, and others, are described in detail in the chapters that follow.

1.7 Organization of the Book

The remainder of this book is organized as follows:

Chapter 2: Original Approach to Design Fragmented Apertures. This chapter describes the original fragmented aperture concept as disclosed in U.S. Patent 6,323,809. The genetic algorithm design approach is presented, along with early design results that demonstrated the viability of the concept.

Chapter 3: Improved Approach to Design Fragmented Apertures. The original fragmented aperture approach suffered from the problem of diagonal touching, where pixels that touch only at corners lead to fabrication difficulties and poor model-measurement agreement. This chapter presents three improved pixel geometries that inherently avoid diagonal touching, along with an improved mutation algorithm that accelerates the convergence of the genetic algorithm for designs with many pixels.

Chapter 4: Sample Antenna Designs. This chapter presents a gallery of fragmented aperture antenna designs that illustrate the versatility of the approach. Topics include various feed strategies, bandwidth tailoring, fixed beam steering, polarization control (linear and circular), beamwidth tailoring, and out-of-band rejection.

Chapter 5: Reconfigurable Fragmented Aperture Antennas. This chapter describes the Agile Aperture Antenna, a reconfigurable antenna in which switched links between metallic pads allow the antenna to be electronically reconfigured to meet different performance specifications. Static and reconfigurable proof-of-concept designs are presented with measured results.

Chapter 6: Fragmented Array Elements. This chapter extends the fragmented aperture concept to the design of individual elements for phased array antennas. The approach for incorporating scan performance into the design process is described, and example designs spanning multiple octaves of bandwidth are presented.

Chapter 7: Wideband Antenna Arrays. This chapter describes the development of ultra-wideband phased arrays using fragmented aperture design principles. Key innovations include connected arrays, broadband screen backplanes using resistive card layers to mitigate ground-plane nulls, and multi-layer radiators for improved front-to-back ratio. Measured results for arrays with bandwidths up to 33:1 are presented.

Chapter 8: Designing Wide Scan Fragmented Array Antennas. This chapter describes techniques for designing fragmented aperture array elements with wide scan volumes ($\pm 60^\circ$ and beyond) using spectral-domain FDTD simulation within the genetic algorithm design process. A laminated printed circuit board fabrication approach is presented, and results for a whole X-band (8–12 GHz) array element are shown.

Chapter 9: Reconfigurable Arrays. This chapter describes reconfigurable phased array antennas that combine the fragmented aperture design approach with electronic reconfiguration, enabling improved scan performance and dynamic polarization control.

Appendix A: Computational Modeling of Antennas. This appendix provides a self-contained introduction to the finite-difference time-domain (FDTD) method as applied to antenna analysis. The basic algorithm is described, the formulation for both transmitting and receiving antennas is presented, and several examples are provided to illustrate the accuracy and utility of the method.

References

[1] J. G. Maloney, M. P. Kesler, P. H. Harms, T. L. Fountain, and G. S. Smith, "The fragmented aperture antenna: FDTD analysis and measurement," in *Millennium Conference on Antennas and Propagation (AP 2000)*, 2000, p. 93.

[2] J. G. Maloney, M. P. Kesler, P. H. Harms, and G. S. Smith, "Fragmented aperture antennas and broadband ground planes," U.S. Patent No. 6,323,809 B1, Nov. 2001.

[3] L. N. Pringle, P. H. Harms, S. P. Blalock, G. N. Kiesel, E. J. Kuster, P. G. Friederich, R. J. Prado, J. M. Morris, and G. S. Smith, "A reconfigurable aperture antenna based on switched links between electrically small metallic patches," *IEEE Transactions on Antennas and Propagation*, vol. 52, no. 6, pp. 1434–1445, Jun. 2004.

[4] D. Landgren, T. Brunasso, K. Allen, D. Dykes, J. Kovitz, J. Perez, J. Dee, J. Marsh, C. Hunter, and G. Smith, “A broadband array with unbalanced feeds : Elements and power combiners based on the fragmented aperture principle,” in *2019 IEEE International Symposium on Antennas and Propagation and USNC-URSI Radio Science Meeting*, 2019, pp. 1223–1224.

[5] J. G. Maloney, B. N. Baker, R. T. Lee, G. N. Kiesel, and J. J. Acree, “Wide scan, integrated printed circuit board, fragmented aperture array antennas,” in *2011 IEEE International Symposium on Antennas and Propagation (APSURSI)*, 2011, pp. 1965–1968.

[6] B. Thors, H. Steyskal, and H. Holter, “Broad-band fragmented aperture phased array element design using genetic algorithms,” *IEEE Transactions on Antennas and Propagation*, vol. 53, no. 10, pp. 3280–3287, 2005.

[7] N. Barani, J. F. Harvey, and K. Sarabandi, “Fragmented antenna realization using coupled small radiating elements,” *IEEE Transactions on Antennas and Propagation*, vol. 66, no. 4, pp. 1725–1735, 2018.

[8] IEEE, “Ieee standard for definitions of terms for antennas,” Institute of Electrical and Electronics Engineers, Tech. Rep. IEEE Std 145-2013, 2013.

Chapter 2

Original Approach to Design Fragmented Apertures

2.1 Aperture Utilization

A central goal in antenna design is to make effective use of the available aperture area. As discussed in Chapter 1, the theoretical maximum gain for a uniformly illuminated planar aperture of area A radiating into one hemisphere is $4\pi A/\lambda^2$, and for an aperture radiating into both hemispheres (no ground plane), the limit is $2\pi A/\lambda^2$. Traditional antenna designs—dipoles, patches, spirals, and the like—typically utilize only a fraction of the available aperture area at any given frequency. For example, a spiral antenna uses an "active region" whose size scales with frequency; at any given operating frequency, much of the physical aperture is not contributing to the radiation.

The original fragmented aperture concept was motivated by a simple question: *can one design a planar antenna that utilizes the entire aperture area across a wide frequency band, thereby approaching the theoretical gain limit?* The answer, as demonstrated in this chapter, is yes—provided one is willing to abandon traditional antenna geometries in favor of computationally optimized structures.

2.2 Original Genetic Design Approach

2.2.1 Binary Encoding of Antenna Geometry

The fundamental idea behind the fragmented aperture antenna is to represent the antenna geometry as a binary string that can be manipulated by an evolutionary optimization algorithm. The antenna surface is divided into a grid of sub-wavelength rectangular pixels, as illustrated in Figure 2.1. Each pixel is assigned a single binary value: 1 for conducting (metal present) and 0 for non-conducting (metal absent). The collection of all pixel states defines the antenna geometry and constitutes the "genetic code" of the antenna.

This binary representation maps naturally onto a genetic algorithm (GA). The

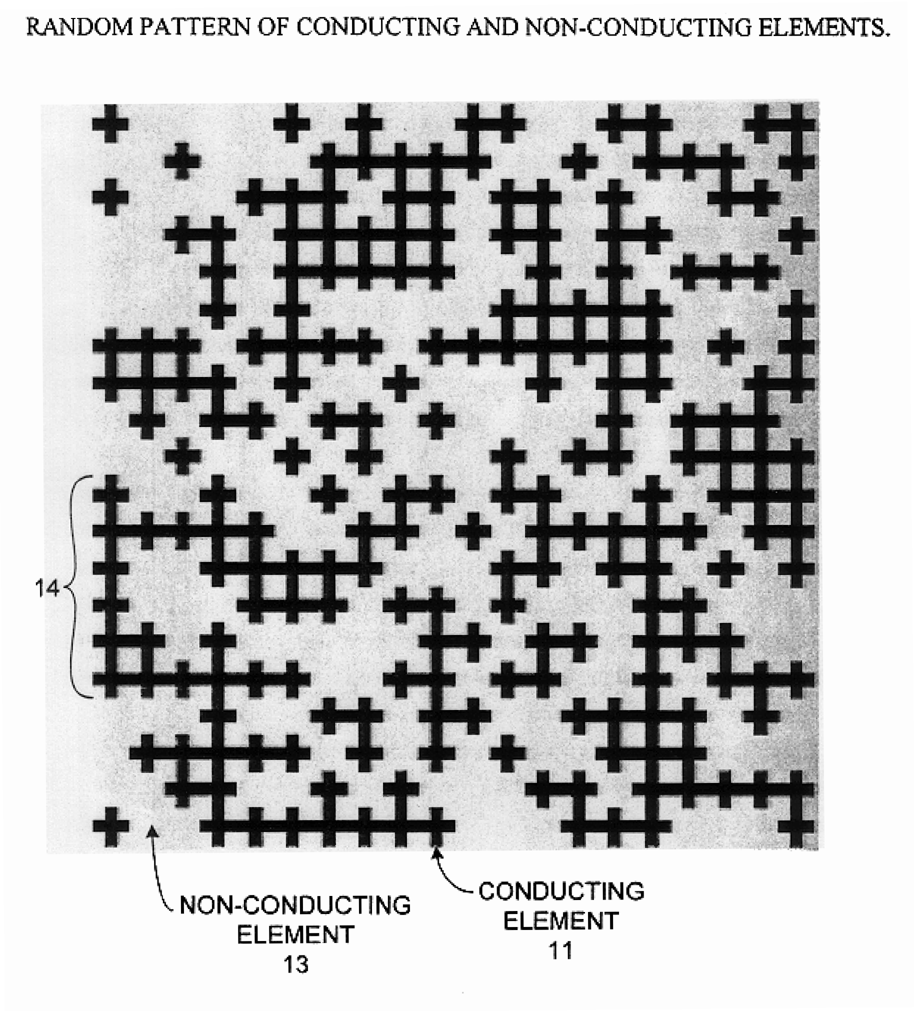

Figure 2.1: The fragmented aperture concept: a planar surface divided into a grid of sub-wavelength pixels, each either conducting (black) or non-conducting (white). The pattern of conducting and non-conducting elements defines the antenna geometry [1].

GA maintains a population of candidate antenna designs, each represented by a binary string. Over successive generations, the population evolves toward better antenna designs through the standard genetic operations of selection, crossover, and mutation.

2.2.2 Two-Stage Optimization

The original design process employed a two-stage optimization approach, as illustrated in Figure 2.2. In the first stage, the aperture area is described using a relatively small number of trapezoidal conducting strips arranged symmetrically about a coaxial feed point. Each strip has a variable length that is encoded in the binary representation. This coarse description of the antenna geometry allows the GA to quickly explore the design space and identify promising regions.

In the second stage, the best design from the first stage is converted to the full pixel representation and the GA continues to optimize at the pixel level, refining the antenna geometry to improve performance. The flowchart for this second stage is shown in Figure 2.3.

2.2.3 Fitness Evaluation with FDTD

At each generation of the GA, every candidate antenna in the population must be evaluated to determine how well it meets the design objectives. This evaluation requires a full-wave electromagnetic simulation of each candidate antenna. The finite-difference time-domain (FDTD) method was used exclusively for this purpose because a single time-domain simulation produces the antenna response across the entire frequency band of interest via Fourier transformation (see Appendix A for details).

The fitness function used to evaluate each candidate antenna was typically based on the broadside realized gain across the design bandwidth. Designs that achieved good impedance match (low VSWR) and high broadside gain over the specified frequency range received higher fitness scores. The GA then preferentially selected high-fitness individuals for reproduction, driving the population toward better antenna designs over successive generations.

Even with the efficiency of the FDTD method, the computational cost of evaluating hundreds or thousands of candidate antennas over many GA generations was substantial. This was one of the earliest applications of large-scale parallel computing to antenna design, with populations of antennas evaluated simultaneously on clusters of workstations.

2.2.4 Symmetry Constraints

To reduce the size of the design space and to ensure that the resulting antenna designs had desirable radiation characteristics, symmetry constraints were typically imposed during the optimization. For a vertically polarized broadside antenna, left-right and top-bottom symmetry were enforced, reducing the number of independent pixels (and hence the length of the binary string) by a factor of four. For example, an aperture with 400 pixels and both symmetries enforced has only 100 independent degrees of freedom, corresponding to a design space of 2^{100} possible configurations—still enormous, but

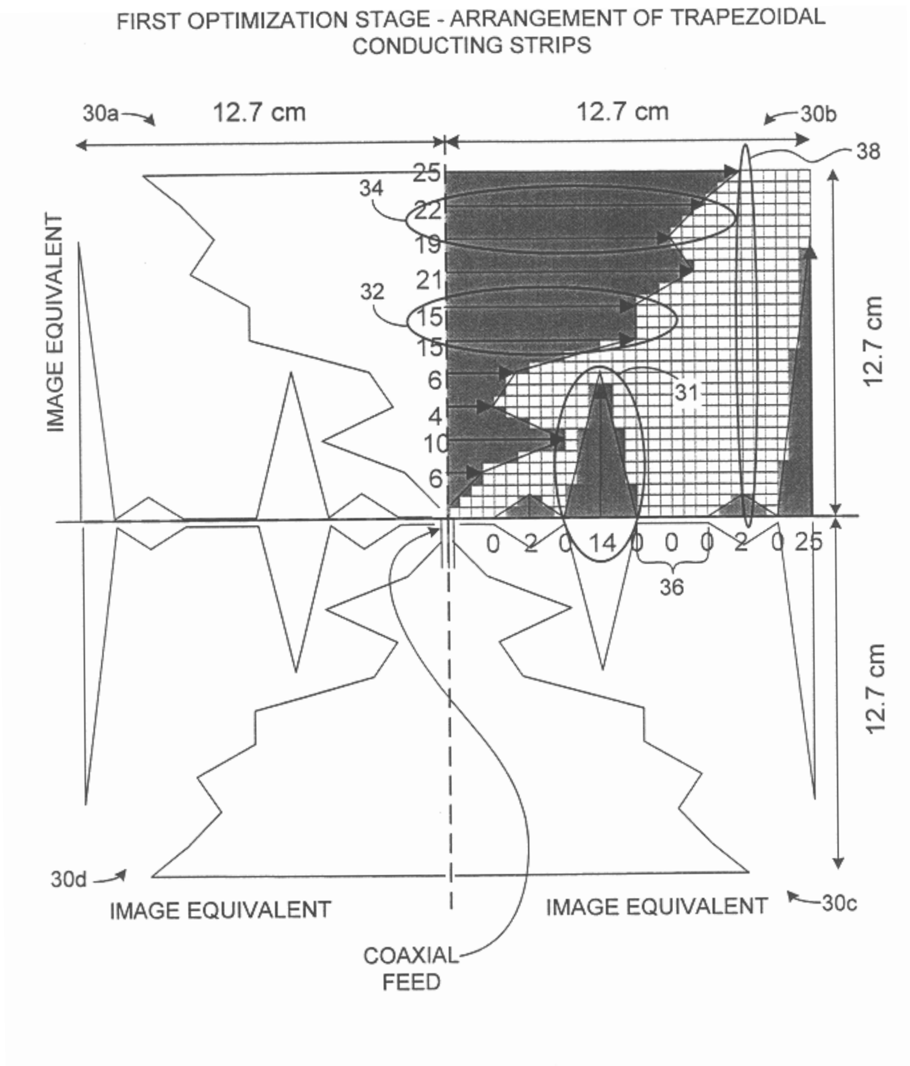

Figure 2.2: First optimization stage: the aperture is described using trapezoidal conducting strips of variable length arranged about a coaxial feed. This coarse parameterization enables rapid exploration of the design space [1].

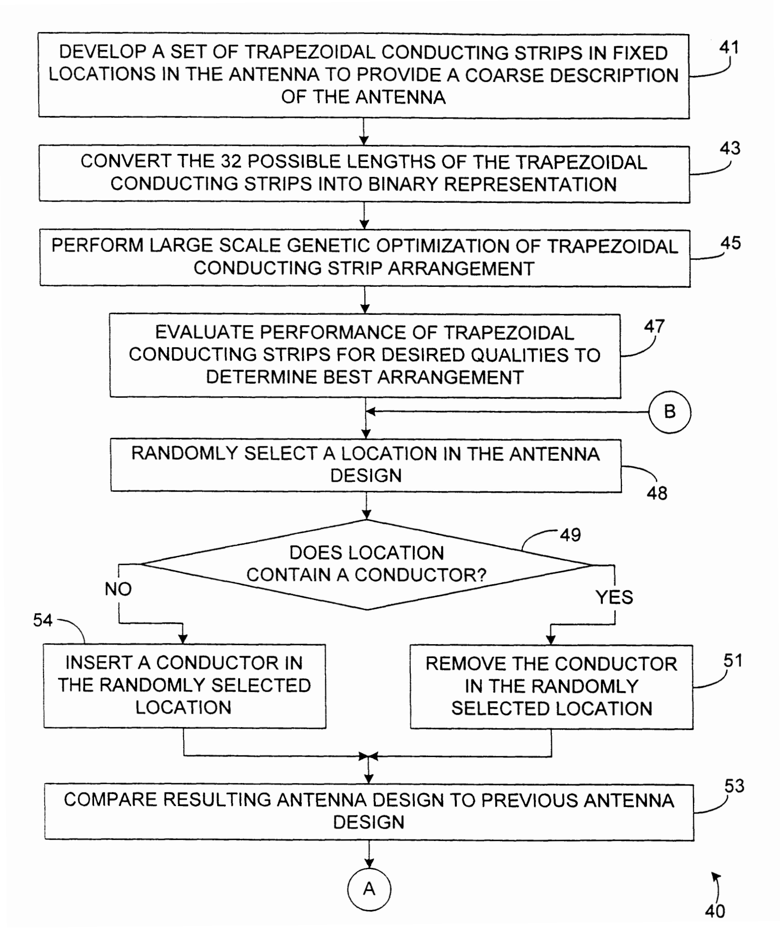

Figure 2.3: Flowchart of the genetic optimization process for fragmented aperture design. The algorithm iteratively toggles pixels between conducting and non-conducting states, evaluating the antenna performance at each step using full-wave electromagnetic simulation [1].

significantly more tractable for the GA.

2.3 First Success

The first successful fragmented aperture antenna design was a planar aperture optimized to operate from 800 MHz to 2.5 GHz (a bandwidth of approximately 3:1). The aperture was 10 inches $\times$ 10 inches (25.4 cm $\times$ 25.4 cm) and was excited at a feed point near the center of the aperture. The optimized design is shown in Figure 2.4.

The visual complexity of the design in Figure 2.4 is striking. The conducting regions form an intricate pattern of connected and disconnected fragments that bears no resemblance to any traditional antenna geometry. It was this visual character—the many fragments of conductor scattered across the aperture—that led to the name "Fragmented Aperture Antenna."

Despite the non-intuitive appearance of the design, the measured performance was excellent. Figure 2.5 compares the measured broadside gain with the FDTD prediction and with two reference curves: the uniform aperture gain limit ($2\pi A/\lambda^2$, since there is no ground plane) and the gain of a spiral antenna of the same aperture size.

Several important observations can be drawn from Figure 2.5:

- Within the optimization range of 800 MHz to 2.5 GHz, the fragmented aperture closely approaches the uniform aperture gain limit. This demonstrates that the GA/FDTD design process is effective at utilizing the full aperture area.
- The measured and FDTD-predicted gains are in excellent agreement across the entire frequency range, validating the accuracy of the FDTD model used in the design process.
- The fragmented aperture significantly outperforms a spiral antenna of the same physical aperture size. The spiral, being a traveling-wave antenna with a frequency-dependent active region, does not utilize the full aperture at any given frequency.
- Outside the optimization range, the antenna performance degrades, as expected. The GA optimized the design specifically for the 800 MHz to 2.5 GHz band, and performance outside this band was not part of the fitness function.

2.4 Bidirectional Radiation

Because the first fragmented aperture antennas were single-layer planar structures with no ground plane, they radiated into both hemispheres. Figure 2.6 shows the H-plane radiation pattern of the first successful design, comparing the FDTD prediction with the measured pattern.

The bidirectional radiation pattern is clearly visible in Figure 2.6, with the antenna producing roughly equal radiation in the forward and backward directions. The model-measurement agreement is again excellent. This bidirectional behavior is a natural consequence of the single-layer planar geometry: since the antenna structure is symmetric about the plane of the aperture (to within the thickness of the conductor), there is no physical mechanism to preferentially direct radiation into one hemisphere.

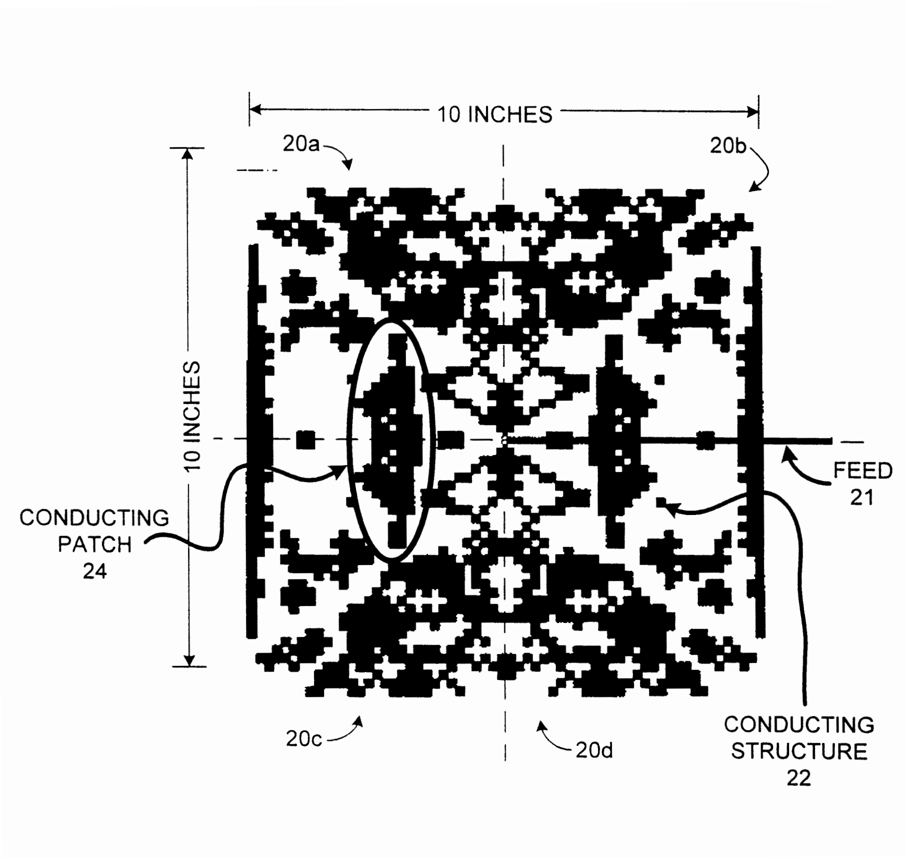

Figure 2.4: The first successful fragmented aperture antenna: a 10-inch × 10-inch aperture optimized for 800 MHz to 2.5 GHz. The complex pattern of conducting (black) and non-conducting (white) regions was determined entirely by the genetic algorithm and FDTD simulation. The feed is located at the right side of the aperture. Left-right and top-bottom symmetry lines are indicated by the dashed lines [1].

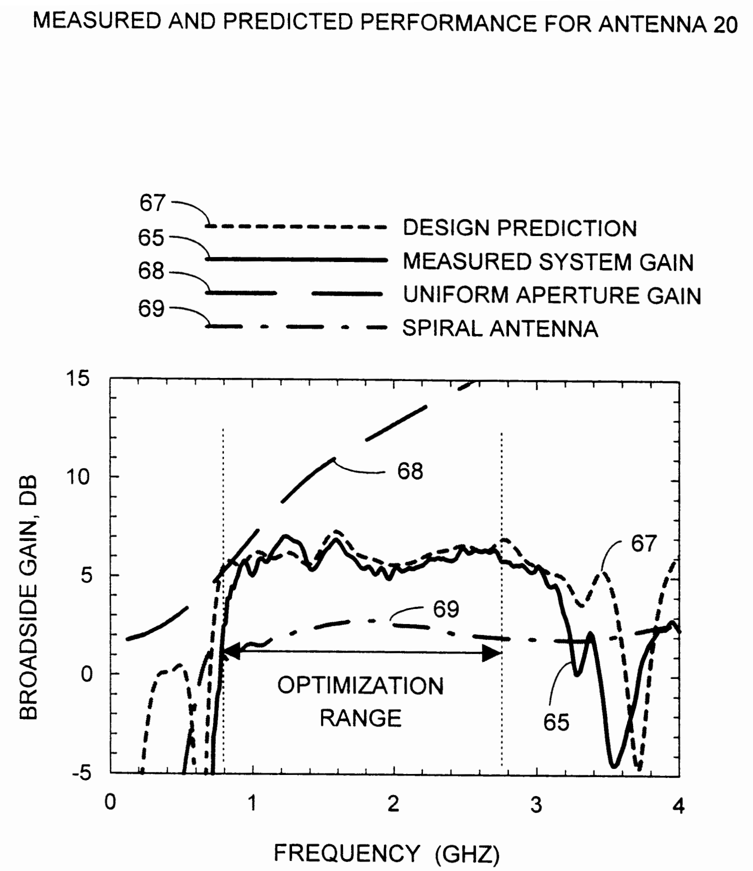

Figure 2.5: Measured and predicted broadside gain for the first fragmented aperture antenna (Figure 2.4). The fragmented design closely approaches the uniform aperture gain limit across the 800 MHz to 2.5 GHz optimization range, and significantly outperforms a spiral antenna of the same aperture size. The measured and FDTD-predicted gains are in excellent agreement [1].

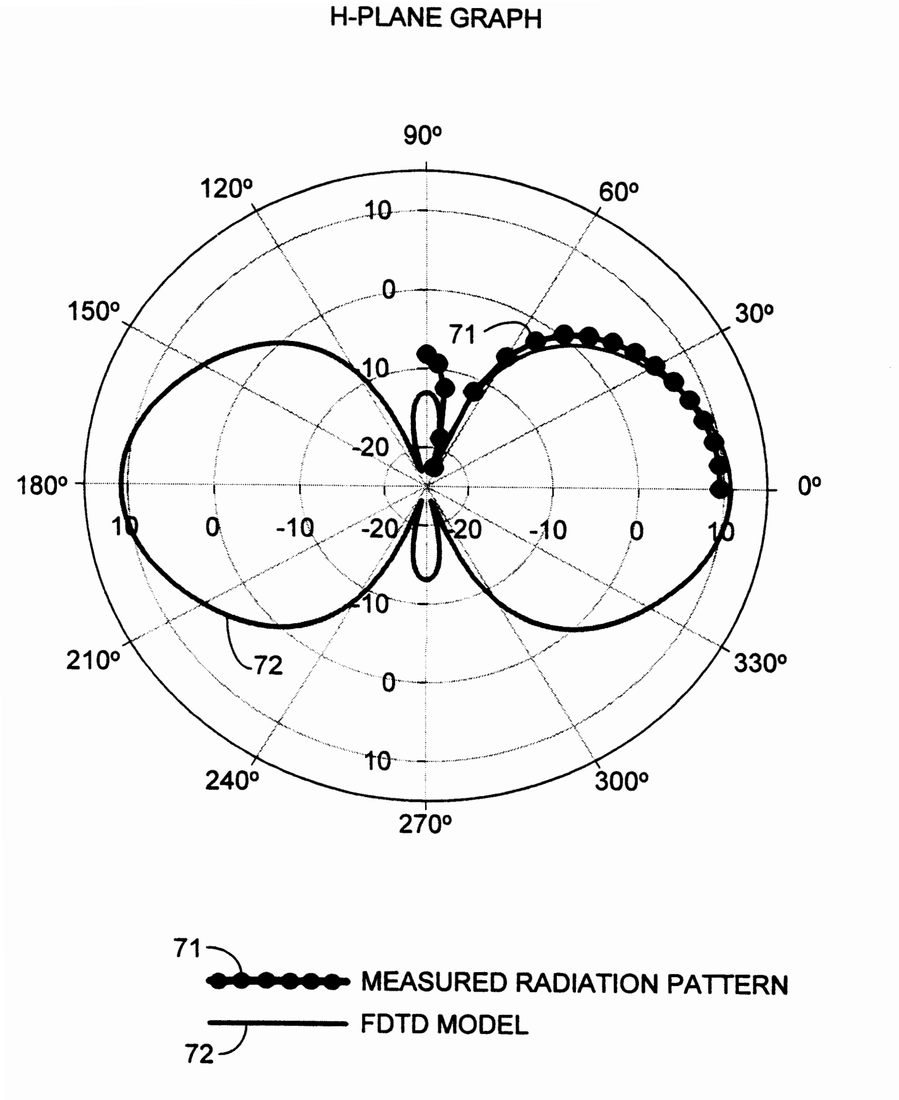

Figure 2.6: H-plane radiation pattern of the first fragmented aperture antenna, comparing the measured pattern with the FDTD model prediction. The pattern is clearly bidirectional, with roughly equal radiation into the forward and backward hemispheres [1].

For many applications, bidirectional radiation is undesirable—half of the radiated power is directed away from the intended coverage area. This motivates the use of a ground plane behind the aperture. However, as will be discussed in detail in Chapter 7, a simple conducting ground plane introduces half-wave nulls at frequencies where the aperture-to-ground-plane spacing is an integer multiple of $\lambda/2$. Addressing this challenge led to the development of broadband screen backplanes and multi-layer radiating structures that are key features of the wideband fragmented array designs.

2.5 Fragmented Broadband Ground Planes

An interesting early application of the fragmented aperture concept was the design of broadband ground planes. Just as the pixel pattern on the radiating aperture can be optimized to achieve desired antenna characteristics, the pixel pattern on a surface behind the aperture can be optimized to function as a broadband ground plane.

A conventional conducting ground plane placed a quarter wavelength behind a radiating aperture provides constructive interference at the design frequency: the backward-radiated wave reflects off the ground plane and, after traveling an additional half wavelength (round trip), arrives back at the aperture in phase with the forward-radiated wave. However, this constructive interference is inherently narrowband.

By replacing the solid conducting ground plane with a fragmented surface—a pixelated pattern of conducting and non-conducting regions—it is possible to design a reflector that provides a more uniform phase response over a wider bandwidth. Figure 2.7 shows the transmission phase through a fragmented surface compared with a reference.

This early exploration of fragmented ground planes laid the groundwork for the more sophisticated broadband screen backplane designs described in Chapter 7, which use resistive card (r-card) layers in combination with a conducting ground plane to achieve wideband operation.

2.6 The Original Patent and Early Publications

The original fragmented aperture antenna concept, including both the radiating aperture and the broadband ground plane, was disclosed in U.S. Patent 6,323,809, "Fragmented Aperture Antennas and Broadband Ground Planes," granted November 27, 2001 [1]. The inventors were J. G. Maloney, M. P. Kesler, P. H. Harms, and G. S. Smith.

The first public presentation of the fragmented aperture concept occurred at the ICAP/JINA Conference on Antennas and Propagation in 2000 [2]. The reconfigurable version of the concept (switched fragmented apertures) was presented at the IEEE Antennas and Propagation Symposium later that same year [3]. The concept was subsequently described in a number of conference papers and symposium presentations [4], and was included as part of a chapter on wideband arrays in the Modern Antenna Handbook [5].

Since the original publications, several other research groups have independently adopted the fragmented aperture design approach for their own applications. Herscovici et al. applied the concept to aperture-coupled microstrip antennas [6]. Thors et al. used

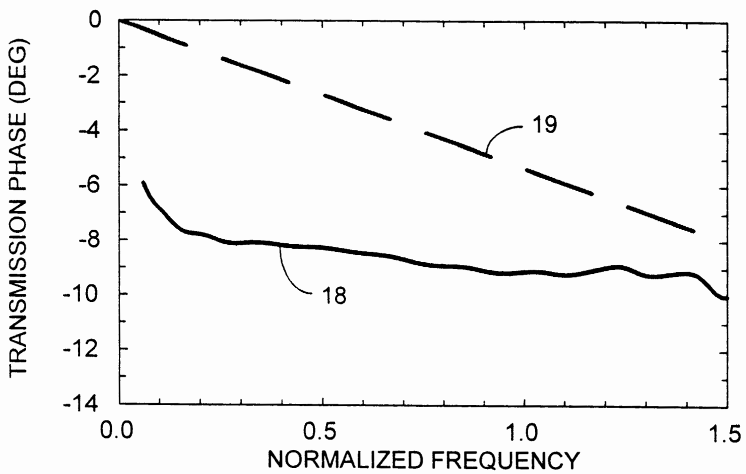

Figure 2.7: Transmission phase comparison demonstrating the broadband properties of a fragmented surface [1].

genetic algorithms for broadband fragmented aperture phased array element design [7]. Ellgardt and Persson investigated wide-angle scanning fragmented aperture arrays [8]. More recent work has explored fragmented antennas based on coupled small radiating elements [9] and optimized designs with integrated baluns [10]. These and other efforts confirm the broad applicability of the fragmented aperture design philosophy.

2.7 Lessons Learned

The success of the original fragmented aperture antenna validated the fundamental premise that computational optimization could discover antenna geometries far beyond those accessible through traditional design approaches. However, the early work also revealed important limitations that would drive subsequent research:

- **Diagonal touching.** The original rectangular pixel geometry led to situations where conducting pixels touched only at their corners. In the FDTD simulation, these diagonally touching pixels are always electrically connected, but when fabricated (e.g., by printed circuit board etching), the connection is unreliable. This issue, and the solutions to it, are the subject of Chapter 3.

- **Convergence for large pixel counts.** As the number of pixels increased beyond approximately 100, the standard GA mutation operator became increasingly ineffective at exploring the design space. An improved mutation strategy tailored for fragmented apertures is described in Chapter 3.

- **Bidirectional radiation.** Single-layer fragmented apertures without a ground plane radiate equally into both hemispheres, limiting the achievable gain to $2\pi A/\lambda^2$. Addressing this limitation motivated the development of broadband backplanes (Chapter 7) and multi-layer radiating structures (Chapter 7).

- **Fixed designs.** Once fabricated, a fragmented aperture antenna operates with a single set of characteristics. The desire for antennas that could dynamically change their operating characteristics led to the development of reconfigurable fragmented apertures (Chapter 5).

Despite these limitations, the original fragmented aperture concept established a powerful new paradigm for antenna design: one in which the physical structure of the antenna is determined by computation rather than by analytical insight alone. The remaining chapters of this book describe how this paradigm has been extended and refined to address an increasingly wide range of antenna design challenges.

References

[1] J. G. Maloney, M. P. Kesler, P. H. Harms, and G. S. Smith, “Fragmented aperture antennas and broadband ground planes,” U.S. Patent No. 6,323,809 B1, Nov. 2001.

[2] J. G. Maloney, M. P. Kesler, P. H. Harms, T. L. Fountain, and G. S. Smith, "The fragmented aperture antenna: FDTD analysis and measurement," in *Millennium Conference on Antennas and Propagation (AP 2000)*, 2000, p. 93.

[3] J. G. Maloney, M. P. Kesler, L. M. Lust, L. N. Pringle, T. L. Fountain, and P. H. Harms, "Switched fragmented aperture antennas," in *IEEE Antennas and Propagation Society International Symposium*, Salt Lake City, UT, Jul. 2000, pp. 310–313.

[4] P. Friederich, L. Pringle, L. Fountain, P. Harms, D. Denison, E. Kuster, S. Blalock, G. Smith, J. Maloney, and M. Kesler, "A new class of broadband planar apertures," in *Antenna Applications Symposium*, Sep. 2001, pp. 561–587.

[5] W. Croswell, T. Durham, M. Jones, D. Schaubert, P. G. Friederich, and J. G. Maloney, "Wideband arrays," in *Modern Antenna Handbook*, C. A. Balanis, Ed. John Wiley & Sons, 2011, ch. 12.

[6] N. Herscovici, J. Ginn, T. Donisi, and B. Tomasic, "A fragmented aperture-coupled microstrip antenna," in *IEEE Antennas and Propagation Society International Symposium*, Jul. 2008, pp. 1–4.

[7] B. Thors, H. Steyskal, and H. Holter, "Broad-band fragmented aperture phased array element design using genetic algorithms," *IEEE Transactions on Antennas and Propagation*, vol. 53, no. 10, pp. 3280–3287, 2005.

[8] A. Ellgardt and P. Persson, "Characteristics of a broad-band wide-scan fragmented aperture phased array antenna," in *2006 First European Conference on Antennas and Propagation*, 2006, pp. 1–5.

[9] N. Barani, J. F. Harvey, and K. Sarabandi, "Fragmented antenna realization using coupled small radiating elements," *IEEE Transactions on Antennas and Propagation*, vol. 66, no. 4, pp. 1725–1735, 2018.

[10] Y. Zang, M. Jin, and X. Jiao, "The optimum design of a 3-10ghz linear-polarized fragmented aperture array with integrated balun," in *2019 International Symposium on Antennas and Propagation (ISAP)*, 2019, pp. 1–3.

Chapter 3

Improved Approach to Design Fragmented Apertures

3.1 Overview

In the late 1990s, Maloney et al. began investigating the design of highly pixelated apertures whose physical shape and structure are optimized using genetic algorithms (GA) and full-wave computational electromagnetic simulation (FDTD) to best meet a required antenna performance specification—gain, bandwidth, polarization, pattern, and so on [1]–[2]. Visual inspection of the optimized designs revealed that the metallic pixels formed many connected and disconnected fragments across the aperture, which led to the name *Fragmented Aperture Antennas* for this new class of antennas. A detailed description of the original design approach is disclosed in the original patent [3]. Since the original publications, other research groups have successfully applied the fragmented aperture design approach to their own applications [4]–[5], including the use of genetic algorithms for broadband fragmented aperture phased array design [6] and the development of fragmented antennas based on coupled small radiating elements [7].

However, the original fragmented design approach suffers from two significant deficiencies. First, the placement of pixels on a generalized rectilinear grid leads to the problem of *diagonal touching*—pixels that share only a corner vertex are electrically connected in the numerical model but may be disconnected when fabricated. Other research groups have also encountered this diagonal touching problem [8]. Second, the convergence of the GA becomes increasingly poor as the pixel count grows large ($\gg$ 100). Recent work has explored various optimization strategies to address convergence challenges, including the use of integrated baluns to simplify the design space [9] and automated optimization techniques [10].

This chapter presents solutions to both of these shortcomings. First, alternate approaches to the discretization of the aperture area that inherently avoid diagonal touching are presented. Second, an improved mutation operator tailored for fragmented aperture design that significantly improves convergence for large pixel counts is introduced.

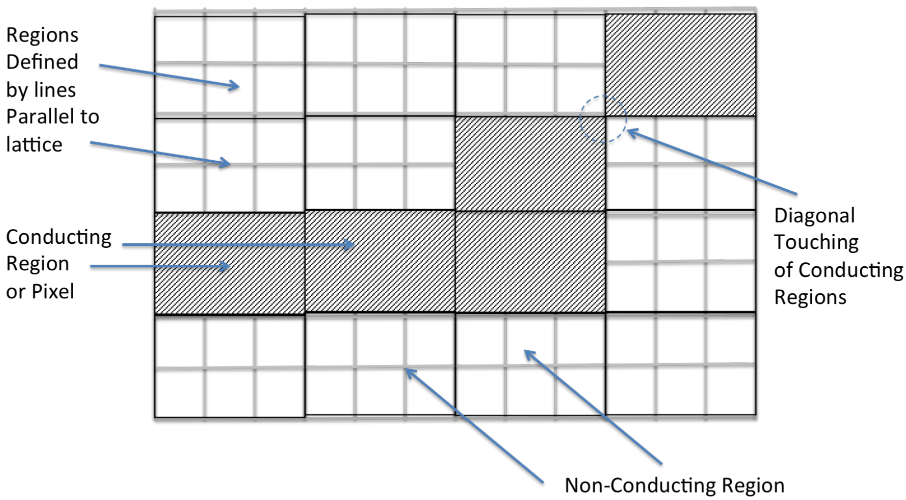

Figure 3.1: Original fragmented aperture approach based on a lattice of rectangular pixels. An example of diagonal touching is shown in the top right of the figure.

3.2 The Diagonal Touching Problem

Originally, fragmented aperture antennas were envisioned as a planar surface partitioned into a grid of rectangular pixels, each either conducting or non-conducting, as shown in Figure 6.1. A genetic algorithm and a computational electromagnetic model determined which pixels should be conducting and which should be non-conducting to form an antenna surface suitable for a given application. This concept was generalized to parallelogram-shaped pixels, as shown in Figure 3.2, in the original fragmented aperture patent [3].

As discussed in Chapter 2, the rectangular pixel approach was very successfully used to design novel antennas [1]–[2]. However, many of these designs proved troublesome to fabricate and measure. The primary problem is *diagonal touching* of pixels, as illustrated in the top right of Figures 6.1 and 3.2.

Diagonal touching is not a problem during the design phase because in the FDTD numerical model, diagonally adjacent conducting pixels are always electrically connected. However, when fabricated using processes such as printed circuit board etching, the diagonal contact is often broken due to over-etching, as illustrated in Figure 3.3(a). Disconnecting metal that should be connected can seriously degrade the antenna's impedance match and gain characteristics.

Other researchers have also observed the difficulties caused by diagonal touching. A close-up photograph of an etched copper fragmented surface is shown in Figure 3.3(b), where the disconnection of diagonally adjacent pixels is clearly visible [11].

In fact, nearly every antenna design included in the original fragmented aperture patent suffers from the diagonal touching problem. Figure 3.4 shows a few examples from U.S. Patent 6,323,809 [3], with the most troublesome diagonal-touching locations near the antenna feed circled.

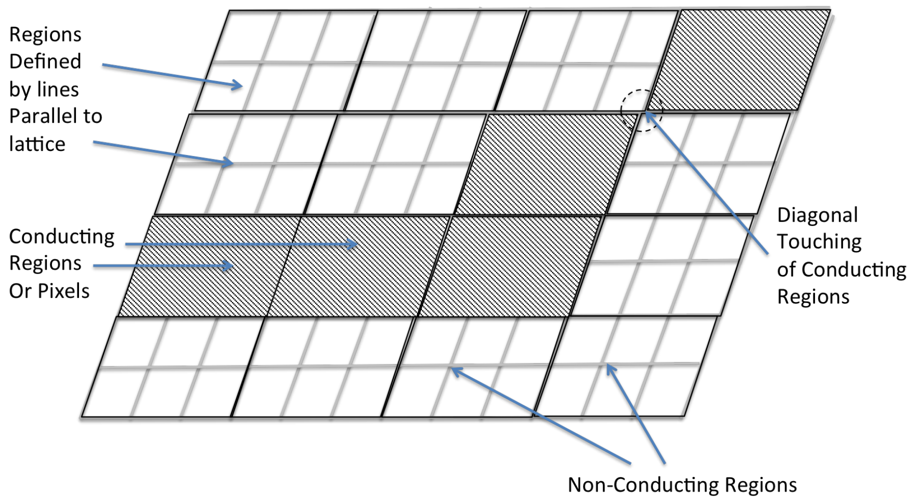

Figure 3.2: Generalized fragmented aperture approach based on parallelogram-shaped pixels. Again, an example of diagonal touching is shown in the top right of the figure.

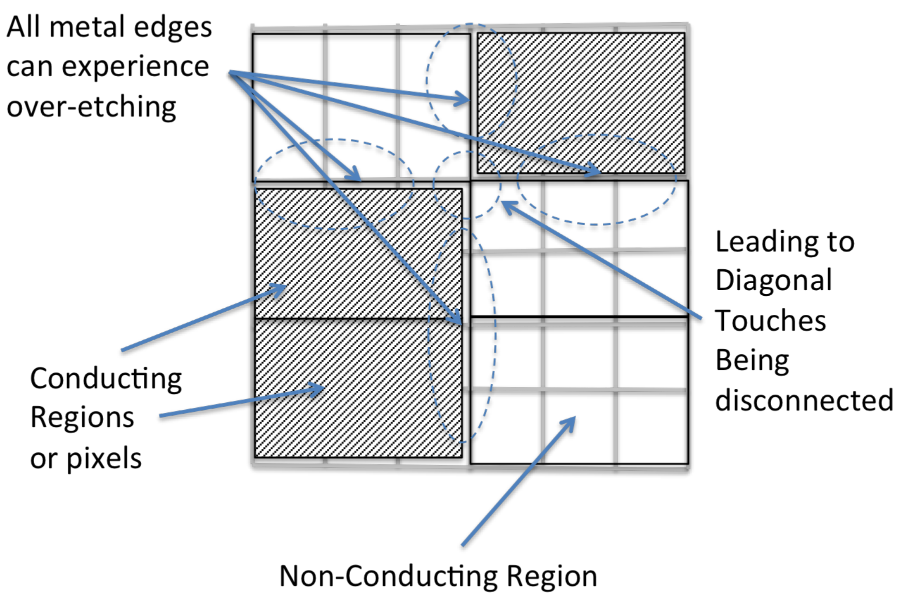

Figure 3.3: (a) Over-etching causing diagonal elements not to touch, as shown in the top center. (b) Close-up photograph of an etched copper fragmented antenna showing over-etch disconnecting diagonal fragments.

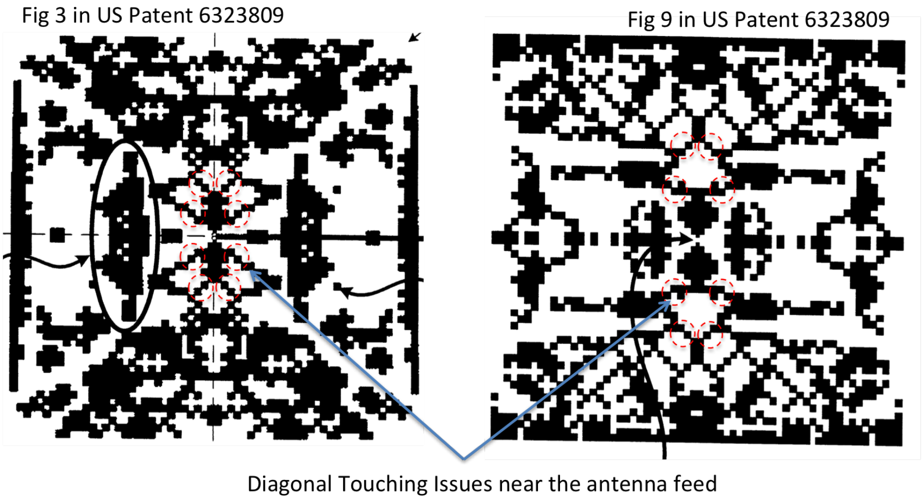

Figure 3.4: Two sample designs from the original fragmented aperture patent exhibiting diagonal touching [3]. The most troublesome examples of diagonal touching near the antenna feed are circled.

The root cause of the problem lies in the fundamental approach to area partitioning. When the pixel edges are parallel to the lattice forming vectors, as in Figures 6.1 and 3.2, the issue of diagonal touching is unavoidable. The next two sections present solutions: Section 3.3 describes several practical mitigation strategies, while Section 3.4 presents three improved pixel geometries that inherently eliminate diagonal touching.

3.3 Mitigation Strategies for Diagonal Touching

Before presenting the improved pixel geometries, it is instructive to review several practical strategies that have been used over the years to mitigate diagonal touching in designs based on the original rectangular pixel approach. Four such strategies are illustrated in Figure 3.5.

3.3.1 Super-Cell Approach

One approach that was successfully exploited is the super-cell strategy shown in Figure 3.5(a). A super-cell is a collection of smaller sub-elements—for example, a 3×3 grid of sub-pixels. To avoid diagonal touching, the conducting area is defined as the five sub-elements that form a plus sign, leaving the four corner sub-elements always non-conducting. This guarantees that no diagonal touching can occur.

The super-cell approach successfully produced antennas with good correlation between measurement and model. However, restricting the conducting area to plus-sign shapes forces electrical currents to flow only in directions aligned with the grid, which over-constrains the design and can lead to suboptimal antenna performance.

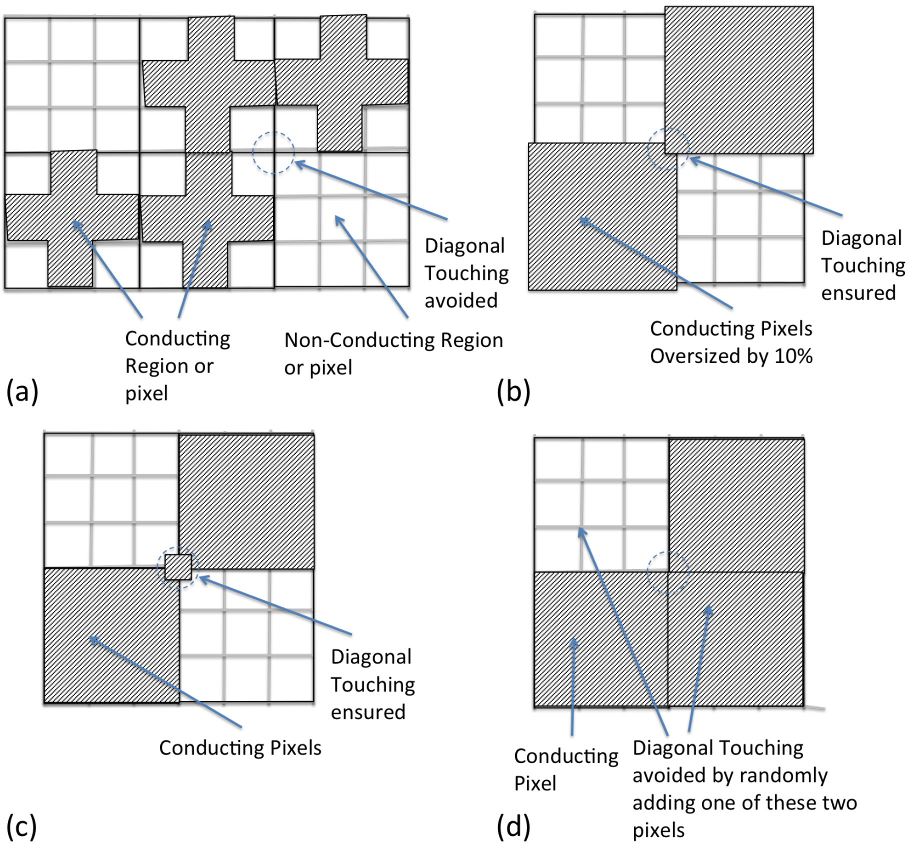

Figure 3.5: Four approaches to mitigating diagonal touching: (a) super-cell approach using 3×3 plus signs, (b) fabricating each pixel approximately 10% larger than designed, (c) placing a small metal square at diagonal contact points to ensure connection, and (d) random coin-flip approach to resolve diagonal ambiguity.

3.3.2 Oversized Fabrication

Another successful approach was to intentionally fabricate every pixel approximately 10% larger than designed, as illustrated in Figure 3.5(b). This enlargement ensures that diagonally adjacent pixels overlap slightly, guaranteeing electrical contact. This strategy was found to yield a high percentage of successfully fabricated antennas.

However, oversized fabrication results in the antenna having roughly 10–20% more conductor than originally designed, which can alter the antenna characteristics from the design predictions. It is worth noting that fabricating pixels 10% *smaller* would guarantee that diagonal pixels never touch, but this would mean that conducting regions could never extend beyond a single pixel—a condition that would render the antenna virtually useless. Moreover, smaller fabrication would be inconsistent with the FDTD model used during design, in which diagonally adjacent conducting pixels are always connected.

3.3.3 Metal Bridge and Coin-Flip Approaches

Other research groups have developed additional strategies. Ellgardt and Persson [5] considered both the oversized pixel strategy of Figure 3.5(b) and a variant in which a small square of metal is placed at each diagonal contact point to ensure connection, as shown in Figure 3.5(c). Rahmat-Samii and colleagues at UCLA have used a random coin-flip process to resolve diagonal ambiguity: when two non-conducting pixels are diagonally adjacent to two conducting pixels, a random selection determines which non-conducting pixel is made conducting to complete the connection, as illustrated in Figure 3.5(d).

While each of these mitigation strategies can be effective, they all represent workarounds for a fundamental problem. The proper solution is to change the pixel geometry itself so that diagonal touching cannot occur, as described in the next section.

3.4 Three Improved Pixel Geometries

The proper approach to eliminating diagonal touching is to break the dependence between pixel edges and lattice directions that is implicit in the rectangular and parallelogram geometries of Figures 6.1 and 3.2. The following three subsections present three different pixel geometries that accomplish this, each leading to improved fragmented aperture antennas. Recent studies have examined important design considerations such as pixel size, symmetry constraints, and their effects on antenna performance [12].

3.4.1 First Approach: Skewed Lattice

In the first approach, the individual conducting/non-conducting elements are defined using lattice vectors that are not both parallel to the element edges, as illustrated in Figure 3.6. The example shown uses square elements arranged on a skewed lattice with a skew angle of $\psi \approx 63.4°$.

Notice that skewing the lattice vector $\vec{V}_2$ completely eliminates the possibility of diagonal touching. Every adjacent pixel pair shares a full edge, so the electrical con-

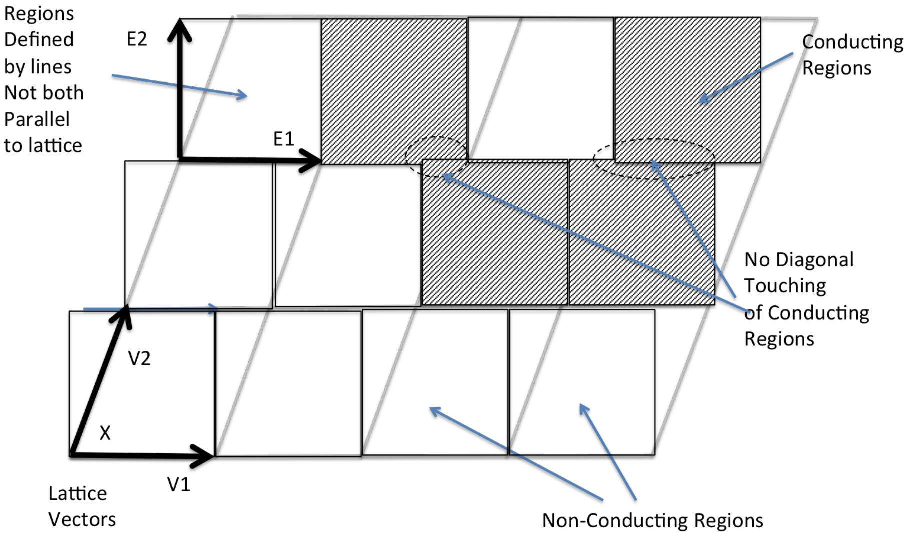

Figure 3.6: First approach to improved fragmented aperture antennas: square elements on a skewed lattice. Skewing the lattice vector $\vec{V}_2$ eliminates the possibility of diagonal touching.

nection between adjacent conducting pixels is always robust and unambiguous.

3.4.2 Second Approach: Alternating Pixel Shapes

In the second approach, two complementary pixel shapes are used that alternate across the aperture, as illustrated in Figure 3.7. The shapes are chosen so that adjacent pixels always share a definite edge rather than merely a corner point.

The key requirement is that the two shapes together tessellate the plane—that is, they tile the aperture surface without gaps or overlaps. When this condition is met and the shapes are designed so that adjacency always involves a shared edge, diagonal touching is inherently impossible.

3.4.3 Third Approach: Single Self-Tessellating Shape

In the third approach, a single pixel shape is chosen that tessellates the plane by itself while ensuring that adjacent pixels share edges rather than corner points. Figure 3.8 shows one example of such a shape, although many other shapes satisfying these requirements exist.

The advantage of a single-shape tessellation is simplicity of implementation: only one pixel geometry needs to be defined and manufactured. However, depending on the chosen shape, this approach may not naturally support the left-right and top-bottom symmetry constraints that are commonly imposed for broadside, linearly polarized antenna designs. This makes the third approach particularly well suited for designs where symmetry is not required, such as beam-steered or circularly polarized antennas.

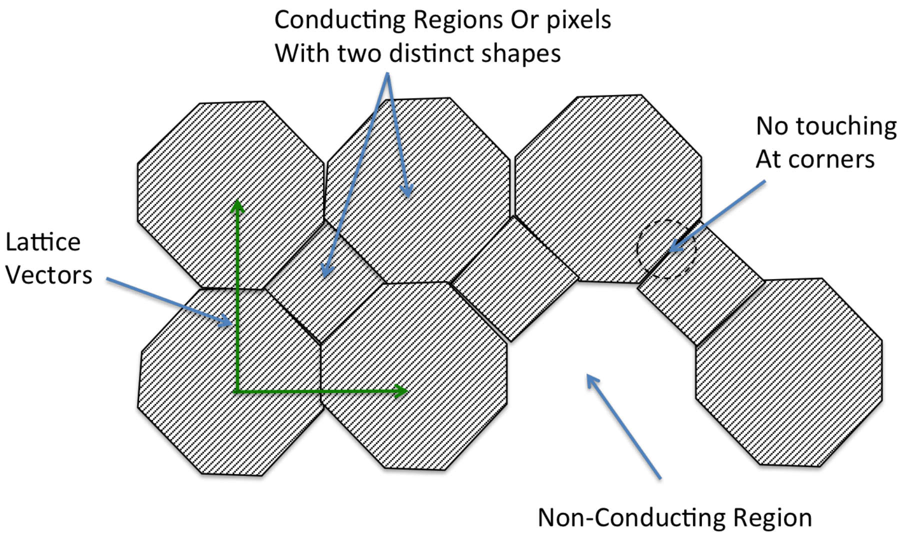

Figure 3.7: Second approach to improved fragmented aperture antennas: alternating pixel shapes that tessellate the plane while ensuring definite edge contact between adjacent pixels.

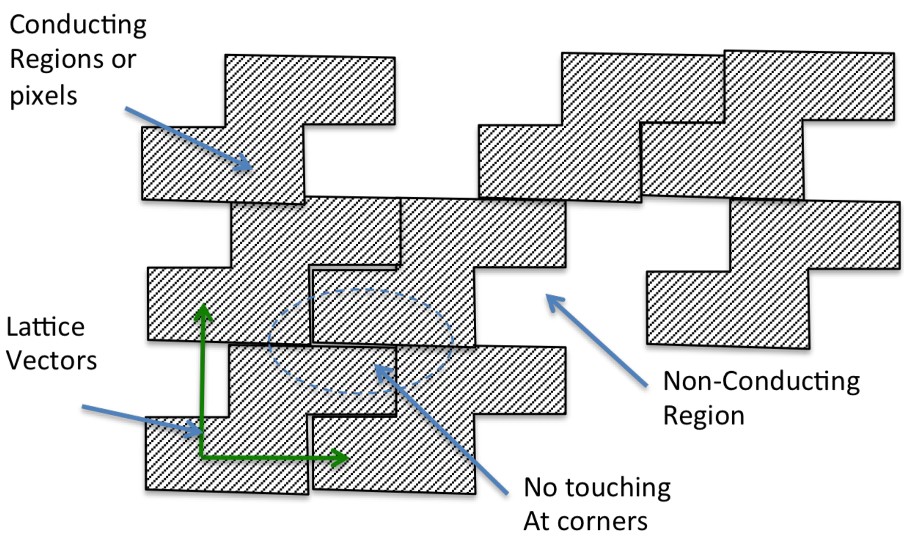

Figure 3.8: Third approach to improved fragmented aperture antennas: a single self-tessellating pixel shape that tiles the aperture surface while ensuring definite edge contact between all adjacent pixels.

3.5 Improved Mutation Algorithm for Better Convergence

In addition to the diagonal touching problem, the original fragmented aperture design approach suffered from poor convergence of the genetic algorithm when the number of pixels became large. This section describes an improved mutation operator that addresses this limitation. More recent work has explored alternative optimization approaches including topology optimization with level set methods [13], machine learning and neural network techniques [14, 15, 16], and reinforcement learning [17]; however, genetic algorithms remain popular due to their simplicity and effectiveness for pixelated antenna design [18, 19].

In a standard genetic algorithm, mutation is a random process in which a small number of genes are changed each generation to help the algorithm avoid convergence to suboptimal solutions. For a fragmented aperture antenna, mutation randomly toggles a few pixels between conducting and non-conducting states. However, many of these random mutations produce only an isolated metal pixel in a non-conducting region or a small hole in an otherwise solid metal area. Such changes have negligible effect on the antenna performance, and the mutation step is effectively wasted.

The improved mutation algorithm is biased so that mutations preferentially extend the boundaries of existing conducting fragments into empty regions, or enlarge holes within large metal regions. This is accomplished using an adjacency matrix that describes which pixels are in contact with each other. By analyzing the local neighborhood of each pixel, the algorithm identifies pixels at the boundaries between conducting and non-conducting regions and preferentially selects these boundary pixels for mutation.

To demonstrate the effectiveness of this adjacency-based mutation strategy, three independent design trials were conducted with the traditional mutation algorithm and three with the improved mutation algorithm. Figure 3.9 shows the convergence of the fitness score as a function of generation count, averaged over the three trials for each algorithm. The improved mutation algorithm (green line) converges to a better fitness score in fewer generations than the traditional approach (blue line).

As shown in Table 3.1, the improved mutation algorithm produced a better result than the traditional algorithm in every one of the three trials. The best trial with the improved algorithm achieved a fitness score of -1.684, compared to -2.238 for the best trial with the traditional algorithm—an improvement of more than 0.5 dB.

The results in Table 3.1 also illustrate an important practical point: when using an evolutionary algorithm to design an antenna, more than one design trial should always be executed. As these results show, the variation between trials can exceed 1 dB, so running multiple trials and selecting the best result is essential for obtaining high-quality designs.

3.6 Sample Improved Fragmented Aperture Designs

This section presents sample antenna designs produced using the improved pixel geometries described in Section 3.4. All designs use the improved mutation algorithm of

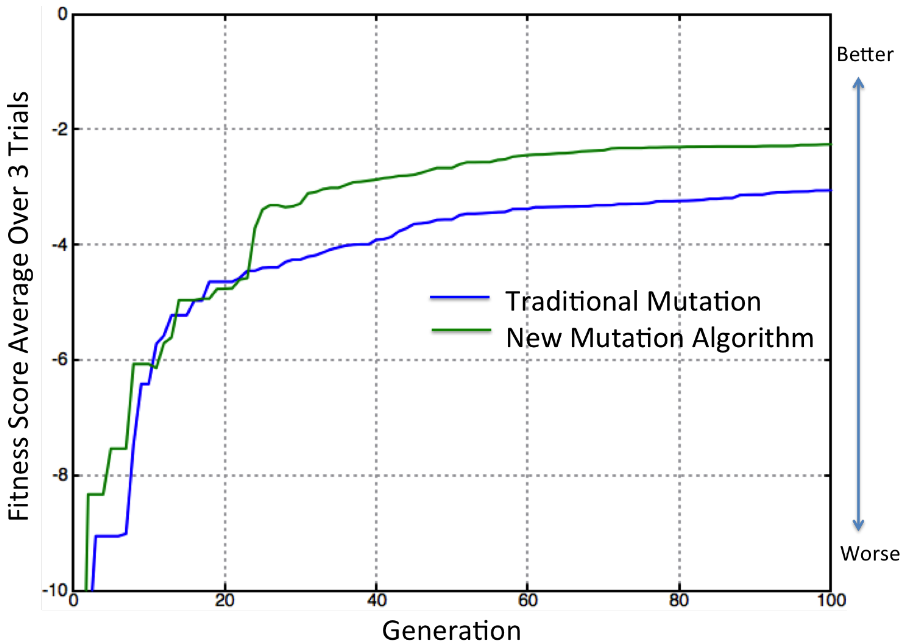

Figure 3.9: Convergence comparison between the traditional mutation algorithm (blue) and the improved adjacency-based mutation algorithm (green), averaged over three independent design trials. The improved algorithm converges to a better fitness score in fewer generations.

Table 3.1: Fitness score comparison across three convergence trials for the traditional and improved mutation algorithms (higher score is better).

Fitness Score Comparison	Tradiational Mutation Algorithm	New Mutation Algorithm
Best of 3 Trials	-2.238	-1.684
Middle	-3.208	-2.461
Worst	-3.727	-2.850

Section 3.5.

3.6.1 First Approach Designs

The skewed-lattice approach of Figure 3.6 was used to design a series of fragmented aperture antennas spanning from 500 MHz to 2.0 GHz. The lattice skew angle was chosen to be $\psi = \tan^{-1}(2) \approx 63.4°$, which provides the left-right physical symmetry needed for linearly polarized broadside designs. The square pixels were 10.8 mm on a side, and the total aperture area was 25.4 cm $\times$ 25.4 cm. Each antenna was excited at a terminal pair at the center of the aperture with a 100 Ω transmission line.

The aperture designs were performed using a genetic algorithm with FDTD evaluation of each candidate antenna (see Appendix A for details on FDTD modeling of antennas). For these designs, the 25.4 cm $\times$ 25.4 cm aperture contained 663 individual pixels. Enforcing left-right and top-bottom symmetry reduced the number of independent degrees of freedom to 169. With a single bit representing the state of each pixel (1 = conducting, 0 = non-conducting), this yields a 169-bit genetic code. Using a population size of 32 antennas, approximately 100 GA generations were required to produce each design. The fitness function rewarded good impedance match (return loss better than 15 dB) and maximum broadside realized gain.

Four representative aperture designs are shown in Figure 3.10. The physical shapes clearly demonstrate that none of the designs suffer from diagonal touching—every connection between adjacent conducting pixels involves a full shared edge.

Figure 3.11 shows the broadside realized gain of each design as a function of frequency. The gains are compared with the aperture gain limit (black line), which for these ground-plane-free apertures is $2\pi A/\lambda^2$. All four designs approach the aperture gain limit within their respective design bands.

Figure 3.12 shows the VSWR of each design. The VSWR remains below 1.5 across the respective design bands, consistent with the fitness function requirement of return loss better than 15 dB.

3.6.2 Second Approach Designs

The alternating-shape approach of Figure 3.7 was also used to design fragmented aperture antennas. This pixel geometry naturally supports both left-right and top-bottom symmetry when required. The aperture area was again 25.4 cm $\times$ 25.4 cm, excited at the center with a 100 Ω feed. The aperture contained 841 shaped pixels, and with both symmetries enforced, the number of independent degrees of freedom was 221.

[Note: The Second Approach currently has two sample designs. Four designs are planned to match the First Approach presentation. Figures and text to be updated.]

Figure 3.13 shows two sample designs for the 0.5–0.8 GHz and 0.8–1.2 GHz bands. As with the first approach designs, no diagonal touching is present in the physical structures.

Figures 3.14 and 3.15 summarize the broadside gain and VSWR for these two designs. The performance is consistent with the design objectives, with gain approaching the aperture limit within each design band and VSWR remaining below 1.5.

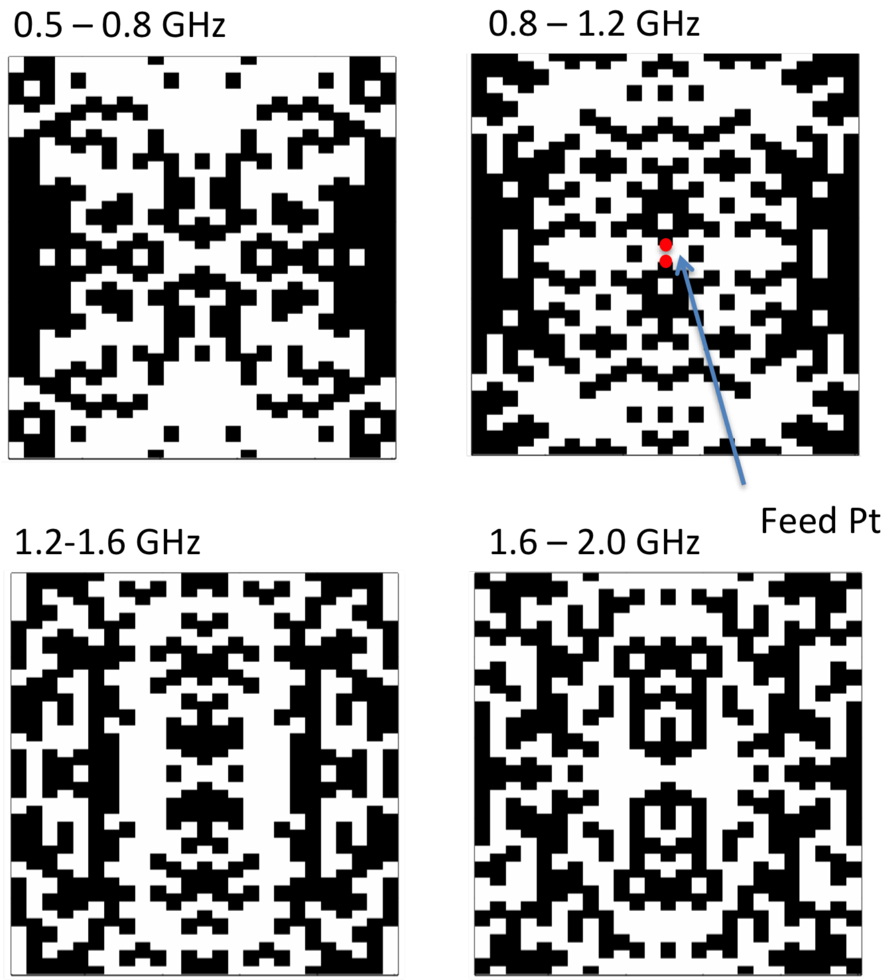

Figure 3.10: Four sample fragmented aperture designs produced using the skewed-lattice (First Approach) pixel geometry. None of the designs exhibit diagonal touching.

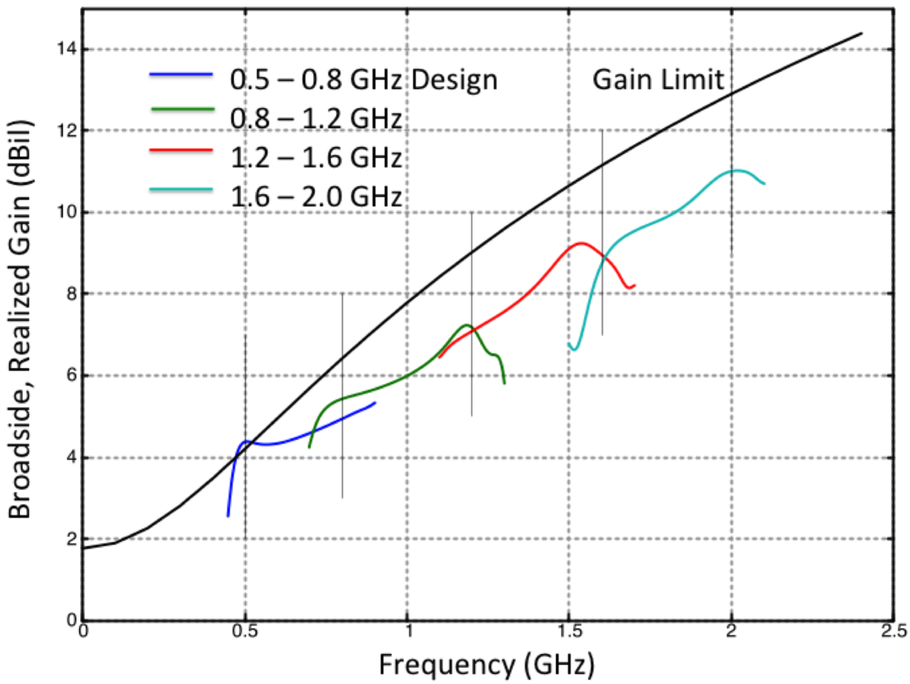

Figure 3.11: Broadside realized gain for the four skewed-lattice designs shown in Figure 3.10. The black line indicates the aperture gain limit $2\pi A/\lambda^2$.

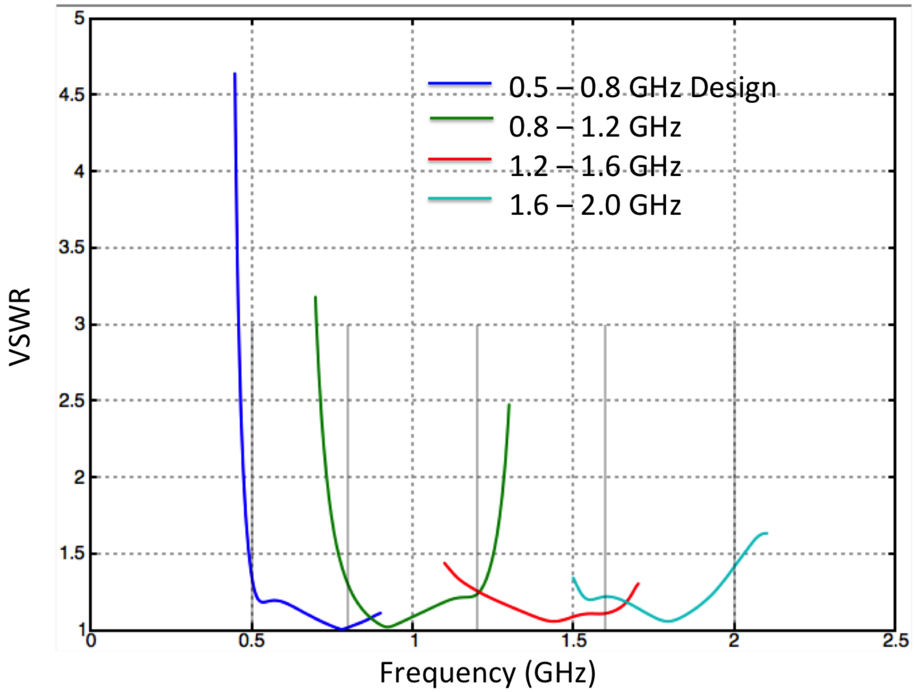

Figure 3.12: VSWR for the four skewed-lattice designs shown in Figure 3.10.

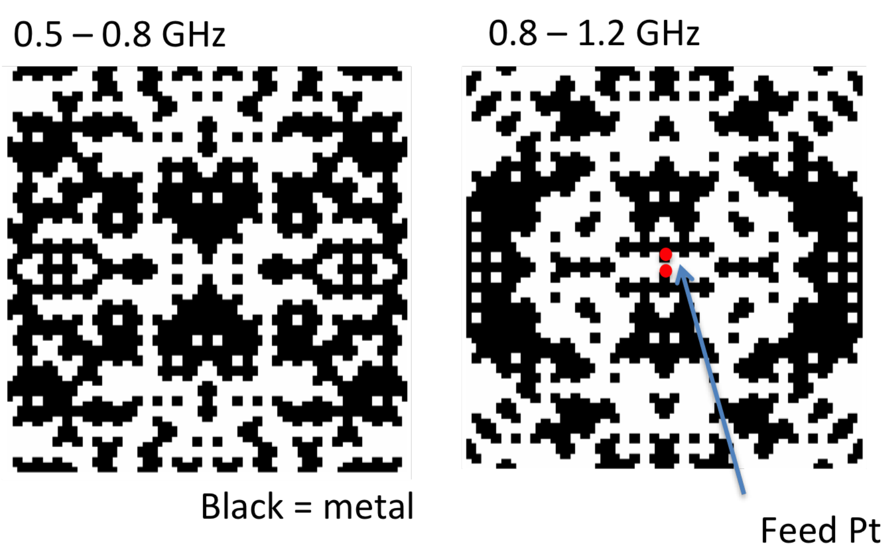

Figure 3.13: Two sample fragmented aperture designs produced using the alternating-shape (Second Approach) pixel geometry for the 0.5–0.8 GHz and 0.8–1.2 GHz bands.

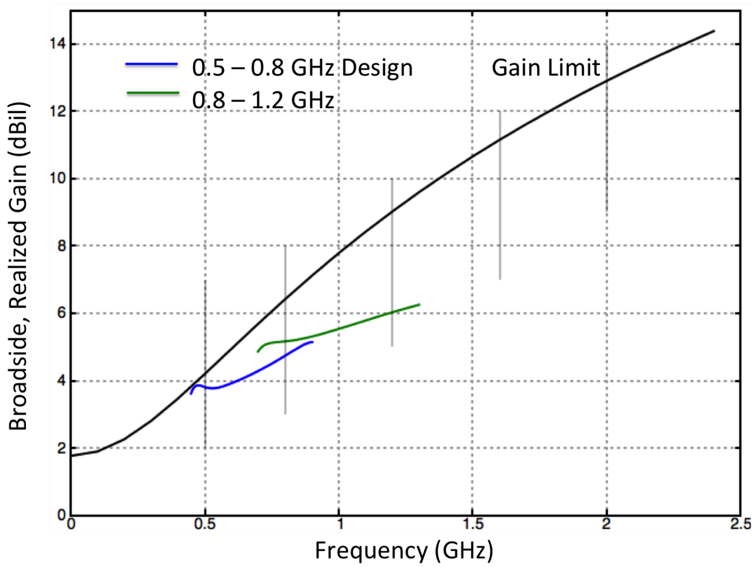

Figure 3.14: Broadside realized gain for the two alternating-shape designs shown in Figure 3.13.

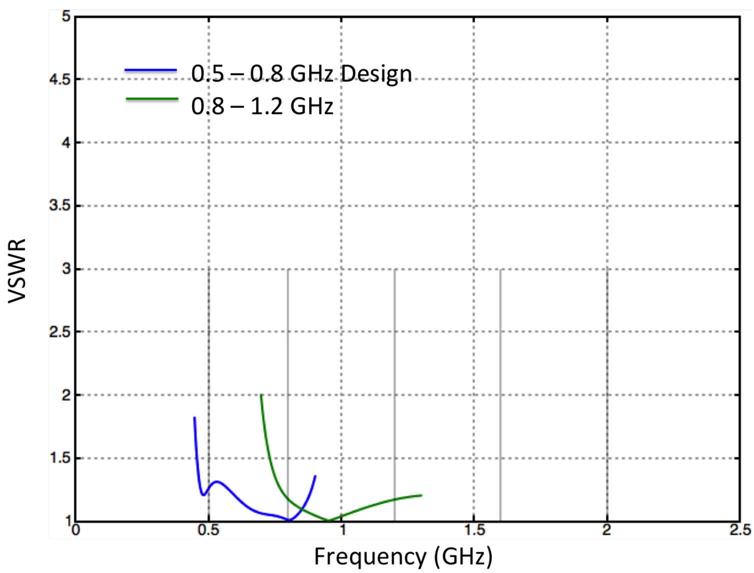

Figure 3.15: VSWR for the two alternating-shape designs shown in Figure 3.13.

3.6.3 Third Approach Designs

The self-tessellating shape approach of Figure 3.8 can also be used to design fragmented aperture antennas. As noted earlier, for vertically or horizontally polarized elements with a broadside beam, the lack of inherent left-right and top-bottom symmetry in many self-tessellating shapes is a drawback. However, for applications where the desired beam direction is not broadside or the desired polarization is circular or slant-linear, symmetry constraints are not needed and the third approach is fully competitive with the first and second.

[Missing content: Third Approach sample designs are needed. Planned designs include: (a) broadside vertically polarized, (b) broadside horizontally polarized, (c) broadside slant-linear polarized, and (d) vertically polarized beam steered $45°$ from broadside. Corresponding gain, VSWR, and azimuth pattern figures are also needed.]

References

[1] J. G. Maloney, M. P. Kesler, P. H. Harms, T. L. Fountain, and G. S. Smith, "The fragmented aperture antenna: FDTD analysis and measurement," in *Millennium Conference on Antennas and Propagation (AP 2000)*, 2000, p. 93.

[2] W. Croswell, T. Durham, M. Jones, D. Schaubert, P. G. Friederich, and J. G. Maloney, "Wideband arrays," in *Modern Antenna Handbook*, C. A. Balanis, Ed. John Wiley & Sons, 2011, ch. 12.

[3] J. G. Maloney, M. P. Kesler, P. H. Harms, and G. S. Smith, "Fragmented aperture antennas and broadband ground planes," U.S. Patent No. 6,323,809 B1, Nov. 2001.

[4] N. Herscovici, J. Ginn, T. Donisi, and B. Tomasic, "A fragmented aperture-coupled microstrip antenna," in *IEEE Antennas and Propagation Society International Symposium*, Jul. 2008, pp. 1–4.

[5] A. Ellgardt and P. Persson, "Characteristics of a broad-band wide-scan fragmented aperture phased array antenna," in *European Conference on Antennas and Propagation (EuCAP)*, Nov. 2006, pp. 1–5.

[6] B. Thors, H. Steyskal, and H. Holter, "Broad-band fragmented aperture phased array element design using genetic algorithms," *IEEE Transactions on Antennas and Propagation*, vol. 53, no. 10, pp. 3280–3287, 2005.

[7] N. Barani, J. F. Harvey, and K. Sarabandi, "Fragmented antenna realization using coupled small radiating elements," *IEEE Transactions on Antennas and Propagation*, vol. 66, no. 4, pp. 1725–1735, 2018.

[8] A. Ellgardt, "Wide-angle scanning wide-band phased array antennas," Ph.D. dissertation, KTH School of Electrical Engineering, Stockholm, Sweden, 2009, page 21 discusses diagonal touching issues.

[9] Y. Zang, M. Jin, and X. Jiao, “The optimum design of a 3-10ghz linear-polarized fragmented aperture array with integrated balun,” in *2019 International Symposium on Antennas and Propagation (ISAP)*, 2019, pp. 1–3.

[10] Y. Li, J. Dong, S. Wang, Y. Wu, B. Xiong, Q. Li, K. Wang, and Y. Zhang, “An automated approach for pixelated antenna topology design incorporating multi-objective optimization algorithms,” in *2019 International Conference on Microwave and Millimeter Wave Technology (ICMMT)*, 2019, pp. 1–3.

[11] A. Ellgardt and P. Persson, “Characteristics of a broad-band wide-scan fragmented aperture phased array antenna,” in *2006 First European Conference on Antennas and Propagation*, 2006, pp. 1–5.

[12] D. Mair, M. Renzler, and R. Rueland, “Design considerations for pixelated antennas regarding pixel size and symmetry,” in *2024 International Symposium on Electromagnetic Compatibility – EMC Europe*, 2024, pp. 226–231.

[13] C. T. Howard, A. Saad-Falcon, D. W. Landgren, and K. W. Allen, “Topology optimization of a wideband planar phased array element using periodic level set functions,” in *2024 IEEE International Symposium on Phased Array Systems and Technology (ARRAY)*, 2024, pp. 1–7.

[14] M. Li, Y. Wang, and M. Zhu, “Inverse design of pixelated antenna based on residual neural network,” in *2025 International Applied Computational Electromagnetics Society Symposium (ACES-China)*, 2025, pp. 1–3.

[15] Q. Wang, Z. Pang, D. Gao, P. Liu, X. Pang, and X. Yin, “Machine learning-assisted quasi-bisection method for pixelated patch antenna bandwidth optimization,” *IEEE Antennas and Wireless Propagation Letters*, vol. 23, no. 12, pp. 4807–4811, 2024.

[16] J. P. Jacobs, “Accurate and efficient modeling of gain patterns of multiband pixelated antenna by deep neural networks,” in *2022 International Conference on Electromagnetics in Advanced Applications (ICEAA)*, 2022, pp. 306–306.

[17] Q. Wang, Z. Pang, D. Gao, P. Liu, X. Zhang, X. Pang, and X. Yin, “Bandwidth enhancement of pixelated patch antennas based on localized reinforcement learning,” in *2024 14th International Symposium on Antennas, Propagation and EM Theory (ISAPE)*, 2024, pp. 1–4.

[18] D. Mair, M. Unterladstaetter, M. Renzler, and T. Ussmueller, “Evolutionary optimized pixelated antennas for 5g iot communication,” in *2022 52nd European Microwave Conference (EuMC)*, 2022, pp. 548–551.

[19] A. Zeghdoud, M. C. Derbal, and M. Nedil, “Accelerated convergence in ga-based patch antenna optimization using fuzzy logic and machine learning,” in *2025 IEEE International Symposium on Antennas and Propagation and North American Radio Science Meeting (AP-S/CNC-USNC-URSI)*, 2025, pp. 1829–1831.

Chapter 4

Sample Antenna Design

4.1 feed strategies

- feed strategies
- in-plane self-balun
- in-Plane twin feed
- unbalanced fed thru ground plane
- balanced fed thru ground plane
- tailor bandwidth
- fixed steering
- broadside
- forward and backward 45
- end fire
- Polarization
  linear
  circular
  non-broadside cp
- tailor beamwidth
- out-band-rejection

4.2 First Success

[2].

Figure A.1 is a schematic drawing showing a typical volume in which Maxwell's equations are to be solved. The volume is divided into unit cells each of volume.

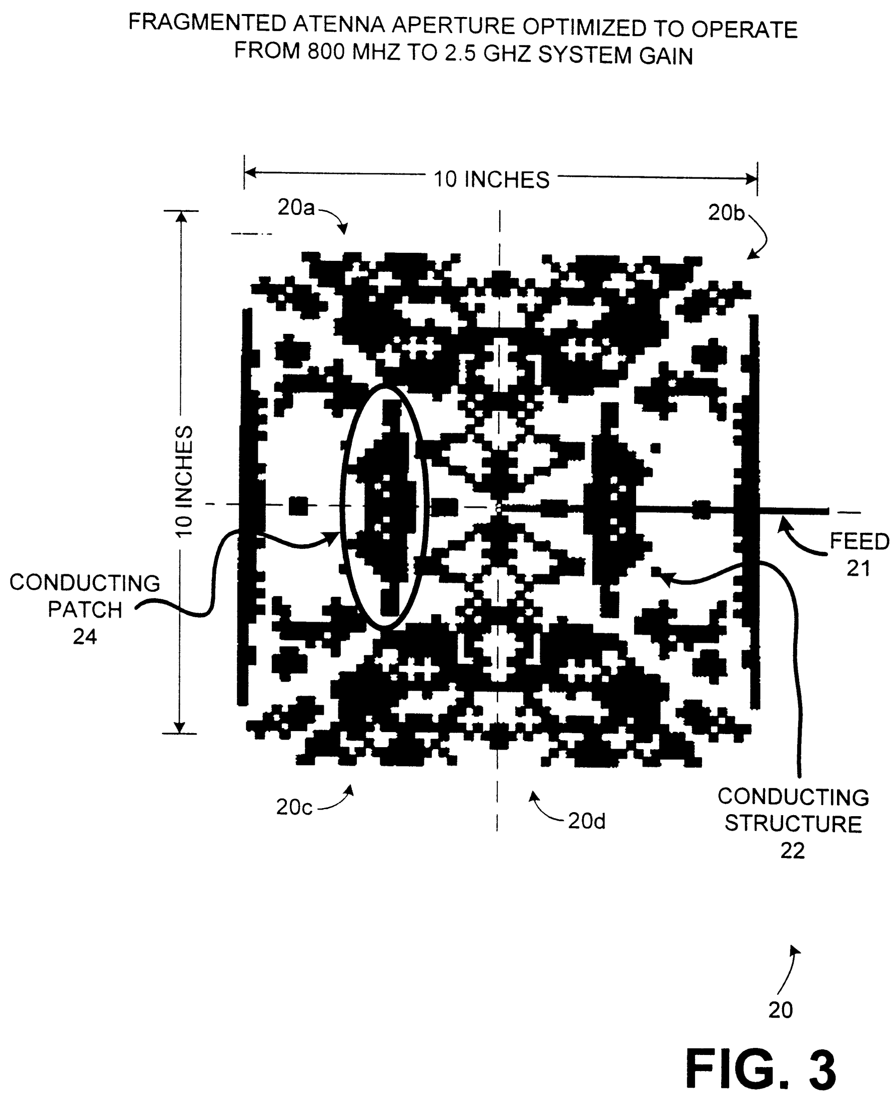

Figure 4.1: Comparison of fragmented design to uniform aperture limit $2\pi A/\lambda^2$

References

[1] K. S. Yee, "Numerical Solution of Initial Boundary Value Problems Involving Maxwell's Equations in Isotropic Media," IEEE Trans. Antennas Propagat., Vol. AP-14, pp. 302-307, May 1966.

[2] J. G. Maloney, G. S. Smith, and W. R. Scott, Jr., "Accurate Computation of the Radiation from Simple Antennas Using the Finite-Difference Time-Domain Method," IEEE Trans. Antennas Propagat., Vol. AP-38, pp. 1059-1068, July 1990.

[3] J. J. Boonzaaier and C. W. Pistorius, "Thin Wire Dipoles ? A Finite-Difference Time-Domain Approach," Electronics Lett., Vol. 26, pp. 1891-1892, 25 October, 1990.

[4] D. S. Katz, M. J. Picket-May, A. Taflove, and K. R. Umashankar, "FDTD Analysis of Electromagnetic Wave Radiation from Systems Containing Horn Antennas," IEEE Trans. Antennas Propagat., Vol. AP-39, pp. 1203-1212, August 1991.

Chapter 5

Reconfigurable Fragmented Aperture Antennas

5.1 Introduction

In the preceding chapters, we have shown how the fragmented aperture concept can be used to design antennas that meet particular performance specifications. A planar sheet of conductor is divided into many sub-wavelength pixels, and a genetic algorithm working with an FDTD simulation determines which pixels should be conducting and which should not. Different designs can be obtained to meet different specifications: for example, one design might produce an antenna with a broadside beam optimized for a particular bandwidth, while a second design might produce an antenna with the beam steered to 45^o from broadside.

Of course, once a fragmented aperture antenna is fabricated, it can only meet one set of specifications—either the broadside design or the steered design, but not both. It would be enormously useful if a single fragmented aperture could be electronically switched between different configurations to meet different requirements on demand. This would require a mechanism for dynamically changing individual pixels from conducting to non-conducting and vice versa. Recent work has demonstrated various reconfigurable pixelated antenna implementations using MEMS switches [1, 2], phase transition materials [3], and magnetically actuated mechanisms [4].

One can imagine, for example, making the cladding on a circuit board from a photoconductive material and using a laser to selectively illuminate the pixels that need to be conducting for a particular design. Changing the illumination pattern would reconfigure the antenna. While this particular approach remains impractical with current technology, the underlying idea—a reconfigurable fragmented aperture—motivated the development of the Agile Aperture Antenna described in this chapter.

5.2 The Agile Aperture Antenna Concept

The concept of a reconfigurable fragmented aperture antenna was first published in 2000 under the name "switched fragmented aperture antenna" [5]. Subsequently, DARPA funded a solicitation for "reconfigurable aperture" antennas and coined the acronym RECAP. To distinguish the fragmented aperture approach from other reconfigurable antenna concepts, we later adopted the term "Agile Aperture Antenna" (A3), emphasizing that the purpose of reconfiguration is to make the antenna *agile*—able to dynamically change its frequency of operation, beam direction, polarization, or other characteristics. The seminal IEEE paper on this work [6] and a comprehensive book chapter [7] provide detailed treatments of reconfigurable aperture antenna technology.

The Agile Aperture Antenna implementation that was successfully demonstrated is shown schematically in Figure 5.1 [8]. A thin dielectric substrate supports an array of square metallic pads. The pads are electrically small, with side length l satisfying $l/\lambda_o \ll 1$, where λ_o is the free-space wavelength at the operating frequency. Each pad is connected to its neighboring pads by switched links, indicated by the arrows in the figure. Each switch may be independently set to open or closed depending on the desired antenna configuration. A single feed point (pair of terminals) is located near the center of the antenna.

The Agile Aperture Antenna can be understood as a variant of the fragmented aperture antenna in which the fundamental unit is not a single pixel but a metallic pad composed of a group of pixels. The pads are not contiguous; they are separated by narrow dielectric gaps. The antenna structure for any given configuration consists of the conducting pads that are connected by closed switches, together with all of the unconnected pads that remain present on the substrate. This is an important distinction from a conventional fragmented aperture: in the Agile Aperture Antenna, the unconnected pads are always physically present and contribute to the electromagnetic behavior of the antenna through scattering, even when they are not part of the connected conducting structure.

5.3 Static Proof of Concept

INSERT: Description of the first two static (hard-wired) pixelated designs that demonstrated the unconnected pads did not prevent good antenna performance. Include figures showing the two designs and their measured performance.

5.4 Reconfigurable Proof of Concept

To prove the validity of the Agile Aperture Antenna concept, a detailed study was conducted using a prototype antenna with hard-wired switches—gaps that were either closed by a soldered wire or left open. This study not only validated the design approach but also identified areas where future research would be needed to extend the concept to practical, electronically reconfigurable antennas.

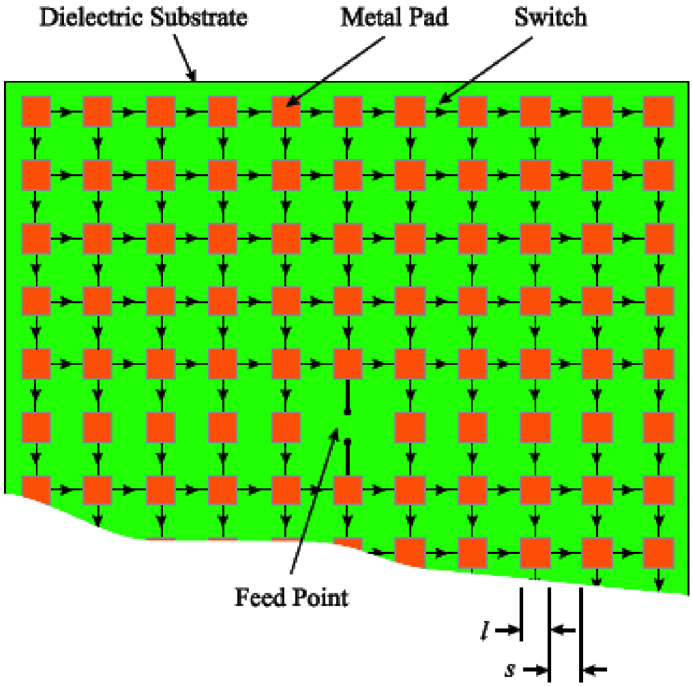

Figure 5.1: Schematic drawing of the Agile Aperture Antenna in dipole form. Square metallic pads are connected by switched links (arrows). The state of each switch (open or closed) determines the antenna configuration [8].

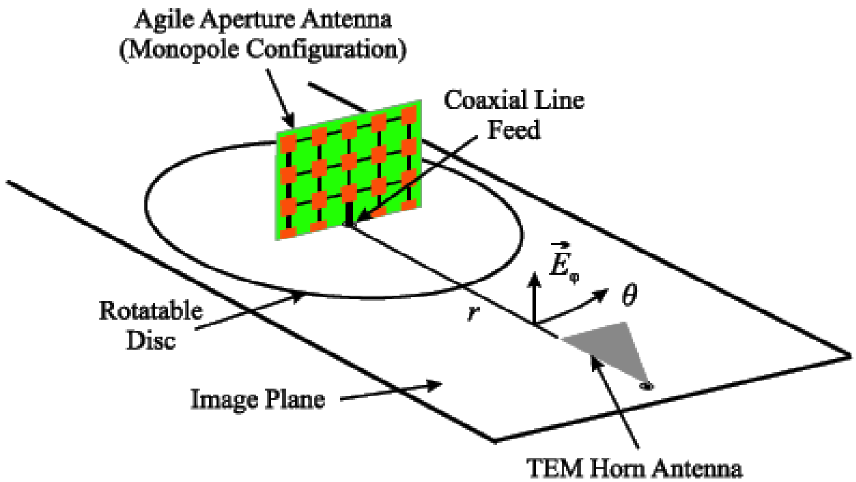

Figure 5.2: Experimental arrangement for measuring the Agile Aperture Antenna in monopole form. The antenna is mounted vertically on a rotatable disc centered in a large metallic image plane [8].

5.4.1 Prototype Description

For all of the antennas discussed in this section, the aperture was formed from a printed circuit board 22.5 cm $\times$ 22 cm in size, with the pads etched from the copper cladding on one side of the board. The pad side length and spacing were both $l = s = 1.0$ cm (see Figure 5.1). The board contained a total of 120 pads and 208 switches. The dielectric substrate was 1.7 mm thick FR4 circuit board with measured electrical properties $\varepsilon_r = 4.27$ and $\tan\delta = 0.07$ (verify loss tangent value).

The frequency of operation was in the range 0.85 GHz $\leq f \leq 1.45$ GHz, so the pads were electrically small: $0.028 \leq l/\lambda_o \leq 0.048$. All of the antenna designs described in this section have mirror symmetry about the horizontal line through the feed point, including the states of the switches. This symmetry allows the antennas to be analyzed and measured in either the "dipole form" shown in Figure 5.1 or the "monopole form" shown in Figure 5.2.

5.4.2 Measurement Setup

Figure 5.2 shows the experimental setup used for all of the measurements reported in this section. The monopole version of the Agile Aperture Antenna was mounted vertically on a rotatable disc centered in a large metallic image plane (insert image plane dimensions). The antenna was fed from below the image plane by a 50 Ω coaxial line, with the center conductor connected to the bottom pad in the center column of the antenna. A calibrated TEM horn antenna was located at a distance of (insert distance) from the antenna [8]. The scattering parameters for the two-port network formed by the Agile Aperture Antenna and the TEM horn were measured with a network analyzer and used to determine the absolute gain of the Agile Aperture Antenna [9]. The horizontal radiation pattern ($|E|$ versus azimuth angle ϕ) was obtained by rotating the disc while recording the output signal from the horn.

5.4.3 Design Procedure

The procedure for designing a switch configuration for the Agile Aperture Antenna is conceptually the same as for a conventional fragmented aperture: a rigorous FDTD simulation of the antenna is run in conjunction with a genetic algorithm optimizer (see Appendix A for an introduction to the FDTD method). In all of the FDTD simulations reported here, cubical Yee cells with a side length of 2.5 mm were used. More recent optimization approaches for reconfigurable pixelated antennas include beam steering techniques [10] and quantum genetic algorithms [11].

A performance goal is first established—for example, maximum broadside realized gain over a specified bandwidth. The GA then searches for the switch configuration (which switches should be open and which should be closed) that best meets this goal. Taking into account the mirror symmetry of the antenna, there are $2^{104} \approx 2 \times 10^{31}$ possible switch configurations—far too many to evaluate exhaustively. The GA provides an efficient, though approximate, method for searching this enormous design space.

5.4.4 Broadside Design

The design goal for the first example was to maximize the broadside realized gain over the frequency range 0.85 GHz $\leq f \leq 1.25$ GHz (a fractional bandwidth of 38%). The target was that the realized gain should equal or exceed the directivity of a uniform sheet of vertically directed current occupying the same aperture area.

Figure 5.3(a) shows the switch configuration obtained by the GA for this broadband, bidirectional, broadside design. Notice that this configuration has right-left symmetry in addition to the imposed top-bottom symmetry; all of the broadside designs discussed in this chapter are constrained to have this additional symmetry.

Figure 5.4(a) shows the realized gain versus frequency for this design. The dashed blue line is the design goal (uniform aperture directivity), the solid black line is the FDTD simulation, and the red line with markers is the measured result. All realized gain values are for the antenna in the dipole configuration. The simulated and measured realized gains are in good agreement over the design bandwidth, with a maximum difference of approximately 1 dB. The realized gain falls approximately 0.5–1.5 dB below the goal; a portion of this difference is attributable to impedance mismatch at the antenna feed.

Figure 5.4(b) shows the mismatch factor $(1 - |\Gamma_A|^2)$ as a function of frequency, where Γ_A is the voltage reflection coefficient at the antenna terminals. Within the design bandwidth, this factor ranges from 0.0 dB to -1.5 dB, confirming that mismatch accounts for a significant portion of the difference between the realized gain and the goal.

Figure 5.5 shows the horizontal radiation pattern at the center frequency $f =$

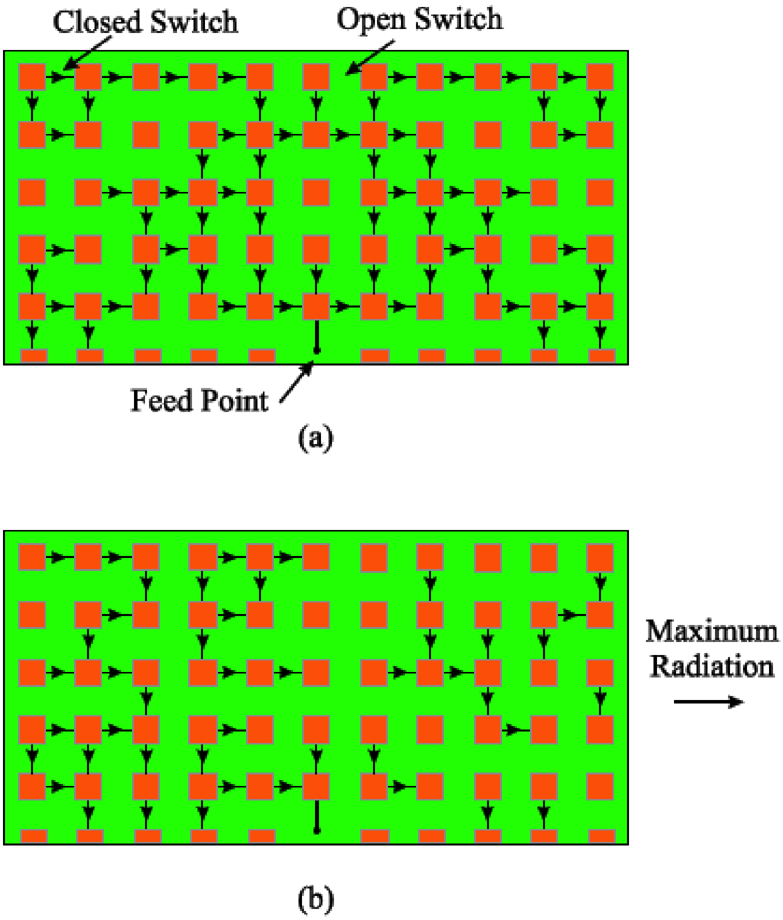

Figure 5.3: Switch configurations for the Agile Aperture Antenna (monopole form) with hard-wired switches. (a) Broadband, bidirectional, broadside design. (b) Narrow-band, unidirectional, end-fire design. The two configurations are strikingly different, yet both are realized on the same physical antenna [8].

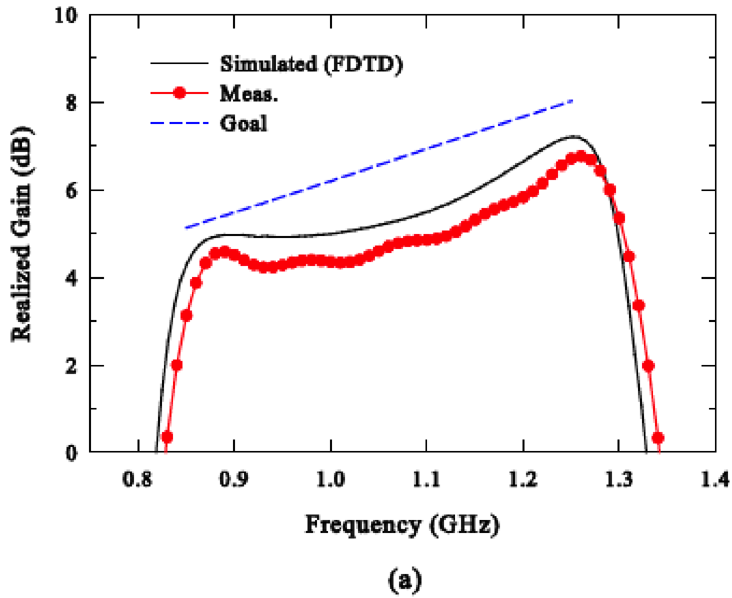

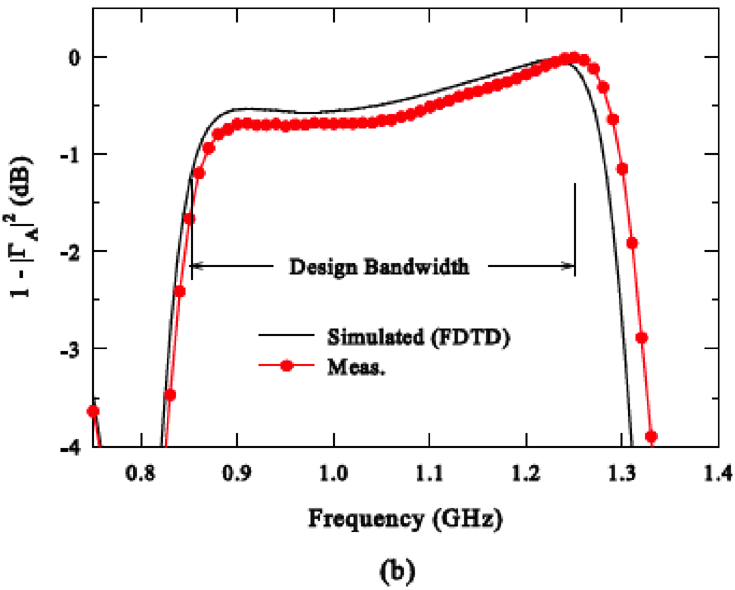

Figure 5.4: Results for the broadband, bidirectional, broadside design with hard-wired switches. (a) Realized gain versus frequency. (b) Gain reduction due to impedance mismatch: $(1 - |\Gamma_A|^2)$ [8].

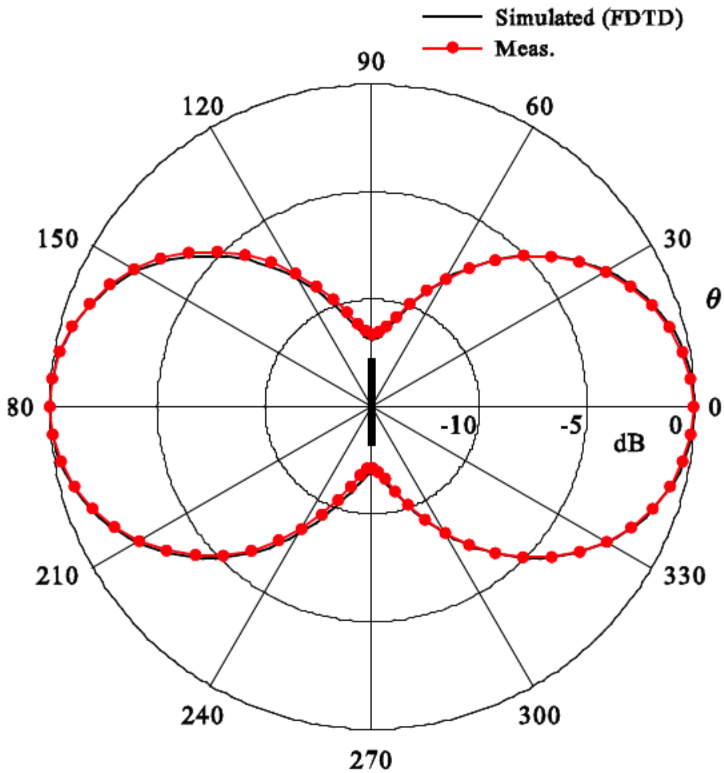

Figure 5.5: Horizontal radiation pattern at $f = 1.05$ GHz for the broadband, bidirectional, broadside design with hard-wired switches. Both patterns are normalized to 0 dB [8].

1.05 GHz. The simulated and measured patterns are nearly identical, with both normalized to a maximum of 0 dB. The heavy line at the center of the pattern indicates the orientation of the dielectric substrate.

5.4.5 End-Fire Design

To demonstrate the versatility of the Agile Aperture Antenna concept, a second design was produced for a completely different objective: a narrowband, unidirectional, end-fire beam over the frequency range 1.0 GHz $\leq f \leq 1.1$ GHz (a fractional bandwidth of 9.5%). The goal was again that the realized gain should equal or exceed the directivity of a uniform sheet of current, but now with the current phased to produce end-fire radiation.

Figure 5.3(b) shows the switch configuration for this end-fire design. It is immediately apparent that this configuration is strikingly different from the broadside configuration in Figure 5.3(a)—the end-fire design does not have right-left symmetry and produces a fundamentally different current distribution on the aperture. Yet both configurations are realized on the same physical hardware simply by changing which switches are open and which are closed.

Figure 5.6(a) shows the realized gain versus frequency for the end-fire design. The simulated and measured results are again in good agreement over the design bandwidth, with a maximum difference of approximately 1 dB. The realized gain falls approximately 1.0–2.0 dB below the goal. The mismatch factor shown in Figure 5.6(b) is within the range 0.0 dB to -0.8 dB over the design bandwidth.

Figure 5.7 shows the horizontal radiation pattern at $f = 1.05$ GHz. The simulated and measured patterns are in excellent agreement, and both clearly show the characteristic end-fire beam directed to one side of the antenna.

5.4.6 Observations on the Designed Configurations

In the configurations studied, approximately 30% to 60% of the switches were closed. One might expect that examination of the switch states for a particular design would reveal recognizable antenna structures—for example, the end-fire design might show strings of pads forming linear elements arranged like the driven element, reflector, and director of a Yagi-Uda array. However, as seen in Figure 5.3(b), this is not the case. In general, there is no simple, discernible relationship between the switch states and the design goal.

This lack of an obvious physical interpretation is consistent with the experience from conventional fragmented aperture design (Chapter 2): the GA discovers complex, non-intuitive structures that exploit the full electromagnetic physics of the problem. In the case of the Agile Aperture Antenna, the optimization is further complicated by the presence of the unconnected pads, which scatter electromagnetic energy and must be accounted for in the design. It is clear, however, that the switch connections near the feed point are often arranged to improve the impedance match between the antenna and the transmission line.

5.5 Discussion

The broadside and end-fire examples presented above, along with several other designs not shown, demonstrate that the Agile Aperture Antenna concept is viable: a single physical antenna can be reconfigured via its switch states to meet fundamentally different performance specifications. The excellent agreement between FDTD simulations and measurements further validates the design procedure.

However, for the Agile Aperture Antenna to transition from a laboratory concept to a practical technology, several challenges must be addressed. Most critically, a switch technology must be developed that can be electronically controlled without interfering with the electromagnetic performance of the antenna. The switches must introduce minimal insertion loss when closed, provide high isolation when open, and the control circuitry (bias lines, drivers) must not distort the antenna's radiation characteristics.

Subsequent research has explored several promising switch technologies for reconfigurable pixelated antennas. MEMS-based switches have been successfully demon-

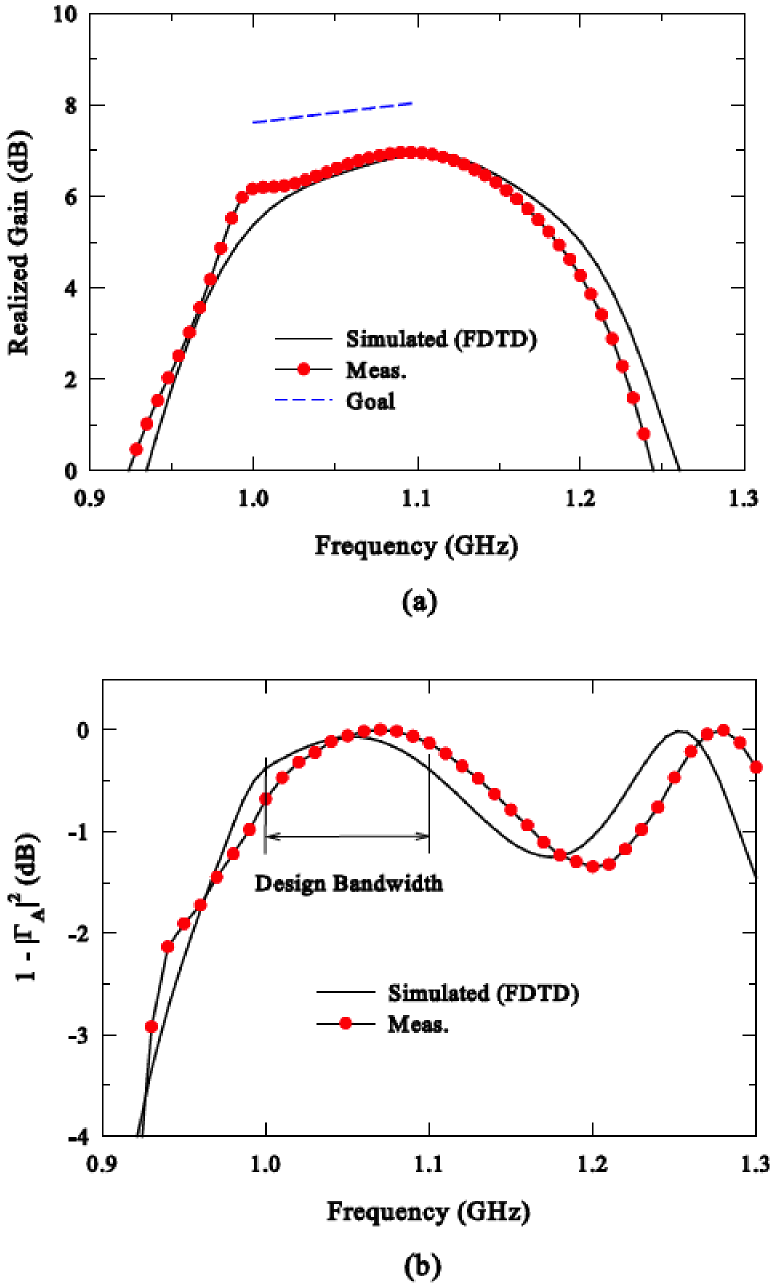

Figure 5.6: Results for the narrowband, unidirectional, end-fire design with hard-wired switches. (a) Realized gain versus frequency. (b) Gain reduction due to impedance mismatch: $(1 - |\Gamma_A|^2)$ [8].

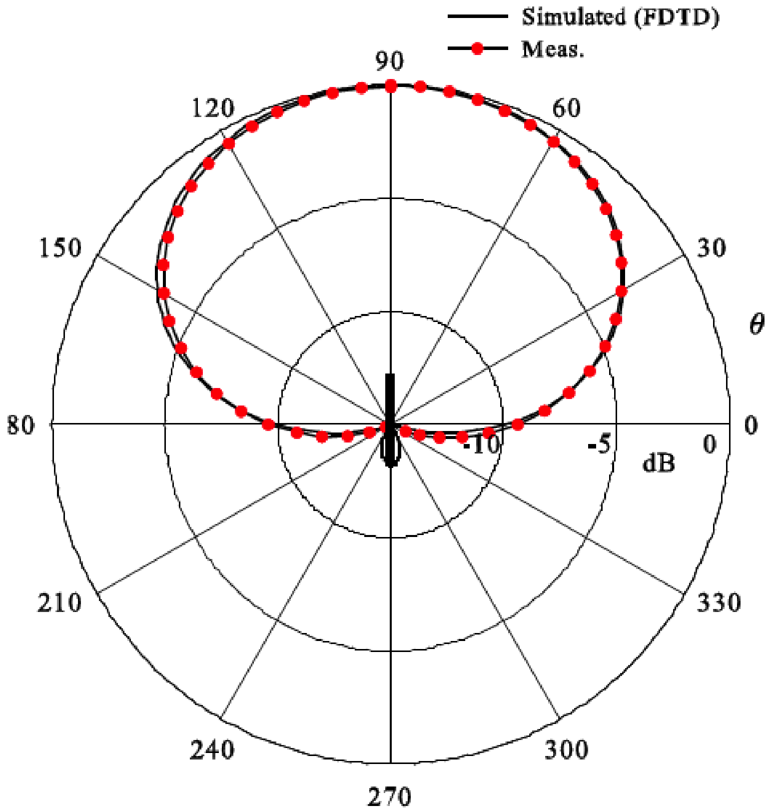

Figure 5.7: Horizontal radiation pattern at $f = 1.05$ GHz for the narrowband, unidirectional, end-fire design with hard-wired switches. Both patterns are normalized to 0 dB [8].

strated for reconfigurable patch antennas [12, 2, 1], offering excellent RF performance with low insertion loss and high isolation. Phase transition materials such as vanadium dioxide (VO2) provide another approach, enabling frequency reconfiguration through voltage-controlled phase changes [3]. Other techniques include magnetically actuated pixels [4] and tunable designs using varactors [13]. More recent work has focused on dual-port mmWave reconfigurable designs with optimized pixel configurations [14] and novel frequency reconfigurable implementations [15, 11].

5.6 Acknowledgement

The author would like to thank Professor Glenn Smith for his dedication in writing the original IEEE paper [8] on which much of this chapter is based. The author also acknowledges the contributions of the full research team as described in [16].

References

[1] M. D. Wright, W. Baron, J. Miller, J. Tuss, D. Zeppettella, and M. Ali, "Mems reconfigurable broadband patch antenna for conformal applications," *IEEE Transactions on Antennas and Propagation*, vol. 66, no. 6, pp. 2770–2778, 2018.

[2] M. Ali, N. Bishop, W. Baron, B. Smyers, J. Tuss, and D. Zeppettella, "A mems reconfigurable pixel microstrip patch antenna for conformal load bearing antenna structures (clas) concept," in *2014 IEEE Antennas and Propagation Society International Symposium (APSURSI)*, 2014, pp. 1093–1094.

[3] Z. Lou, L. Liao, Y. Wang, Y. Yang, J. Li, and S. Yan, "Frequency reconfigurable pixelated antenna using vo2 phase transition material," in *2025 IEEE 8th International Symposium on Electromagnetic Compatibility (ISEMC)*, 2025, pp. 1–3.

[4] J. Pal, K. Deshpande, L. Chomas, S. Santhanam, F. Donzelli, D. Piazza, J. A. Bain, and G. Piazza, "Magnetically actuated reconfigurable pixelated antenna," *2018 IEEE Micro Electro Mechanical Systems (MEMS)*, pp. 791–794, 2018.

[5] J. G. Maloney, M. P. Kesler, L. M. Lust, L. N. Pringle, T. L. Fountain, P. H. Harms, and G. S. Smith, "Switched fragmented aperture antennas," in *IEEE Antennas and Propagation Society International Symposium*, Salt Lake City, UT, Jul. 2000, pp. 310–313.

[6] L. N. Pringle, P. H. Harms, S. P. Blalock, G. N. Kiesel, E. J. Kuster, P. G. Friederich, R. J. Prado, J. M. Morris, and G. S. Smith, "A reconfigurable aperture antenna based on switched links between electrically small metallic patches," *IEEE Transactions on Antennas and Propagation*, vol. 52, no. 6, pp. 1434–1445, Jun. 2004.

[7] G. H. Huff and J. T. Bernhard, "Reconfigurable antennas," in *Modern Antenna Handbook*, C. A. Balanis, Ed. Wiley, 2007, ch. 8.

[8] L. N. Pringle, P. H. Harms, S. P. Blalock, G. N. Kiesel, E. J. Kuster, P. G. Friederich, R. J. Prado, J. M. Morris, and G. S. Smith, “A reconfigurable aperture antenna based on switched links between electrically small metallic patches,” *IEEE Transactions on Antennas and Propagation*, vol. 52, no. 6, pp. 1434–1445, Jun. 2004.

[9] R. T. Lee and G. S. Smith, “A design study for the basic TEM horn antenna,” *IEEE Antennas and Propagation Magazine*, vol. 46, no. 1, pp. 86–92, Feb. 2004.

[10] M. A. Towfiq, I. Bahceci, S. Blanch, J. Romeu, L. Jofre, and B. A. Cetiner, “A reconfigurable antenna with beam steering and beamwidth variability for wireless communications,” *IEEE Transactions on Antennas and Propagation*, vol. 66, no. 10, pp. 5052–5063, 2018.

[11] R. M. Bichara, F. A. Z. Asadallah, M. Awad, and J. Costantine, “A miniaturized reconfigurable antenna using quantum genetic algorithm optimization,” in *2021 IEEE International Symposium on Antennas and Propagation and USNC-URSI Radio Science Meeting (APS/URSI)*, 2021, pp. 763–764.

[12] M. Wright, M. Ali, W. Baron, J. Miller, J. Tuss, and D. Zeppettella, “Effect of bias traces and wires on a mems reconfigurable pixelated patch antenna,” in *2016 IEEE International Symposium on Antennas and Propagation (APSURSI)*, 2016, pp. 1429–1430.

[13] R. O. Ouedraogo, J. Tang, K. Fuchi, E. J. Rothwell, A. R. Diaz, and P. Chahal, “A tunable dual-band miniaturized monopole antenna for compact wireless devices,” *IEEE Antennas and Wireless Propagation Letters*, vol. 13, pp. 1247–1250, 2014.

[14] S. Tang, Y. Zhang, J. Rao, T. Qiao, C. Y. Chiu, and R. Murch, “Dual-port endfire millimeter wave reconfigurable antenna with optimized pixel surface,” in *2023 IEEE International Symposium on Antennas and Propagation and USNC-URSI Radio Science Meeting (USNC-URSI)*, 2023, pp. 969–970.

[15] T. Qiao, S. Tang, J. Rao, Y. Zhang, C. Y. Chiu, Q. S. Cheng, and R. Murch, “A novel optimization technique for designing frequency reconfigurable pixelated planar antenna,” in *2023 IEEE International Symposium on Antennas and Propagation and USNC-URSI Radio Science Meeting (USNC-URSI)*, 2023, pp. 1757–1758.

[16] J. G. Maloney *et al.*, “Chapters on antennas and fdtd methods,” in *Modern Antenna Handbook*, C. A. Balanis, Ed. Wiley, 2007, see Chapters 8, 12, and 30.

Chapter 6

Fragmented Array Elements

6.1 Direct Element Design

- direct element design
- use large scan paper to describe method for including scan (IEEE conf paper and slides)
- example of whole x-band for the IEEE paper
- 4:1 bandwidth
- discuss similarity to current sheets of munk and Harris
- usually balanced fed with differential feeds and electronics

6.2 First Success

[2].

Figure A.1 is a schematic drawing showing a typical volume in which Maxwell's equations are to be solved. The volume is divided into unit cells each of volume.

References

[1] K. S. Yee, "Numerical Solution of Initial Boundary Value Problems Involving Maxwell's Equations in Isotropic Media," IEEE Trans. Antennas Propagat., Vol. AP-14, pp. 302-307, May 1966.

[2] J. G. Maloney, G. S. Smith, and W. R. Scott, Jr., "Accurate Computation of the Radiation from Simple Antennas Using the Finite-Difference Time-Domain Method," IEEE Trans. Antennas Propagat., Vol. AP-38, pp. 1059-1068, July 1990.

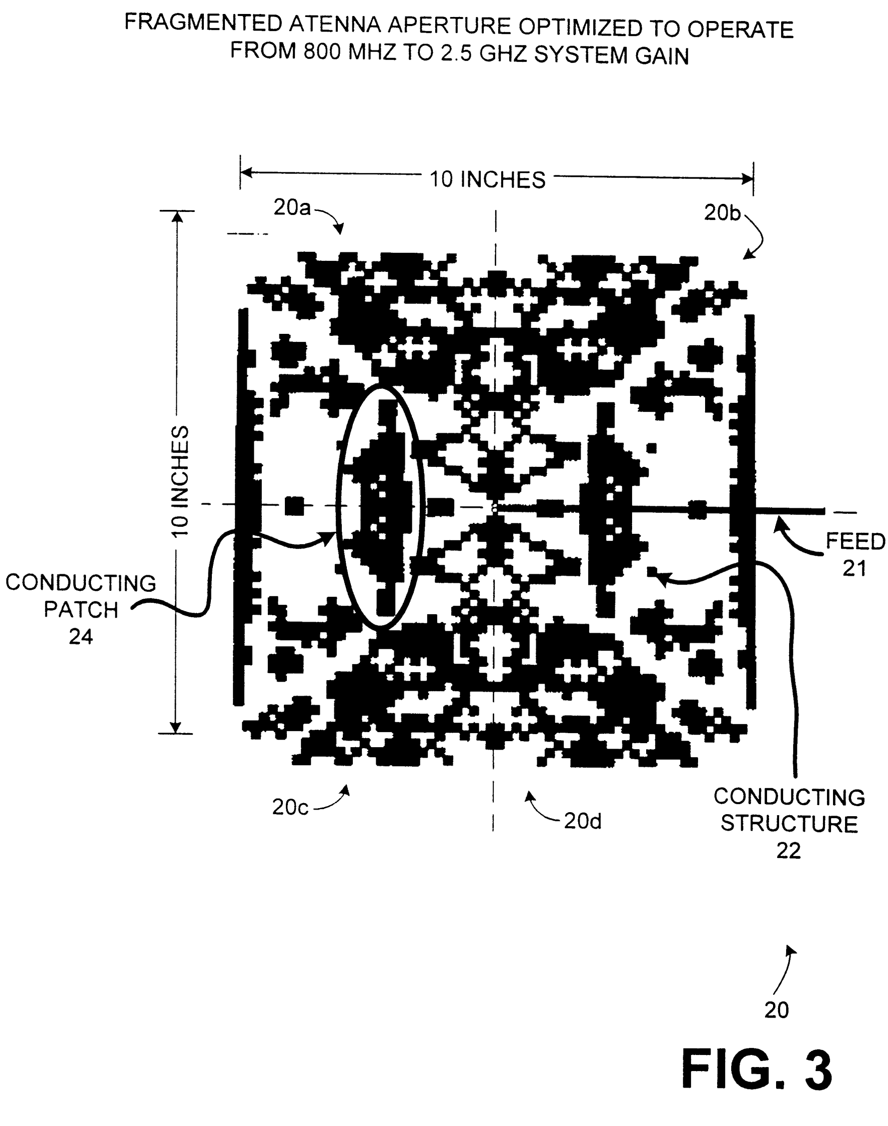

Figure 6.1: Comparison of fragmented design to uniform aperture limit $2\pi A/\lambda^2$

[3] J. J. Boonzaaier and C. W. Pistorius, “Thin Wire Dipoles ? A Finite-Difference Time-Domain Approach,” Electronics Lett., Vol. 26, pp. 1891-1892, 25 October, 1990.

[4] D. S. Katz, M. J. Picket-May, A. Taflove, and K. R. Umashankar, “FDTD Analysis of Electromagnetic Wave Radiation from Systems Containing Horn Antennas,” IEEE Trans. Antennas Propagat., Vol. AP-39, pp. 1203-1212, August 1991.

Chapter 7

Wideband Antenna Arrays

7.1 Introduction

Students of antenna design are taught that the gain of an array antenna can be estimated by multiplying the pattern of a single element by the array factor. This approach ignores mutual coupling between elements, which has traditionally been a major challenge for designers of phased arrays. Mutual coupling introduces areas of scan blindness—combinations of frequency and scan angle for which the array is poorly matched—that can severely degrade array performance. As the sophistication of numerical modeling codes has increased in concert with the availability of inexpensive parallel computing power, antenna designers have developed the ability to include the effects of mutual coupling in their performance predictions. This capability, in turn, suggests the possibility of *exploiting* mutual coupling rather than merely avoiding it.

To appreciate why wideband arrays are challenging, consider the performance comparison in Figure 7.1. A $10'' \times 10''$ aperture is populated with three different antenna types: a uniform current sheet (the theoretical ideal), a spiral antenna, and a bowtie antenna. The uniform current sheet achieves the full aperture gain limit across frequency, but it is a theoretical construct, not a realizable antenna. The spiral produces useful gain only over a limited bandwidth, and the bowtie exhibits narrow resonant peaks. Neither conventional design approaches the broadband performance that the aperture could support.

The fragmented aperture design approach, applied to array elements, offers a path to achieving the broadband performance that conventional element designs cannot. By allowing a genetic algorithm to optimize the conducting pattern of each unit cell—including connections between adjacent elements—the design process can exploit mutual coupling to produce arrays with bandwidths far exceeding those of conventional designs.

This chapter traces the development of wideband fragmented aperture arrays, beginning with the discovery that electrical connections between elements are essential for wide bandwidth. It then describes the broadband screen backplane, a key innovation that mitigates the half-wave nulls introduced by a ground plane, enabling practical planar arrays with bandwidths of 10:1 and beyond. The chapter continues with multi-layer

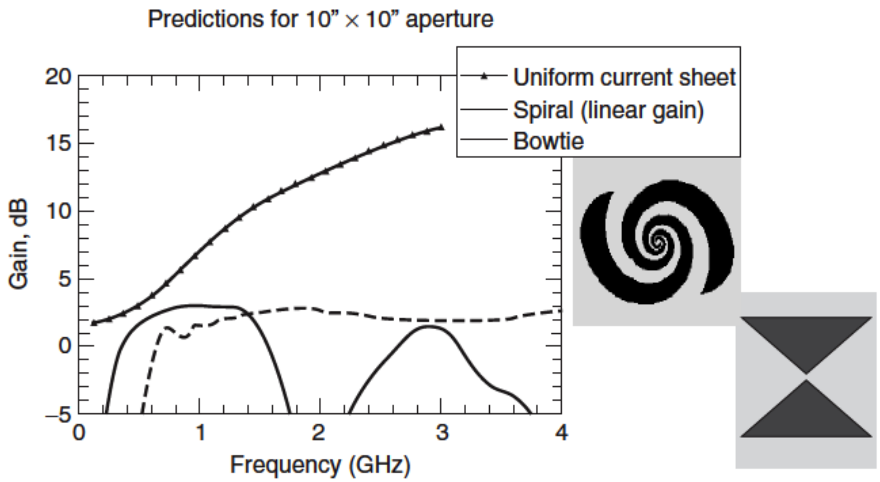

Figure 7.1: Predicted gain for three antenna types occupying a $10'' \times 10''$ aperture: a uniform current sheet (theoretical ideal), a spiral antenna, and a bowtie antenna. Neither the spiral nor the bowtie approaches the broadband aperture gain limit [1].

radiator designs that use parasitic face sheets to enhance front-to-back ratio, further extending achievable bandwidths to 33:1. Measured results from laboratory proof-of-concept arrays are presented throughout.

7.2 Connected Fragmented Array Elements

The fragmented aperture design approach extended naturally from single-element antennas to array elements. The key insight that led to a breakthrough in achievable bandwidths was the recognition that DC electrical connection between adjacent elements was not merely tolerable but actually beneficial and should be exploited. Subsequent multiple-octave array designs consistently featured these inter-element connections, which support continuous current paths spanning multiple elements.

The importance of connected arrays can be understood intuitively. In an array with an 8:1 bandwidth, the radiated wavelength changes from approximately two element widths at the highest frequency to 16 element widths at the lowest. For the array to radiate efficiently at the lowest frequencies, continuous conducting paths of sufficient length must be present on the aperture surface. With a connected array, such paths naturally exist.

To demonstrate the importance of inter-element connections, the 6-cm elements shown in Figure 7.2 were designed to operate from 0.25–2.5 GHz in an array with no ground plane. Two designs were compared: the first was optimized with electrical connections between elements permitted (a connected array), while the second was optimized with a boundary enforced around each element to prevent conducting pathways between elements. The realized gain achieved by an 8×8 finite array of each element

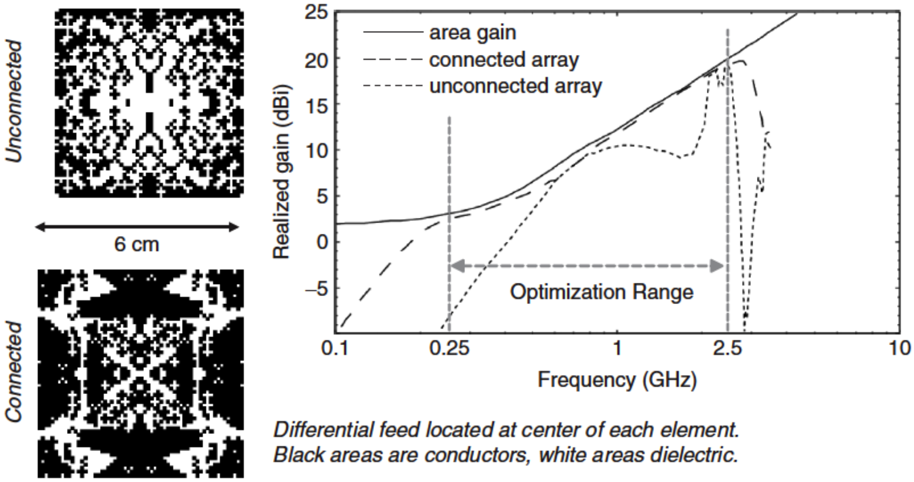

Figure 7.2: Design experiment comparing two 8×8 arrays: (a) connected array element, (b) unconnected array element, (c) embedded element gain comparison for a central element. The connected array element far outperforms the unconnected element [1].

design is shown in Figure 7.2(c). Because of the continuous current paths across element boundaries, the connected design maintains a good impedance match over the full 10:1 bandwidth and achieves markedly superior performance.

Another key feature of the connected geometry is that the overall size of the array becomes a limiting factor on the lowest operating frequency. When the connected element design of Figure 7.2 was modeled in arrays of various sizes (again without a ground plane), the low-frequency performance scaled proportionally with array size, as shown in Figure 7.3. Arrays of 2×2, 4×4, 8×8, and 16×16 elements were simulated. In all cases, the upper frequency limit remained relatively constant, being limited by the element lattice spacing and the onset of grating lobes. The low-frequency limit, on the other hand, was approximately proportional to the overall array dimension.

To confirm the validity of these simulation predictions, a fragmented array with 3-cm elements was designed and measured in 1999. The metric used was the embedded element realized gain (EERG), obtained by driving one central element while terminating all surrounding elements in matched resistive loads. The EERG measures the performance of a single element in the array environment and is a powerful diagnostic because angle-pattern cuts of the EERG can be used to predict the scan performance of a fully driven array. This approach greatly reduces measurement cost since beam-forming electronics are not required. As shown in Figure 7.4, the array achieves near aperture-limited gain at broadside over a 10:1 bandwidth, with excellent model-measurement agreement.

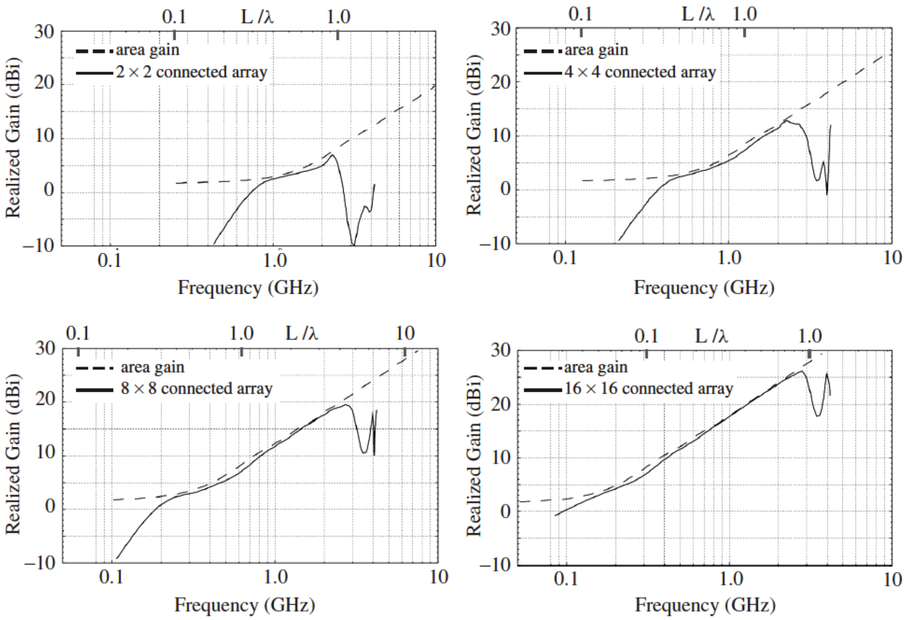

Figure 7.3: The connected element from Figure 7.2 simulated in arrays of various sizes. The low-frequency performance limit is approximately proportional to overall array size [1].

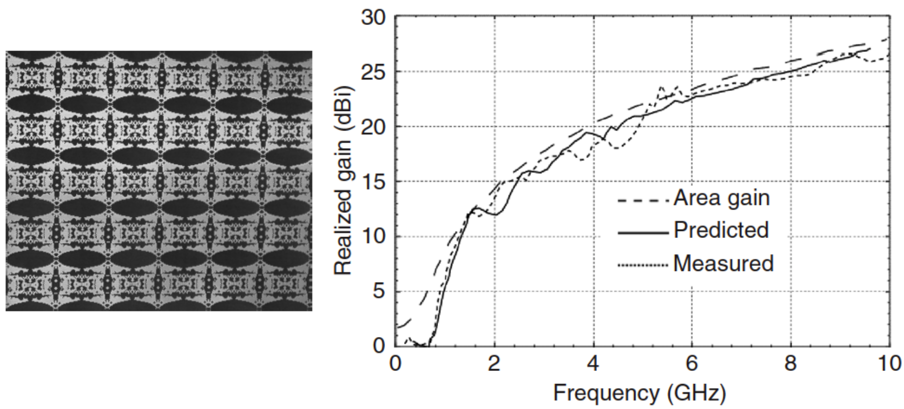

Figure 7.4: Embedded element realized gain (EERG) for a central element of a 10×17 array with 3-cm square unit cells, demonstrating 10:1 bandwidth with excellent model-measurement agreement [1].

7.3 Wideband Backplanes: Planar 10:1 Arrays

Early explorations of fragmented arrays (2000 and earlier) focused on fundamental questions of element connections, bandwidth limits, and natural impedance values [2]–[3]. These investigations typically either used no ground plane behind the radiating surface or accepted the limitations of simple ground planes. More recent work has demonstrated unbalanced feed designs for wideband phased arrays [4, 5] and broadband arrays with power combiners based on the fragmented aperture principle [6].

Ideally, a ground plane should be located $\lambda/4$ behind the radiating surface of a planar antenna. The backward-radiated energy travels a round-trip path of $\lambda/2$, accumulating $180°$ of phase, and the $180°$ phase inversion at the perfect electric conductor (PEC) surface of the ground plane causes the reflected energy to arrive in phase with the forward-going radiation. Wideband antennas pose a fundamental difficulty, however, since λ varies widely over the operating bandwidth. When the ground plane is $\lambda/2$ behind the radiating surface (or an integer multiple of $\lambda/2$), the backward-going radiation is reflected and arrives exactly out of phase with the forward radiation, producing a deep null in the gain.

This situation is illustrated in Figure 7.5, which shows the results of a simulation of a fragmented aperture radiator placed 2.5 cm in front of a PEC ground plane. The broadside gain is normalized to the area gain. Without the ground plane, the radiator is well matched across the band, but because it radiates in both directions, the forward radiation only approaches -3 dB, represented by the dashed line. With the ground plane, the gain approaches the maximum around 3 GHz, where 2.5 cm represents a quarter of the free-space wavelength and the ground plane provides nearly 3 dB of gain enhancement. At 6 GHz, however, the ground plane is a half wavelength behind the radiating surface, and a deep null appears. This null repeats at every integer multiple of $\lambda/2$ (12 GHz, 18 GHz, etc.). Practical experience indicates that fragmented aperture designs can be extended to approximately 8:1 bandwidths before the half-wave null must be addressed.

The problem is further complicated if the array is intended to scan over a significant volume, because the null frequency depends on the scan angle, as illustrated in Figure 7.6. As the scan angle moves away from broadside, the null frequency increases. The contour plot in the figure shows this trend clearly.

7.3.1 The Broadband Screen Backplane

Since the problem can be attributed to backward-radiated energy reflecting off the ground plane, one is tempted to address it with absorbing solutions. Interestingly, the Salisbury screen absorbing structure has the desirable characteristic that its tuned absorption frequency increases with incidence angle, exactly analogous to the scan angle–frequency dependence of the half-wave null. This was the inspiration for the *broadband screen backplane*, which was developed to extend the frequency performance of fragmented apertures over a ground plane.

The broadband screen backplane consists of one or more resistive card (r-card) layers placed between the radiating aperture and the PEC ground plane. Figure 7.7 shows the performance of a typical r-card layer placed halfway between the aperture layer

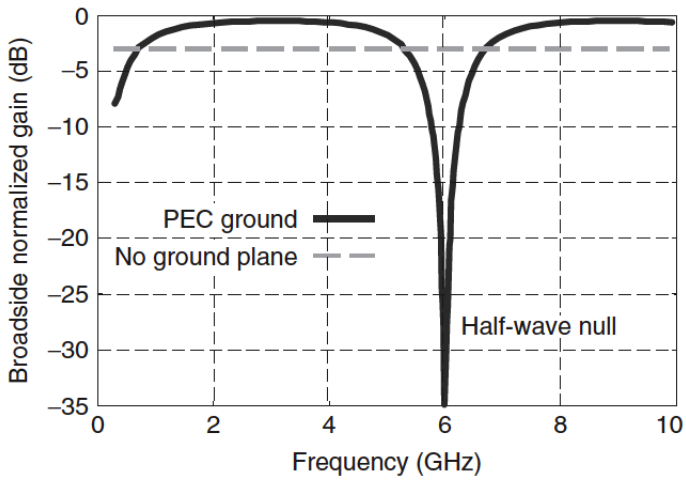

Figure 7.5: When a broadband radiating sheet is placed in front of a simple PEC ground plane, the resulting gain suffers nulls at frequencies where the separation distance is an integer multiple of $\lambda/2$ (in this case, 6 GHz for a 2.5-cm separation) [1].

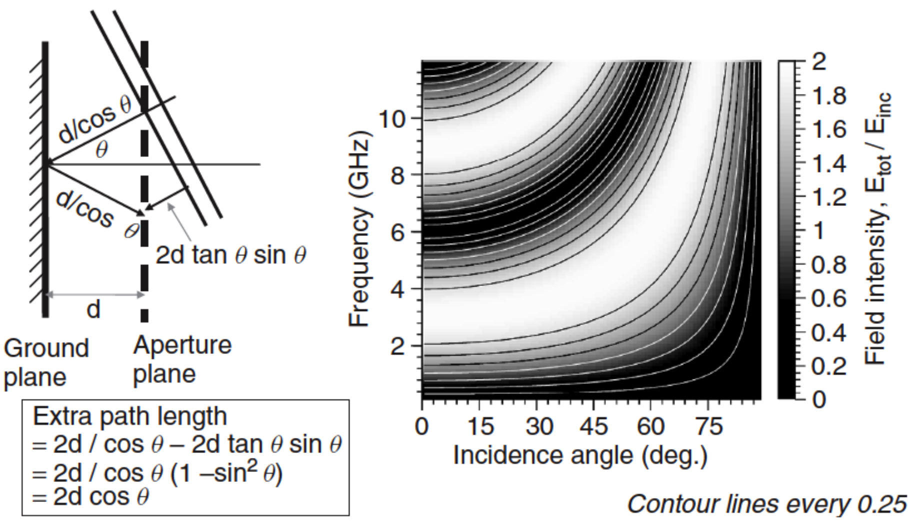

Figure 7.6: The half-wave null frequency depends on scan angle. Left: geometry illustration. Right: contour plot showing the relationship between field intensity at the radiating surface, frequency, and scan angle for a 2.5-cm separation [1].

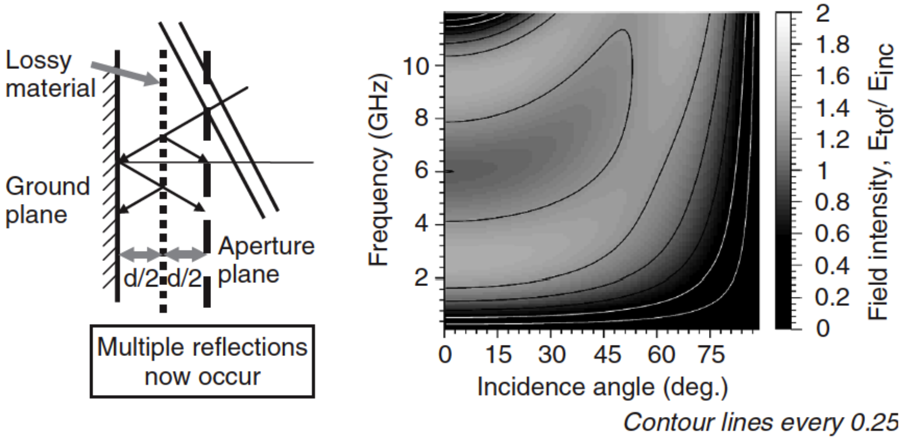

Figure 7.7: A 377 Ω/square r-card layer placed halfway between the radiating surface and the PEC ground plane (2.5-cm separation) eliminates the deep null at $\lambda/2$ [1].

and the ground plane. The backplane is most absorptive at exactly the frequency/angle combinations where the half-wave null occurs (and at every odd multiple of half wavelengths).

Figure 7.8 shows the normalized realized gain at broadside with this first-generation broadband screen backplane. The aperture has recovered enough gain at the problem frequency to achieve near 50% efficiency. However, one can do better. For overall antenna performance, the impedance value, position, and even the number of r-card layers may be treated as free variables in the design. For example, if the 377 Ω r-card is replaced with a 225 Ω card, the realized gain is maintained within 2 dB of the aperture limit across the operating band.

7.3.2 A 10:1 Proof-of-Concept Array

Figure 7.9 shows a 10:1 bandwidth design that was developed as a proof of concept using a single r-card broadband screen. The array demonstrated better than 50% efficiency over the operating band of 1–10 GHz. The plot on the right shows normalized predictions of realized gain, or equivalently, insertion loss. The upper curve (normalized gain) shows the effects of resistive loss alone, while the lower curve (normalized realized gain) shows the combined effects of resistive and mismatch loss. The separation between the two curves is a measure of the impedance match quality.

7.3.3 Multi-Layer Broadband Screen Backplanes

With a simple conducting ground plane behind a planar radiating surface, a standing wave occurs when the separation distance is $\lambda/2$ (or an integer number of half wavelengths), placing a field null at the radiating surface. The resulting impedance mismatch

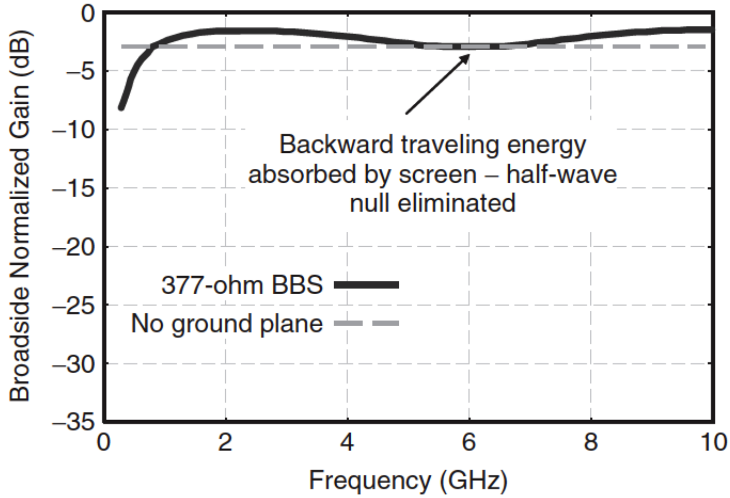

Figure 7.8: Normalized realized gain at broadside for the configuration of Figure 7.7, showing that the deep null at 6 GHz has been improved to approximately 3 dB insertion loss [1].

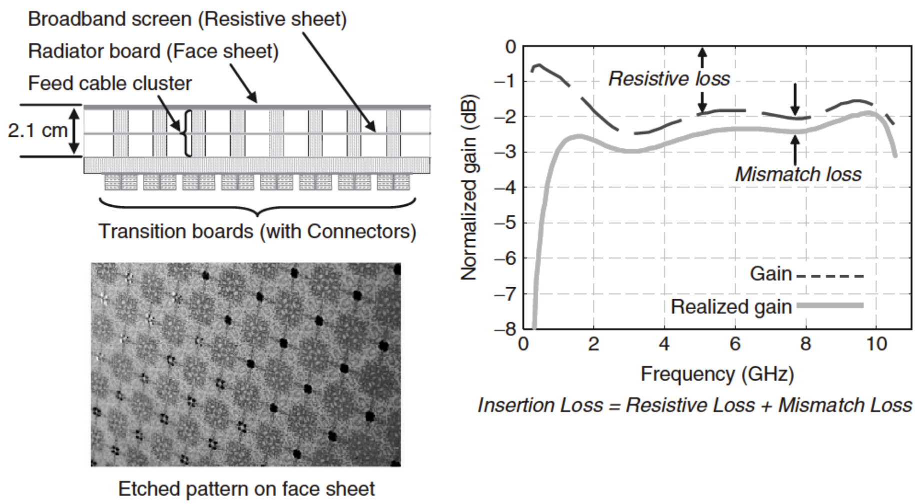

Figure 7.9: The first array built using the broadband screen backplane: a 10:1 design with efficiency better than 50% (< 3 dB insertion loss) from 1 to 10 GHz [1].

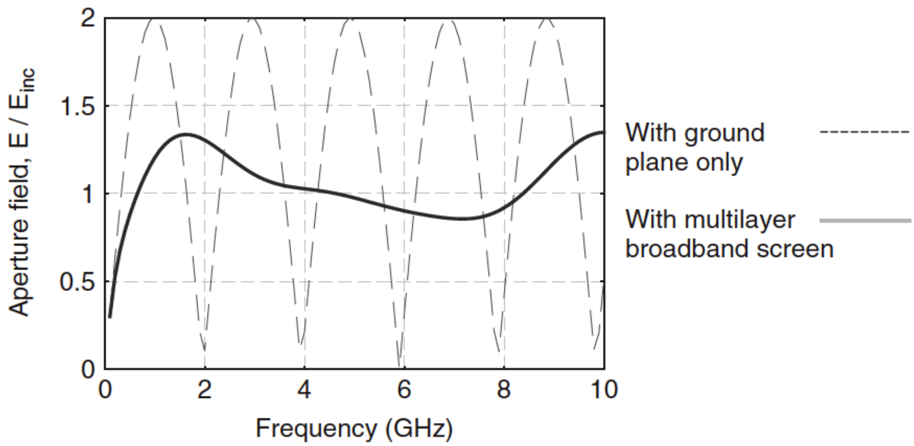

Figure 7.10: Aperture fields 3 inches in front of a PEC surface, with and without a broadband screen backplane [1].

causes the deep dropout in the gain curve. In addition to the energy they dissipate, r-cards inserted in the backplane stack introduce additional reflection boundaries that redistribute the standing wave to avoid field cancellation at the radiating surface.

As the operating bandwidth of the array spans more octaves, a simple ground plane introduces more half-wave nulls, and the problem of defeating the standing wave becomes more complex. Figure 7.10 shows an example of a radiating surface located three inches in front of a simple conducting ground plane. The resulting standing wave produces interference nulls approximately every 2 GHz. When the empty cavity is replaced by an optimized broadband screen with six r-card layers, the standing-wave nulls are eliminated. Figure 7.11 compares the performance of the empty cavity with the broadband screen over frequency and scan angle, demonstrating that the nulls are effectively controlled to scan angles of 60° or more.

7.4 Multi-Layer Radiators: 33:1 Bandwidth Arrays

A broadband screen backplane can control half-wave nulls, but it uses a loss mechanism to do so. While it is not necessary to attenuate all of the backward-radiated energy, some resistive loss is inevitable with this approach. A more desirable strategy would be to radiate energy preferentially into the forward hemisphere, thereby reducing the amount of backward-radiated energy that can reflect off the ground plane.

7.4.1 Directional Radiation from Thick Apertures

As a thought experiment, consider the ideal planar radiator with no thickness shown on the left in Figure 7.12. Radiation must occur equally into both hemispheres since nothing distinguishes one side from the other. However, if the radiating layer has some

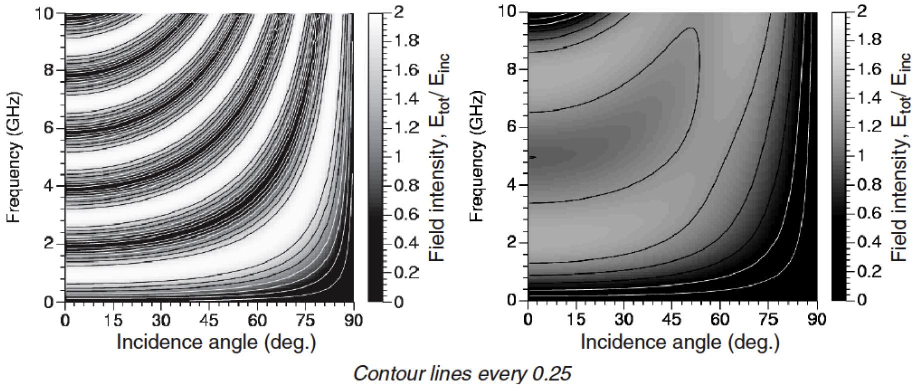

Figure 7.11: Contour plots comparing the configurations of Figure 7.10 over a range of scan angles. The broadband screen effectively eliminates standing-wave nulls to scan angles beyond 60° [1].

thickness, asymmetries may be introduced that cause the surface to radiate preferentially in one direction, as shown on the right in Figure 7.12. For example, if 90% of the energy is directed into the forward hemisphere, then even if the backward-radiated 10% is reflected and returns 180° out of phase, it will only reduce the transmitted power to 80% of the maximum value.

This principle can be exploited using multiple radiating layers in front of the ground plane. The additional layers may be actively driven or parasitic, analogous to the directors in a Yagi-Uda antenna.

7.4.2 Parasitic Layer Design Experiments

In Figure 7.13, two radiating layers approximately 8 mm apart with no ground plane were optimized using the fragmented aperture design process. The design goal was to maximize gain in the forward hemisphere. The plot shows the normalized forward-going and backward-going radiation, demonstrating good front-to-back ratio (F/B) over the upper octave of the design region (1–10 GHz). As the wavelength gets longer, the electrical separation between radiating layers becomes insufficient to direct the radiation.

The region of effectiveness for the parasitic-layer approach is sufficient to produce the 10:1 design of Figure 7.14, where the realized gain remains within 3 dB of the maximum across the band. This design is for illustrative purposes, as it does not include realistic feed structures or material loss.

The extent to which multiple radiating face-sheet layers improve the bandwidth depends on the number and spacing of the face sheets. Figure 7.15 shows designs using two and three face sheets, respectively. These simulations include realistic feed structures, but the ground planes have been replaced by perfectly matched absorbing layers. With two face sheets, the antenna exhibits enhanced gain over most of the upper

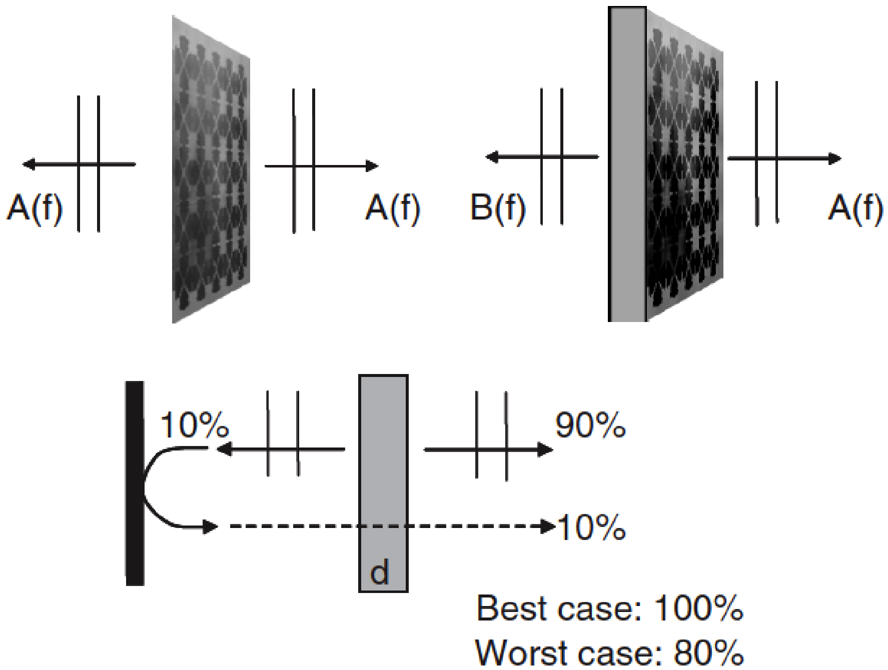

Figure 7.12: Thought experiment demonstrating the benefit of preferential forward radiation. A radiator with finite thickness can achieve asymmetric radiation (front-to-back ratio), mitigating the impact of ground plane reflections [1].

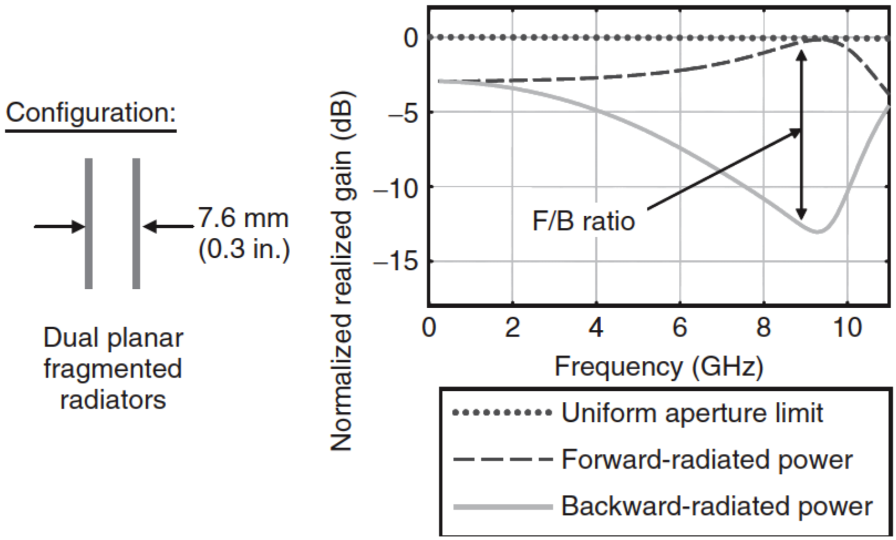

Figure 7.13: Idealized design with two simultaneously optimized radiating layers and no ground plane. The design goal was to maximize front-to-back ratio [1].

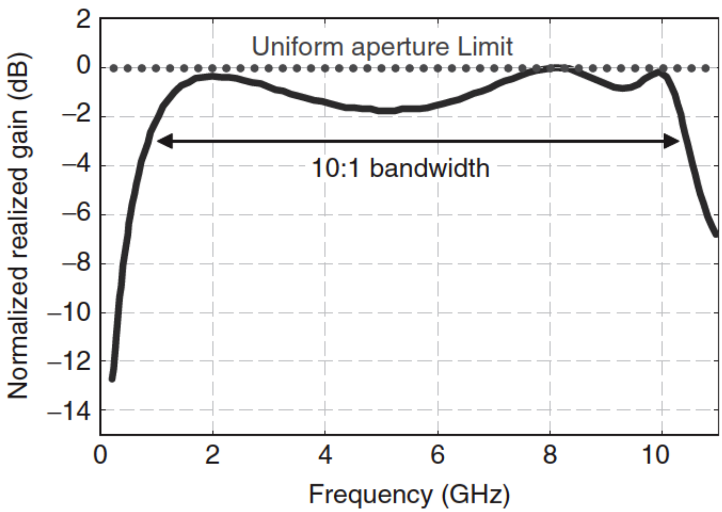

Figure 7.14: Parasitic layers directing radiation forward in the presence of a PEC backplane, keeping insertion loss below 2 dB over most of a 10:1 bandwidth [1].

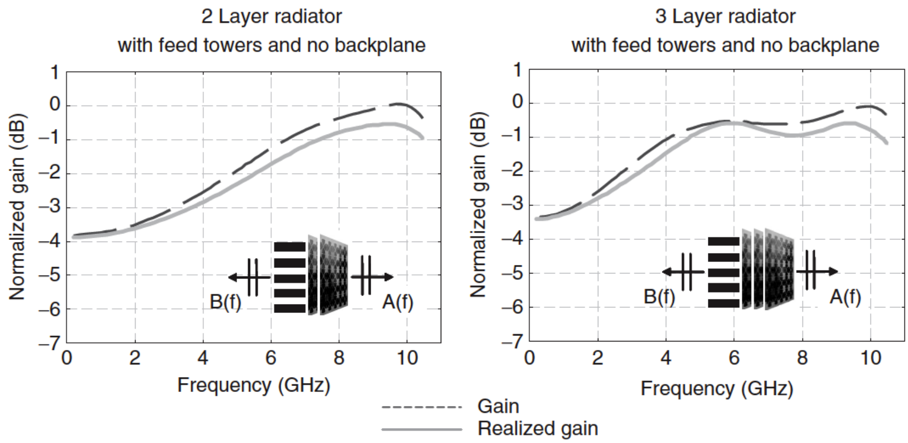

Figure 7.15: Design experiments with two and three radiating face sheets. The ground plane has been replaced in each simulation with a perfectly absorbing back boundary. Normalized gain levels above -3 dB indicate front-to-back ratio enhancement [1].

octave. With three, antenna gain is enhanced over the upper two octaves.

7.4.3 33:1 Proof-of-Concept Arrays

Design of fragmented elements for phased arrays with operating bandwidths beyond 10:1 requires a judicious combination of a multi-layer radiator with a broadband screen backplane. In partnership with Northrop Grumman Electronics Systems, the Georgia Tech Research Institute (GTRI) built and measured two laboratory proof-of-concept radiators with 33:1 bandwidths, each incorporating both design strategies. Each design consisted of a three-layer radiator stack over a six-r-card backplane stack. In the first design, two face sheets were driven by the feeds and the third was parasitic. To simplify the manufacturing process, the second design had only the innermost face sheet driven, with two parasitic outer layers.

Figure 7.16 shows the performance of the second design in a periodic simulation, which eliminates finite-array edge effects. The simulation includes realistic feed structures and material properties. Gain is normalized to the element area gain, so the 0 dB line represents ideal performance. The design achieves approximately 1 dB or better insertion loss over the upper octave, with better than 3 dB insertion loss over the entire 0.3–10 GHz design bandwidth.

7.4.4 33:1 Measured Results

The simulations were validated with measurements of a test piece on three different antenna ranges covering the entire operating bandwidth. The test antenna was a 23×23 element, dual-linear-polarized array with the center element actively driven and all surrounding elements terminated in matched 188 Ω impedances at the feed points. Fig-

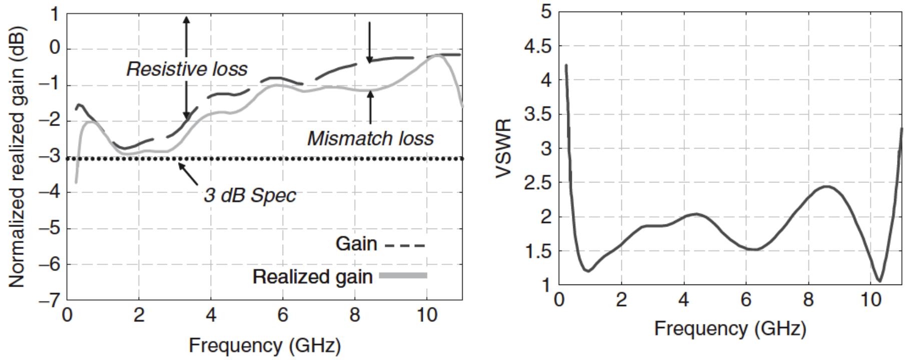

Figure 7.16: Predicted performance of the 33:1 antenna design in a periodic simulation, including realistic feed structures. Antenna efficiency is better than 50% over the entire 0.3–10 GHz bandwidth [1].

ure 7.17 illustrates the composition of one element of the array in cross section, with diagrams of the etched unit-cell pattern on each face sheet and a photograph of the test antenna.

Broadside frequency scans of the EERG are plotted in Figure 7.18. The figure compares measurement results at broadside to predictions. The element area gain (dashed line) represents the physical limit for antenna performance. The predicted EERG at broadside is shown as a solid line. Four measured data sets from three different antenna ranges are compared, including three different calibration horns spanning the 33:1 bandwidth. Data was measured on both V-pol and H-pol feeds (both should be equivalent at broadside for this symmetric design). The measured data show excellent consistency across ranges and at both sets of feed points, and excellent agreement with the predictions.

The measurements showed approximately 1 dB more insertion loss at the high end than predicted. The difference exceeds what can be attributed to resistive loss in the feed cables and on the metal radiating surfaces; it is likely due to slight imperfections in the assembly of the radiator. Performance at the high end is particularly sensitive to the position and planarity of the three face-sheet layers, and the planarity in the assembled test piece was affected by warping in the etched sheets.

This slight high-frequency offset is removed in Figure 7.19 to facilitate angle-pattern comparisons. These patterns allow detailed comparison of measured and modeled EERG over angle cuts at several discrete frequencies. Model-measurement agreement is excellent, with the models predicting features such as the ripple at 2 GHz due to finite-array edge effects and the narrowing of the scan volume above 8 GHz.

Figure 7.20 presents the measured EERG data from three overlapping data sets for H-plane scans and two for E-plane scans. The contour plots show angle cuts plotted horizontally at each frequency. Each angle cut has been normalized so that the maximum value at each frequency is zero (i.e., the frequency slope has been removed). The resulting image shows the achievable scan volume as a function of frequency for a fully

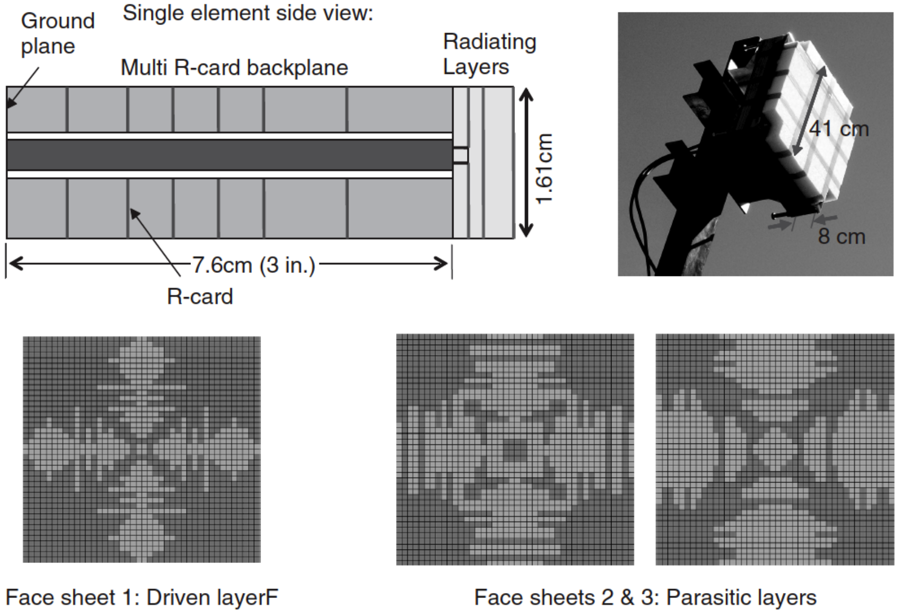

Figure 7.17: Construction details of the 33:1 antenna design, including a photograph of the 23 × 23 element test piece used to measure embedded element realized gain [1].

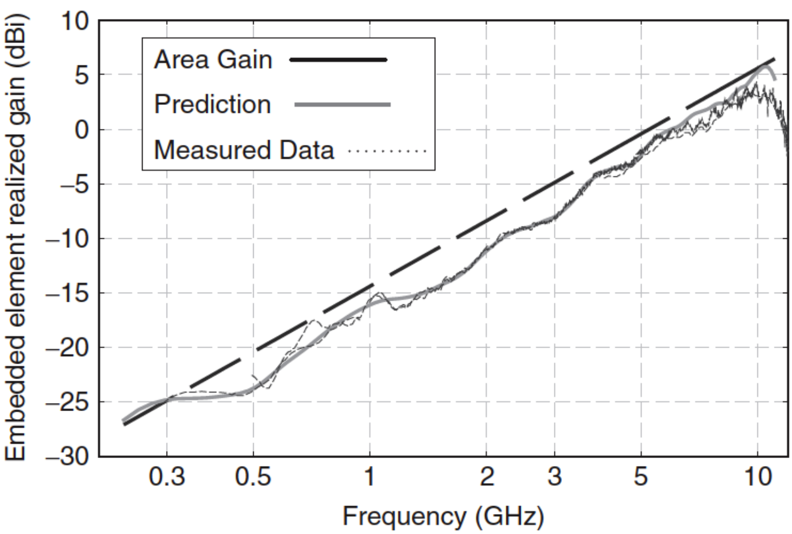

Figure 7.18: Compilation of measured EERG data at broadside for the 33:1 test antenna (three antenna ranges, two polarizations) compared with numerical predictions. The dashed line represents the element area gain [1].

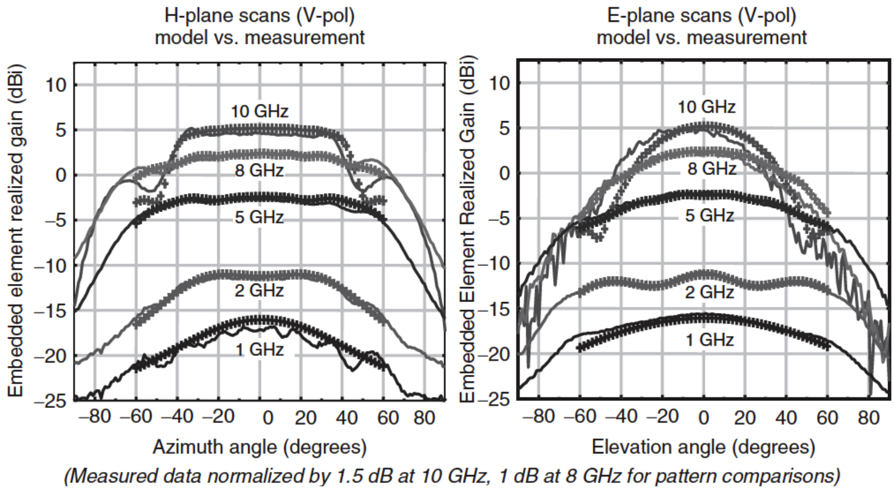

Figure 7.19: Comparison of modeled (solid lines) and measured (data markers) EERG pattern cuts at several discrete frequencies, showing excellent agreement [1].

driven array with this element design. The scan volume, as defined by the -3 dB points, is approximately $\pm 60°$ over most of the band, with some narrowing above 9 GHz in the H-plane and above 7 GHz in the E-plane. Notably, the scan volume shows no evidence of scan blindness anywhere in the operating bandwidth.

7.5 Design Rules and Scaling

Experience with several wideband phased array designs has produced empirical evidence for a useful rule of thumb regarding the thickness of these wideband radiators. Figure 7.21 compiles results for five fragmented array designs with bandwidths greater than an octave. Designs with bandwidths less than 10:1 used simple ground planes; antennas with bandwidths of 10:1 or greater incorporated broadband screen backplanes. In each case, the overall thickness is dictated not by the bandwidth but by the lowest operating frequency. For cavities filled with air or low-dielectric foams, the antenna thickness is approximately $\lambda/12$ at the lowest operating frequency.

7.6 Summary and Conclusions

The successful design of ultra-wideband phased arrays has been enabled by several factors. These designs require high-fidelity time-domain electromagnetic solvers. The necessity to optimize over many frequencies simultaneously would be prohibitively time-consuming with frequency-domain codes. All designs described in this chapter were developed using a finite-difference time-domain (FDTD) code (see Appendix A), the results of which are Fourier transformed to produce the requisite range of frequency

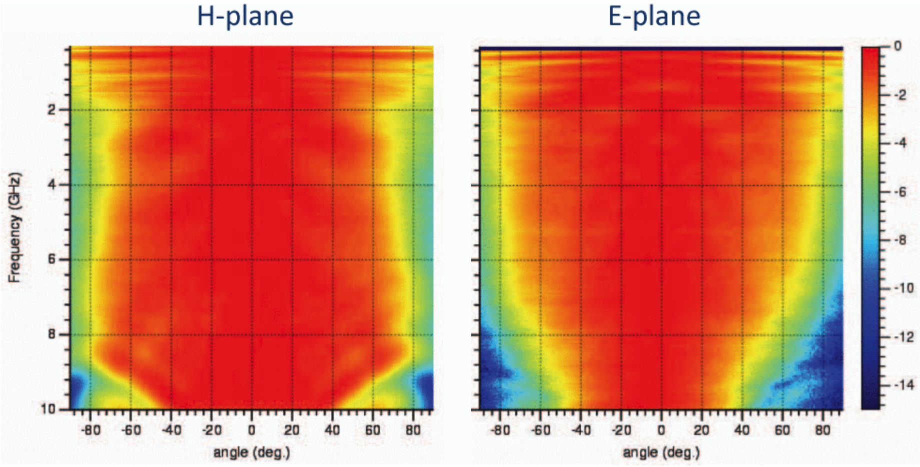

Figure 7.20: Compilation of measured EERG angle cuts normalized to the maximum at each frequency. The resulting contours indicate achievable scan volume. No scan blindness is observed within the operating bandwidth [7].

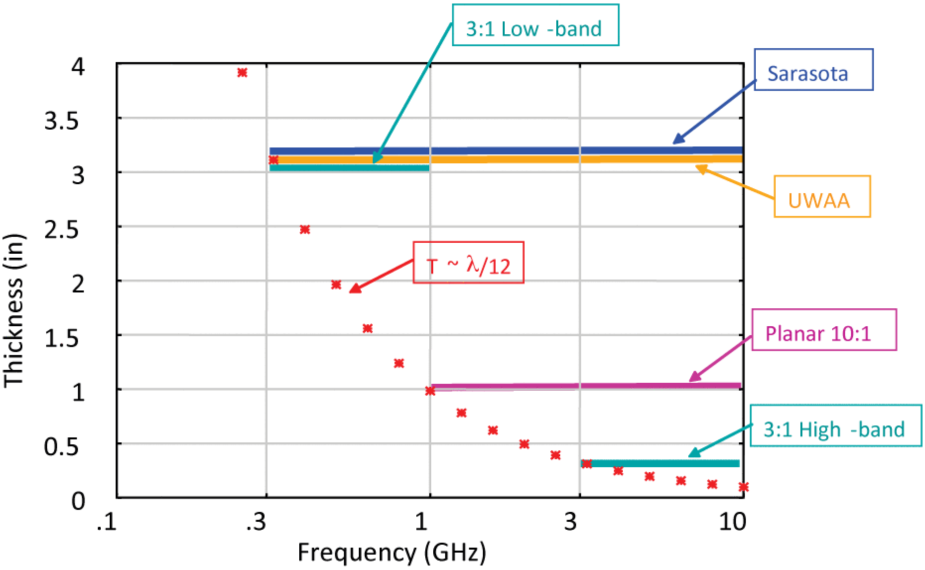

Figure 7.21: Results of several design exercises for fragmented arrays. For air-filled cavities, the antenna thickness is approximately $\lambda/12$ at the lowest operating frequency [7].

predictions. In early design stages, it is important to move through iterations rapidly to converge on a good initial design. In the final stages, accurate predictions are required to account for realistic details such as feed structures and material characteristics.

With the appropriate modeling tools and computing infrastructure, the essential features for ultra-wideband planar phased arrays were developed:

1. **Connected arrays** to span several octaves by supporting continuous current paths across element boundaries.

2. **Broadband screen backplanes** consisting of r-card layers to mitigate the half-wave nulls introduced by a conducting ground plane.

3. **Multi-layer radiators** using parasitic face sheets to enhance front-to-back ratio, leveraging the backplane improvements at lower frequencies.

4. **Fragmented aperture element design** to accomplish impedance matching in the presence of feed structures, material substrates, multiple layers, and mutual coupling.

Measured results confirm the success of these design strategies for bandwidths up to 33:1. Preliminary work suggests that phased array operation over bandwidths of 100:1 or more may be achievable.

[Note: The bullet-point outline for this chapter included a section on 100:1 bandwidth designs. This material is not yet available and should be added when ready.]

7.7 Acknowledgement

The author would like to thank Mr. Paul Friederich for his efforts in converting the original "How to make a 33:1 bandwidth array antenna" presentation into the handbook chapter [1] that served as the source material for this chapter.

References

[1] W. Croswell, T. Durham, M. Jones, D. Schaubert, P. G. Friederich, and J. G. Maloney, "Wideband arrays," in *Modern Antenna Handbook*, C. A. Balanis, Ed. John Wiley & Sons, 2011, ch. 12.

[2] J. G. Maloney, M. P. Kesler, P. H. Harms, T. L. Fountain, and G. S. Smith, "The fragmented aperture antenna: FDTD analysis and measurement," in *Millennium Conference on Antennas and Propagation (AP 2000)*, 2000, p. 93.

[3] P. Friederich, L. Pringle, L. Fountain, P. Harms, D. Denison, E. Kuster, S. Blalock, G. Smith, J. Maloney, and M. Kesler, "A new class of broadband planar apertures," in *Antenna Applications Symposium*, Sep. 2001, pp. 561–587.

[4] D. W. Landgren, D. J. P. Dykes, and K. W. Allen, "An unbalanced feed design for wideband phased arrays," *arXiv preprint arXiv:1706.04658*, 2017, international Telemetry Conference. [Online]. Available: https://arxiv.org/abs/1706.04658

[5] D. J. P. Dykes, K. M. Bowland, and K. W. Allen, “Wideband millimeter-wave fragmented aperture antenna,” in *2017 IEEE National Aerospace and Electronics Conference (NAECON)*, 2017, pp. 213–216.

[6] D. Landgren, T. Brunasso, K. Allen, D. Dykes, J. Kovitz, J. Perez, J. Dee, J. Marsh, C. Hunter, and G. Smith, “A broadband array with unbalanced feeds : Elements and power combiners based on the fragmented aperture principle,” in *2019 IEEE International Symposium on Antennas and Propagation and USNC-URSI Radio Science Meeting*, 2019, pp. 1223–1224.

[7] L. N. Pringle, P. H. Harms, S. P. Blalock, G. N. Kiesel, E. J. Kuster, P. G. Friederich, R. J. Prado, J. M. Morris, and G. S. Smith, “A reconfigurable aperture antenna based on switched links between electrically small metallic patches,” *IEEE Transactions on Antennas and Propagation*, vol. 52, no. 6, pp. 1434–1445, Jun. 2004.

Chapter 8

Designing Wide Scan Fragmented Array Antennas

8.1 Introduction

The previous chapters have demonstrated that fragmented aperture arrays can achieve remarkable bandwidths—up to 33:1 and beyond—while maintaining broadside gain that closely tracks the uniform aperture limit. However, one persistent challenge has been maintaining wide scan volume across the full operating bandwidth. This chapter addresses that challenge, describing design techniques that achieve scan volumes exceeding $\pm 60°$ across the entire design band.

Chapter 7 presented the development of ultra-wideband fragmented arrays, culminating in a 33:1 bandwidth proof-of-concept array. Figure 8.1 shows the measured and predicted embedded element realized gain for that array, confirming excellent agreement between model and measurement across three independent measurement facilities. The broadside gain tracks the uniform aperture area limit well across the 0.3 to 10 GHz design band, and the inset photograph shows the array on the outdoor measurement range.

Despite the excellent broadside performance, this array exhibited a shortcoming in its scan volume. As discussed in Chapter 7 (see Figure 7.20), the principal-plane antenna patterns for the 33:1 array show wide scan volume ($> \pm 60°$) across most of the operating band. However, near the top of the band (approximately 8.5 to 10 GHz), a significant narrowing of the scan volume is evident, reducing the usable scan range to roughly $\pm 40°$. In the years since the design of the 33:1 antenna, preventing this upper-band scan volume narrowing has been an active area of research.

A second shortcoming of the 33:1 array is related to aperture efficiency. As visible in Figure 8.1, the array was within 3 dB of the uniform aperture gain limit (better than 50% aperture efficiency), but the majority of the loss was attributable to the resistive backplane required to suppress the ground-plane nulls over such a large bandwidth. This loss limits the array to receive-only or low-power transmit applications.

This chapter describes progress in overcoming these two limitations. First, an im-

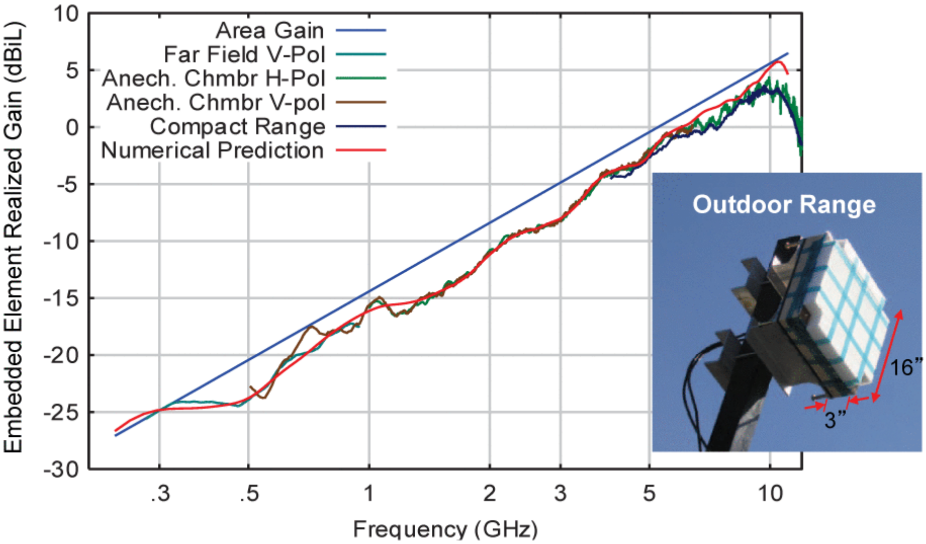

Figure 8.1: Measured and predicted embedded element realized gain (EERG) for the 33:1 bandwidth array. The broadside gain (red line) tracks the uniform aperture area limit (blue line) across the 0.3 to 10 GHz design band. Measurements from three independent facilities (anechoic chamber, compact range, and outdoor range) confirm the model accuracy. Inset: the array on the outdoor measurement range [1].

proved design process using spectral-domain FDTD simulation enables the genetic algorithm to optimize scan performance directly, alleviating the upper-band scan volume narrowing without requiring tighter inter-element spacing. Second, for applications that do not require the extreme bandwidth of the 33:1 design, a simpler antenna structure can be used that avoids the introduction of resistive loss, enabling high-efficiency operation suitable for transmit applications. Third, a laminated printed circuit board (PCB) fabrication approach replaces the traditional machined aluminum construction, yielding a more integrated, mass-producible antenna. These advances are illustrated through the design of a wide-scanning (±60°), whole X-band (8–12 GHz) phased array element.

8.2 Fabrication Approaches

8.2.1 Traditional Construction

Early fragmented aperture array antennas were constructed using the approach depicted in Figure 8.2. This design consists of an array of elements printed on circuit board material, suspended over a conducting ground plane by machined aluminum feed towers. The feed towers enclose differential coaxial lines that provide the dual-polarized excitation to each antenna element. Combining networks and beamforming electronics connect to these coaxial lines in the space behind the ground plane.

This construction method can produce lightweight structures; for example, a 0.6 m × 0.6 m array built in this manner weighed only 4 kg for the entire antenna assembly. This basic construction has been used to build many successful wideband fragmented aperture designs over the past two decades, including the 33:1 bandwidth array and the various designs summarized in the thickness-versus-frequency chart in Chapter 7 (Figure 7.21).

8.2.2 Laminated Printed Circuit Board Construction

While the traditional machined construction produces excellent antenna performance, it is not ideal for mass production, particularly at higher frequencies where the mechanical tolerances become demanding. An alternative approach, shown in Figure 8.3, builds the entire antenna from laminated printed circuit board layers.

In this approach, the fragmented conducting layers, the dielectric spacers between them, and the ground plane are all integrated into a single laminated PCB stack-up. The element feeds, which were previously machined coaxial lines enclosed in aluminum towers, are now implemented as closely spaced plated vias manufactured using standard multi-layer PCB techniques. Feed networks can also be implemented as additional PCB layers, producing a highly integrated antenna panel.

The PCB approach offers several practical advantages. It leverages mature, high-volume PCB manufacturing processes, resulting in antennas that are more repeatable, more easily mass-produced, and potentially less expensive than machined alternatives. These benefits are especially significant at X-band and higher frequencies, where the small feature sizes make machined construction increasingly difficult.

However, the laminated PCB approach also introduces new design challenges:

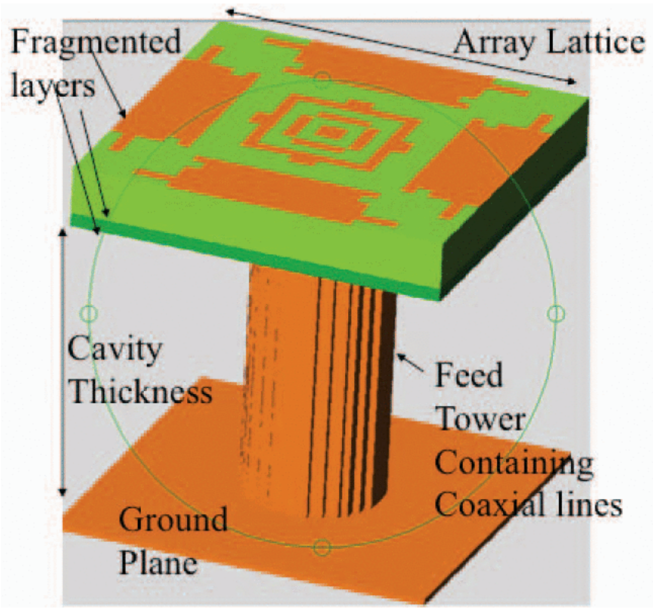

Figure 8.2: Traditional fragmented aperture array construction. Fragmented layers are printed on circuit board material and separated by foam spacers above a machined aluminum ground plane. Feed towers enclose differential coaxial lines that connect to the dual-polarized elements [1].

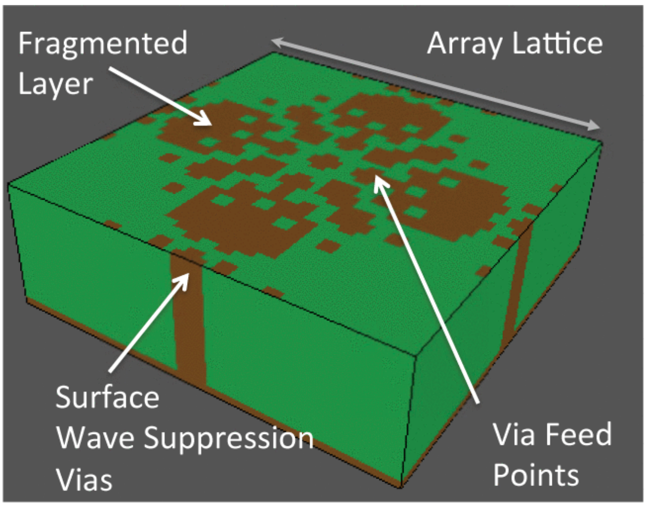

Figure 8.3: Laminated printed circuit board (PCB) fabrication approach. The entire antenna—fragmented layers, dielectric spacers, and ground plane—is built up as a multi-layer PCB stack. Element feeds are plated vias near the center of each unit cell, and surface wave suppression vias are placed near the perimeter [1].

- **Surface wave suppression.** Thick dielectric substrates can support surface waves that cause scan blindness—a condition where the array becomes poorly matched at specific combinations of frequency and scan angle. To prevent this, surface wave suppression vias must be incorporated into the laminated stack-up as an integral part of the design. These vias are visible near the perimeter of the unit cell in Figure 8.3.

- **Dielectric loading.** The presence of dielectric material throughout the cavity between the radiating layers and the ground plane changes the effective wavelength and alters the impedance environment seen by the antenna elements. The design process must account for the specific dielectric properties of the PCB substrate materials.

- **Modified feed structures.** The feeds are no longer simple 50 Ω coaxial lines in air; they are closely spaced vias in a dielectric environment. The characteristic impedance and coupling behavior of these via-based feeds must be accurately modeled during the design process.

All of these effects are captured naturally by the FDTD simulation used in the genetic algorithm design process, so no special analytical treatment is required. The full-wave simulation simply includes the dielectric layers, the vias, and the complete PCB stack-up geometry, and the optimizer works with the true electromagnetic behavior of the structure.

8.3 Spectral-Domain FDTD for Wide Scan Optimization

8.3.1 Limitations of Standard Periodic Boundary Conditions

The design process for fragmented aperture array elements uses a genetic algorithm to optimize a single unit cell of the array, terminated by periodic boundary conditions (PBC) that simulate an infinite array environment. The FDTD method is ideal for this purpose because a single time-domain simulation produces the full frequency-domain response across the entire design bandwidth.

In the standard FDTD implementation of periodic boundary conditions, the PBC is applied as a wrap-around boundary at the edges of the unit cell. This approach naturally models the infinite array at broadside (zero scan angle) and provides the complete broadband response in a single simulation. This is the approach that was used to design the earlier fragmented aperture arrays, including the 33:1 bandwidth design.

However, standard broadside-only PBC does not provide information about the array's scan performance. The scan volume narrowing observed in the 33:1 array (Figure 7.20) was a consequence of optimizing only for broadside performance: the genetic algorithm had no information about off-broadside behavior, so it had no mechanism to prevent scan volume degradation.

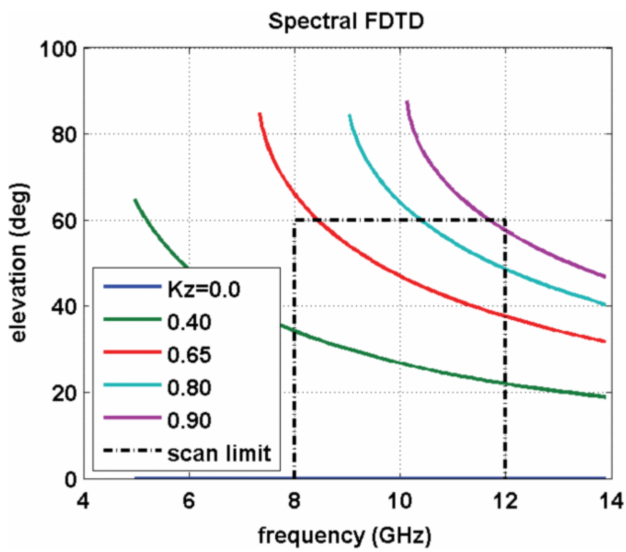

Figure 8.4: Elevation angle versus frequency contours for several normalized transverse wavenumbers K_z used in the spectral-domain FDTD design process. The dashed box indicates the target 8–12 GHz, $\pm 60^\circ$ scan volume. Because the contours are not constant versus frequency, the transverse wavenumber values are chosen to provide denser sampling at higher frequencies and larger scan angles, where scan problems are most likely to occur [1].

8.3.2 The Spectral-Domain FDTD Approach

To incorporate scan performance into the design process, a spectral-domain FDTD approach to periodic boundary conditions [3] was integrated into the design suite. In the spectral-domain formulation, the FDTD simulation is performed at a fixed transverse wavenumber (k_x, k_y) rather than at a fixed scan angle (θ, ϕ). The PBC is still implemented as a wrap-around boundary, but the constant transverse wavenumber assumption means that the effective scan angle is frequency dependent.

Figure 8.4 illustrates this relationship. Each curve shows the elevation angle as a function of frequency for a specific normalized transverse wavenumber K_z. The dashed box indicates the target design space: the 8–12 GHz X-band with a scan volume of $\pm 60^\circ$. Because the contours are not horizontal (i.e., constant angle versus frequency), a single spectral-domain simulation does not map to a single scan angle. Instead, each simulation sweeps through different scan angles as it sweeps through frequency.

8.3.3 Sampling the Scan Volume

The key to successful wide-scan design is to strike the right balance between sampling the scan volume sufficiently and not performing too many simulations (since each simulation adds to the computational cost of every fitness evaluation in the genetic algorithm). The exact number of spectral-domain simulations needed is problem specific, but a useful observation guides the selection of wavenumber samples: poor scan performance, when it occurs, typically manifests at higher frequencies and larger scan angles.

As shown in Figure 8.4, the transverse wavenumber values are chosen to concentrate the sampling in the region of the scan volume where problems are most likely—the upper-right portion of the frequency-angle space. The $K_z = 0$ contour corresponds to broadside at all frequencies, while progressively larger values of K_z sweep through progressively larger scan angles. By including several such simulations in the fitness evaluation, the genetic algorithm receives information about both broadside and off-broadside performance and can optimize accordingly.

This approach adds computational cost to each fitness evaluation, since multiple spectral-domain FDTD simulations must be run for each candidate element design. However, the cost is manageable because the number of required wavenumber samples is typically small (on the order of five to ten), and each individual simulation is no more expensive than the single broadside simulation used in the previous design approach.

8.4 Example: Whole X-Band Array Element

8.4.1 Design Parameters

To illustrate the improved design process and the PCB fabrication approach, a whole X-band (8–12 GHz) phased array element was designed with a target scan volume of $\pm 60°$ in all azimuth planes. The X-band was chosen because it represents a practical frequency range for military radar and communications applications, and because typical printed circuit board elements (e.g., microstrip patches) are not broadband enough to cover the full 8–12 GHz band in a low-profile PCB form factor.

The design begins by selecting the array lattice constant to prevent grating lobes at the maximum scan angle and highest operating frequency:

$$\frac{s}{\lambda_{\text{high}}} = \frac{1}{1 + \sin\theta_{\max}} = 0.536 \quad \text{for } \theta_{\max} = 60° \tag{8.1}$$

where s is the element spacing and λ_{high} is the free-space wavelength at the highest operating frequency (12 GHz).

Next, the number of fragmented pixels across the unit cell is selected using the rules of thumb described in Chapter 3: typically 20–30 pixels across the unique quadrant of the element (as illustrated in Figure 8.3). The element is then designed using the genetic algorithm approach with the spectral-domain FDTD providing the fitness evaluation at the normalized K_z and K_y values shown in Figure 8.4.

8.4.2 Broadside Performance

After the genetic algorithm completes the design, the element performance is verified by simulating a large finite array—in this case, 21×21 elements. The embedded element realized gain is obtained by computing the gain of the central element while all surrounding elements are terminated in matched loads.

Figure 8.5 shows the broadside embedded element realized gain as a function of frequency. The gain is within approximately 0.2 dB of the uniform aperture area limit across the entire 8–12 GHz design band. This near-ideal aperture efficiency demonstrates that the PCB fabrication approach, with its dielectric loading and via-based feeds, does not compromise the ability of the fragmented aperture design to efficiently utilize the available aperture area.

8.4.3 Impedance Match

Figure 8.6 compares the VSWR for the embedded element with the VSWR for the infinite array scanned at broadside. Both are well below 2:1 across the design band, but they are not identical. The difference arises because the infinite-array VSWR includes the mutual coupling from all neighboring elements, whereas the embedded element VSWR reflects the impedance seen at the terminals of a single element in the finite array environment.

An important point for phased array design is that it is the *scanned* VSWR (the infinite-array value) that must be kept small, because this is the impedance that the element presents to the beamforming network during scanning. The embedded element VSWR may actually be higher than the scanned VSWR when significant mutual coupling is being exploited to improve the scanned impedance match. This is another example of how the fragmented aperture design approach embraces mutual coupling rather than attempting to minimize it.

8.4.4 Scan Performance

Figures 8.7 through 8.9 show the embedded element realized gain as a function of both azimuth and elevation angle at three frequencies spanning the X-band: 8 GHz (bottom), 10 GHz (middle), and 12 GHz (top). These plots are obtained by simulating the 21×21 finite array with the central element excited and all others terminated, then computing the realized gain pattern of the central element.

At 8 GHz (Figure 8.7), the scan volume is excellent, with strong realized gain extending well beyond 60° in both azimuth and elevation. At 10 GHz (Figure 8.8), the wide scan volume is maintained. At 12 GHz (Figure 8.9), there is some slight degradation in the scan volume in the azimuth direction, but the overall scan performance still substantially exceeds $\pm 60^\circ$.

This is a dramatic improvement over the scan performance of the 33:1 array element (Figure 7.20), which showed significant scan volume narrowing to only $\pm 40^\circ$ in the upper portion of its operating band. The key difference is that the spectral-domain FDTD design process gives the genetic algorithm direct information about the scan performance, allowing it to optimize for wide scan and wide bandwidth simultaneously.

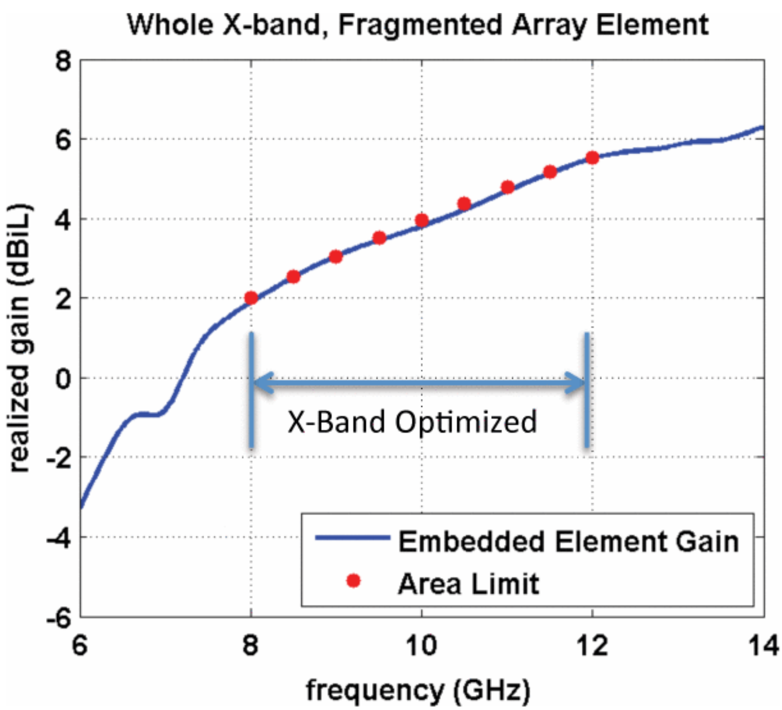

Figure 8.5: Broadside embedded element realized gain for the whole X-band fragmented array element (blue line) compared to the uniform aperture area limit (red dots). The realized gain is within approximately 0.2 dB of the theoretical limit across the 8–12 GHz design band [1].

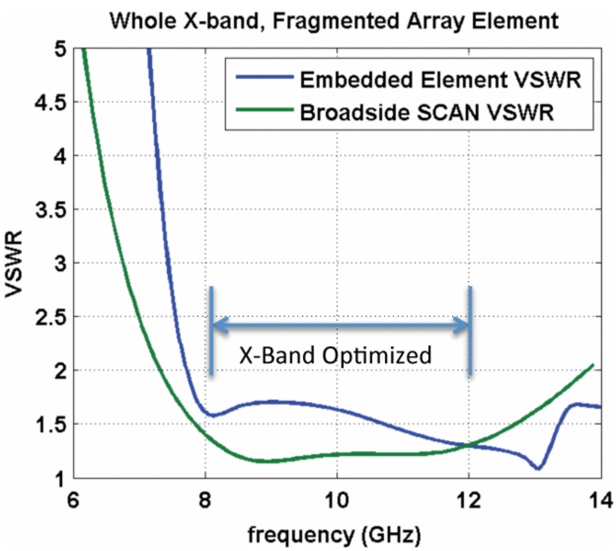

Figure 8.6: VSWR comparison for the X-band fragmented array element. The embedded element VSWR (blue line) and the broadside infinite-array scan VSWR (green line) are both below 2:1 across the design band. The difference between the two reflects the influence of mutual coupling from neighboring elements [1].

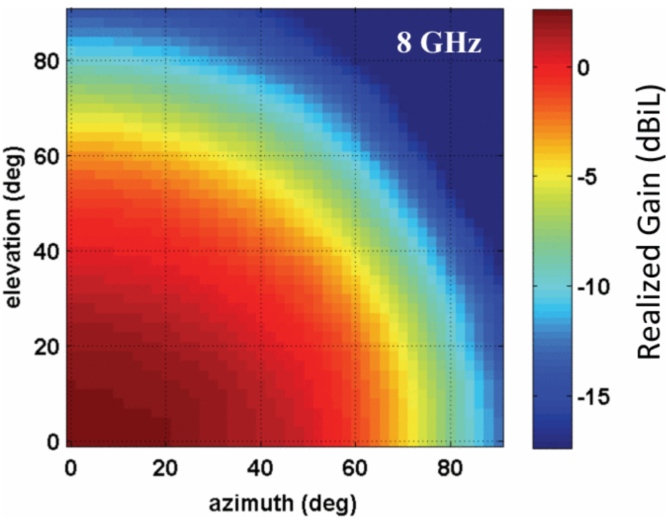

Figure 8.7: Embedded element realized gain at 8 GHz as a function of azimuth and elevation angle for the V-pol feed. The wide scan volume is evident, with usable gain extending well beyond 60° in both planes [1].

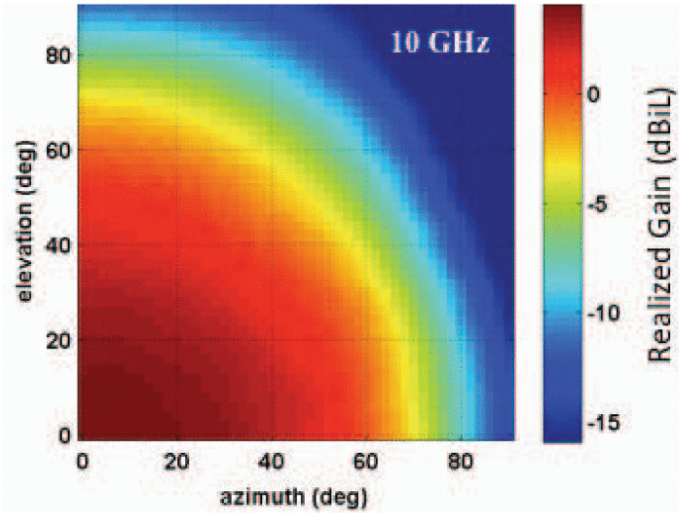

Figure 8.8: Embedded element realized gain at 10 GHz. The wide scan volume ($> \pm 60°$) is maintained at the center of the X-band [1].

8.5 Discussion

8.5.1 Bandwidth–Efficiency–Scan Trade Space

The results of this chapter highlight an important trade space in fragmented aperture array design. The 33:1 bandwidth array described in Chapter 7 achieved extraordinary bandwidth but required a lossy broadband screen backplane to suppress ground-plane nulls, limiting the array to receive-only applications. The X-band element described in this chapter achieves a more modest bandwidth (approximately 1.5:1) but does so without the need for a lossy backplane, enabling high-efficiency, transmit-capable operation.

This trade-off is a fundamental consequence of the physics. As discussed in Chapter 7, the broadband screen backplane uses resistive card (r-card) layers to prevent the half-wave nulls that occur when the aperture-to-ground-plane spacing is an integer multiple of $\lambda/2$. For very large bandwidths, these nulls cannot be avoided without some form of loss. For moderate bandwidths (on the order of 2:1 to 3:1), the aperture thickness can be chosen so that no half-wave nulls fall within the operating band, eliminating the need for lossy backplane layers entirely.

8.5.2 PCB Design Rules

The design rules and scaling relationships discussed in Chapter 7 (Section 7.6) apply to the PCB approach as well, with one important modification. The $\lambda/12$ rule of thumb

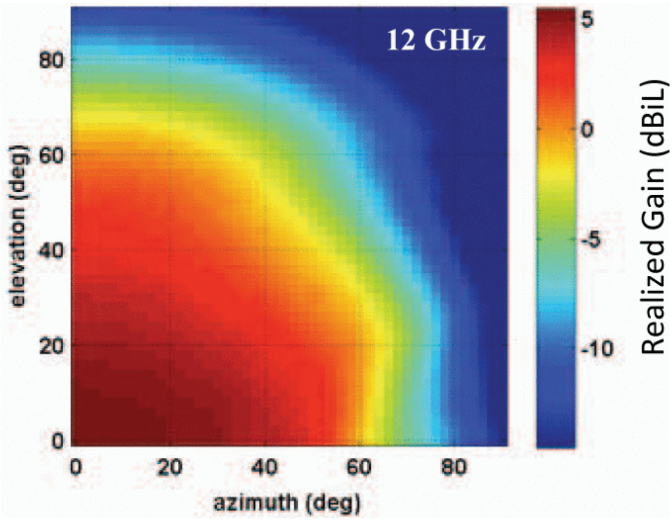

Figure 8.9: Embedded element realized gain at 12 GHz. Some slight reduction in the scan volume is visible in the azimuth direction, but the overall scan volume still substantially exceeds $\pm 60°$ [1].

for cavity thickness (Figure 7.21) was derived from air-filled cavity designs. For the PCB approach, the cavity is dielectrically loaded, so the relevant wavelength is the wavelength in the substrate material. The modified rule of thumb is:

$$T \approx \frac{\lambda_{\text{substrate}}}{12} = \frac{\lambda_0}{12\sqrt{\epsilon_r}} \tag{8.2}$$

where λ_0 is the free-space wavelength at the lowest operating frequency and ϵ_r is the relative permittivity of the substrate. This dielectric loading results in a physically thinner antenna, which is one of the practical benefits of the PCB approach.

[TODO: Include a thickness vs. frequency chart for PCB designs analogous to the air-filled cavity chart in Chapter 7, once enough PCB designs have been completed to establish the trend.]

8.6 Summary and Conclusions

This chapter described three advances that address key limitations of earlier fragmented aperture array designs:

1. **Spectral-domain FDTD for wide scan optimization.** By incorporating a spectral-domain FDTD approach to periodic boundary conditions into the genetic algorithm design process, the optimizer gains direct information about the array's scan performance at multiple angles. This enables the design of elements with scan volumes exceeding $\pm 60°$ across the full operating bandwidth, a significant improvement over designs optimized only at broadside.

2. **Laminated PCB fabrication.** Replacing the traditional machined aluminum construction with a laminated printed circuit board approach yields a more integrated, more easily mass-produced, and potentially lower-cost antenna, with particular advantages at X-band and higher frequencies where machining tolerances are demanding.

3. **High-efficiency, transmit-capable designs.** For applications with moderate bandwidth requirements (on the order of 1.5:1 to 3:1), the antenna can be designed without a lossy broadband screen backplane, resulting in high aperture efficiency suitable for transmit applications.

These advances were demonstrated through the design of a whole X-band (8–12 GHz) phased array element that achieves broadside gain within 0.2 dB of the uniform aperture area limit and a scan volume exceeding $\pm 60°$ across the design band, all in a laminated PCB form factor.

References

[1] J. G. Maloney, B. N. Baker, R. T. Lee, G. N. Kiesel, and J. J. Acree, "Wide Scan, Integrated Printed Circuit Board, Fragmented Aperture Array Antennas," in Proc. 2011 IEEE International Symposium on Antennas and Propagation, Spokane, WA, July 2011, pp. 1965–1968.

[2] J. G. Maloney, M. P. Kesler, P. H. Harms, and G. S. Smith, Fragmented Aperture Antennas and Broadband Ground Planes, U.S. Patent No. 6,323,809 B1, November 27, 2001.

[3] A. Aminian and Y. Rahmat-Samii, "Spectral FDTD: A novel technique for the analysis of oblique incident plane wave on periodic structures," IEEE Trans. Antennas Propag., vol. 54, no. 6, pp. 1818–1825, June 2006.

[4] C. A. Balanis, Modern Antenna Handbook, Chapter 12, Wiley, 2008.

Chapter 9

Reconfigurable Fragmented Aperture Arrays

[PLACEHOLDER: This chapter will cover reconfigurable fragmented aperture array antennas, including improved scan loss performance, dynamic polarization control, and related topics.]

Chapter 10

Recent Fragmented Aperture Innovations

10.1 Introduction

The preceding chapters have presented the fragmented aperture antenna concept from its origins through increasingly sophisticated applications: broadband single elements, improved pixel geometries, reconfigurable apertures, ultra-wideband arrays, and wide-scan phased arrays. Throughout this development, spanning more than two decades, the core idea has remained the same: partition a conducting surface into sub-wavelength pixels and use computational optimization to determine which pixels should be conducting and which should not.

In recent years, several research groups have extended the fragmented aperture concept in directions that were not anticipated when the original work began. This chapter surveys three such directions that represent significant advances in the field.

First, researchers at the Georgia Tech Research Institute (GTRI) have developed a fundamentally new way to parameterize the fragmented design space. Instead of optimizing a binary array of pixel states, they define a smooth, continuous *level set function* whose zero-crossings determine the metal boundaries. This *Periodic Level Set Function* (P-LSF) approach converts the combinatorial optimization problem into a continuous one, enabling the use of powerful gradient-free optimizers such as the covariance matrix adaptation evolution strategy (CMA-ES) and dramatically improving convergence.

Second, researchers at the University of Michigan have demonstrated a distributed fragmented antenna in which the individual radiating elements are carried by separate unmanned aerial vehicles (UAVs) in a swarm formation. Near-field electromagnetic coupling between the elements—through their inductive end loads—creates a larger effective aperture with significantly enhanced bandwidth, extending the fragmented aperture concept to mobile, multi-platform scenarios.

Third, emerging work on machine learning and artificial intelligence methods promises to dramatically accelerate the fragmented aperture design process by replacing or augmenting the computationally expensive full-wave simulations that currently dominate the design cycle.

This chapter is intended as a living document that will be updated as these and other innovations mature.

10.2 Level Set Methods for Fragmented Aperture Design

10.2.1 From Binary Pixels to Continuous Parameterization

All of the fragmented aperture designs presented in Chapters 2 through 9 use a binary parameterization: each pixel is assigned a state of 1 (conducting) or 0 (non-conducting), and the collection of pixel states forms the design vector that is optimized by a genetic algorithm. For an aperture with N independent pixels, the design space is the set of vertices of an N-dimensional unit hypercube, $\boldsymbol{\alpha} \in \{0,1\}^N$. This space is discrete, non-convex, and completely disjoint—no continuous path connects one design to another.

While genetic algorithms have been remarkably successful in navigating this difficult design space (see Chapters 2, 3, and 7), the binary parameterization imposes fundamental limitations. The mutation and crossover operators of a GA can only flip individual bits, and the resulting design changes are necessarily discontinuous. Moreover, the discrete design space precludes the use of many powerful continuous optimization algorithms that rely on interpolation, gradient information, or covariance estimation.

As the number of pixels grows, these limitations become increasingly severe. The improved mutation algorithm described in Chapter 3 addressed the convergence problem for moderately large pixel counts, but the underlying combinatorial nature of the binary design space remains a fundamental bottleneck.

An alternative approach is to define the material distribution not as a binary array but as a continuous function over the aperture, where the zero-crossings of the function determine the boundaries between conducting and non-conducting regions. This is the essence of the *level set method*, which has a rich history in structural topology optimization [1, 2] and has recently been applied to electromagnetic design problems including antennas and metasurfaces.

10.2.2 The Periodic Level Set Function

Saad-Falcon et al. [3] introduced the *Periodic Level Set Function* (P-LSF), a continuous parameterization specifically designed for periodic electromagnetic structures such as metasurfaces and phased array elements. The P-LSF can serve as a drop-in replacement for the traditional binary fragmented parameterization.

In the P-LSF approach, the material distribution over the unit cell is defined by a level set function $f(\mathbf{x})$ composed of a weighted sum of Gaussian radial basis functions (RBFs):

$$f_{\boldsymbol{\alpha}}(\mathbf{x}) = -T + \sum_{i=1}^{N} \alpha_i \, e^{-\gamma_i^2 \|\mathbf{x}-\mathbf{c}_i\|^2} \tag{10.1}$$

where $\mathbf{c}_i$ are the RBF centers (uniformly spaced across the unit cell), γ_i are scale factors, T is a threshold, and $\boldsymbol{\alpha} = [\alpha_1, \alpha_2, \ldots, \alpha_N]^T$ are the basis coefficients that serve as the design variables. The material distribution is then determined by rounding: metal is placed wherever $f(\mathbf{x}) > 0$, and air wherever $f(\mathbf{x}) \leq 0$. The design variables α_i are real-valued and bounded, $-1 \leq \alpha_i \leq 1$, so the design space is the interior of a continuous, convex hypercube $\boldsymbol{\alpha} \in [-1, 1]^N$.

The key innovation of the P-LSF is the use of *distance wrapping* to enforce periodicity. In a standard level set function, the RBF influence decays to zero at the boundaries of the unit cell, creating material discontinuities when the unit cell is tiled into a periodic array. The P-LSF replaces the Euclidean distance $\|\mathbf{x} - \mathbf{c}\|$ with a *wrapped distance* that accounts for periodicity:

$$\|\mathbf{x} - \mathbf{c}\|_{\text{wrapped}} = \sqrt{\sum_{d=1}^{D} \min_{n \in \mathbb{Z}} (x_d + n \cdot s_d - c_d)^2} \tag{10.2}$$

where s_d is the period in dimension d. This ensures that each RBF's influence wraps continuously around the unit cell boundaries, producing material distributions that are inherently periodic with no discontinuities at the cell edges.

The choice of norm in the distance computation affects the character of the resulting designs. Using the ℓ_2 (Euclidean) norm produces designs with rounded, organic-looking features—curves, circles, and smooth boundaries. Using the ℓ_∞ (Chebyshev) norm produces designs with more rectangular, Manhattan-like features that resemble traditional fragmented designs. The ℓ_1 norm produces intermediate, diamond-shaped features. This flexibility allows the designer to select a parameterization suited to the physics of the problem: broadband objectives tend to favor the smooth features of the ℓ_2 norm, while narrowband resonant structures may benefit from the sharper features of the ℓ_∞ norm.

10.2.3 Optimization and Results

The continuous P-LSF design space enables the use of optimization algorithms beyond genetic algorithms. Saad-Falcon et al. demonstrated significant improvements using the covariance matrix adaptation evolution strategy (CMA-ES) [4], a gradient-free optimizer that models the cost function with a multivariate Gaussian distribution and iteratively updates the covariance matrix to guide the search. CMA-ES has been shown to be highly effective for continuous, nonlinear optimization problems [5], and the P-LSF parameterization makes it directly applicable to fragmented aperture design.

The P-LSF and binary fragmented parameterizations were compared on two design objectives using FDTD electromagnetic simulation. The first was a broadband 2:1 bandpass frequency-selective surface (FSS) operating from 15 to 30 GHz (78% fractional bandwidth). The unit cell was discretized onto a 120×120 grid, with the binary parameterization using 4×4 pixel fragments (915 design variables) and the P-LSF using 32×32 RBFs (1024 continuous design variables). Both the non-dominated sorting genetic algorithm II (NSGA-II) [6] and CMA-ES were applied.

For the broadband bandpass objective, the P-LSF with multi-stage GA optimization converged more quickly and to a higher cost function value than the fragmented parameterization. The P-LSF design achieved better than −10 dB reflection across the 15–30 GHz passband. The optimized metasurface was fabricated on Rogers RO3003 substrate and measured in a free-space focused beam system, with close agreement between simulation and measurement.

The second design objective was a dual-band high-Q notch filter, with notch frequencies in the 8–16 GHz and 24–32 GHz bands. For this narrowband problem, the ℓ_∞ norm P-LSF outperformed the ℓ_2 norm, and CMA-ES substantially outperformed the genetic algorithm for both P-LSF variants. The best results were obtained with CMA-ES applied to the ℓ_2 norm P-LSF.

A multi-stage optimization procedure was also demonstrated, in which a coarse P-LSF basis is first optimized and then *upsampled* to a fine basis using a pseudo-inverse technique. This allows the optimizer to quickly converge on a coarse approximation and then refine it, reducing the total number of expensive electromagnetic simulations required.

[INSERT FIGURE: Side-by-side comparison of fragmented (binary) and P-LSF parameterizations, showing the binary pixel grid vs. the continuous level set function and resulting metal pattern. Adapted from Saad-Falcon et al. [3], Figure 1.]

[INSERT FIGURE: Convergence comparison for the broadband bandpass objective, showing P-LSF (GA and CMA-ES) vs. fragmented (GA) cost function histories. Adapted from Saad-Falcon et al. [3], Figure 5.]

[INSERT FIGURE: Fabricated 2:1 bandpass metasurface with measured vs. simulated S-parameters. Adapted from Saad-Falcon et al. [3], Figure 6.]

Howard et al. [7] subsequently applied the P-LSF methodology to the design of a wideband planar phased array element, demonstrating that the technique extends beyond metasurfaces to the phased array antenna designs that are the primary focus of this book. Howard also applied P-LSF-designed metasurfaces to dielectric materials characterization [8], designing a highly resonant periodic surface whose resonance magnitude depends linearly on the loss tangent of an adjacent dielectric sample. The open-source Meep FDTD solver [9] has been used to create a publicly available working example of the P-LSF optimization methodology.

10.2.4 Level Set Designs for Fragmented Aperture Antennas

[PLACEHOLDER: This section will present the author's own designs applying the P-LSF approach to the same antenna design problems presented in Chapter 3. Specifically, the skewed-lattice aperture designs operating in the 500 MHz to 2.0 GHz range (see Chapter 3, Section 5.1) will be redesigned using continuous level set parameterization, providing a direct, controlled comparison between the binary GA approach and the P-LSF/CMA-ES approach on identical antenna geometries. Key comparisons will include:

- **Convergence speed (number of function evaluations to reach a given performance level)**
- **Final design quality (realized gain, impedance match)**

Figure 10.1: Conceptual illustration of the distributed fragmented antenna on UAV platforms. Three miniaturized antennas are carried by separate UAVs in formation, with near-field coupling between their inductive end loads creating a larger effective radiating aperture [10].

- **Character of the optimized designs (smooth P-LSF features vs. rectilinear fragmented features)**
- **Effect of norm choice (ℓ_2 vs. ℓ_∞) on antenna performance**

This work is in progress.]

10.3 Distributed Fragmented Antennas on Mobile Platforms

10.3.1 Concept

At VHF and lower frequencies, the physical size of antennas becomes a significant challenge for mobile platforms. A conventional half-wave dipole at 240 MHz is approximately 62 cm long—too large for small robotic platforms such as unmanned aerial vehicles (UAVs) with maximum dimensions of 15–20 cm. Electrically small antennas that fit on such platforms suffer from narrow bandwidth and poor radiation efficiency, severely limiting data rate and communication range.

Barani, Harvey, and Sarabandi [10] proposed an elegant solution that applies the fragmented aperture philosophy to this problem: instead of placing a single large antenna on a single platform, distribute the antenna across a *formation* of platforms and exploit near-field electromagnetic coupling between the individual elements to synthesize a larger effective aperture. The concept is illustrated schematically in Figure 10.1.

[INSERT FIGURE: Conceptual illustration of three UAVs in linear formation, each carrying an inductively end-loaded folded dipole antenna, with coupling indicated between adjacent elements. Based on Barani et al. [10], Figure 1.]

The key insight is that a cluster of coupled antennas occupying a given volume has a lower radiation quality factor Q than any single antenna confined to a smaller subvolume, and can therefore radiate efficiently over a wider bandwidth. The fragmented antenna is "assembled" by flying the platforms into formation, and "disassembled" when they disperse.

10.3.2 Single Element Design

Each UAV carries a single miniaturized antenna: an inductively end-loaded folded dipole printed on Rogers RO4003C substrate ($\varepsilon_r = 3.55$, $\tan\delta = 0.0027$). The inductive end loads—wire loops at each end of the dipole arms—serve two purposes. First, they reduce the physical length of the antenna by increasing the electrical length per unit of physical length; the end-loaded antenna is confined to a volume of $12 \times 10 \times 10$ cm

($0.096\lambda_0 \times 0.08\lambda_0 \times 0.08\lambda_0$ at 240 MHz) with a total mass of 18 g including the matching network. Second, the end loads produce strong near-field magnetic and electric fields that extend over distances of 100–150 mm from the antenna, enabling coupling to adjacent elements in the formation.

When operating in isolation, the single miniaturized antenna provides a -10 dB return loss bandwidth of only 2.4 MHz ($\sim 1\%$) with a 25 Ω input impedance—typical of the severe bandwidth limitations of electrically small antennas.

Barani et al. also considered folded and threefold versions of the dipole element. An n-fold dipole has an input impedance approximately n^2 times that of a single dipole, which can be exploited to achieve better impedance matching in the coupled configuration. The threefold version also exhibits stronger near-field coupling over longer distances due to the larger end-loop diameters.

10.3.3 Coupling Mechanisms and Optimization

In the proposed three-element configuration, only the center antenna (the "driver") is excited; the two adjacent antennas (the "assistive" elements) are passively terminated with optimized lumped-element loads. Three coupling mechanisms operate between adjacent elements:

1. **Magnetic (inductive) coupling** between the end loops of adjacent antennas, via their normal magnetic fields. This is the dominant coupling mechanism.
2. **Electric (capacitive) coupling** between the dipole arms of adjacent antennas.
3. **Capacitive coupling between end loops and dipole arms** of adjacent antennas, arising from the strong normal electric field produced by the non-uniform current distribution on the loops.

The coupled signal from the driver is received by the assistive antennas, re-radiated, and also reflected back to the driver through the terminating loads. The assistive antennas thus augment the radiation of the driver, increasing both bandwidth and gain.

The terminating loads on the assistive antennas are optimized using a cost function that balances fractional bandwidth and average radiation efficiency:

$$C(\text{load}) = \alpha \frac{\Delta f}{f_0} + \beta\,\bar{\eta} \tag{10.3}$$

where $\Delta f/f_0$ is the fractional bandwidth, $\bar{\eta}$ is the average radiation efficiency over the -10 dB bandwidth, and α and β are weighting constants. The optimization showed that purely reactive loads (capacitive or inductive) provide the best tradeoff: they enhance bandwidth without dissipating power and maintain high radiation efficiency. The optimal load for a separation distance of $d = 12$ cm was found to be a series capacitor of $C = 4.4$ pF.

The capacitive load introduces a second resonance at a frequency shifted above the driver's natural resonance. The enhanced bandwidth of the coupled configuration results from the merging of the driver and assistive antenna resonances—the same principle of coupled resonators that underlies the bandwidth enhancement in many filter and antenna designs.

10.3.4 Sensitivity and Platform Effects

A practical concern for a formation-based antenna is the sensitivity of performance to variations in inter-element spacing and alignment. Barani et al. investigated these effects through full-wave simulation.

Separation distance: As the inter-element distance d increases from 12 to 16 cm (one to 1.33 element lengths), the bandwidth decreases from 18.4 to 13.5 MHz due to weaker coupling, while the input impedance decreases from 126 Ω to 100 Ω. Radiation efficiency remained above 97% (simulated) for all distances.

Lateral misalignment: Shifting the assistive antennas by up to 4 cm in the lateral direction produced modest bandwidth degradation. The relatively wide near-field profiles of the end loads maintain coupling over a broad spatial region, making the configuration tolerant of typical UAV flight formation errors.

Platform effects: Placing the antenna on a small dielectric UAV body ($\varepsilon_r = 4$, 20 cm $\times$ 20 cm) caused only a small shift in center frequency, because the platform is much smaller than the operating wavelength ($\sim \lambda/6$) and occupies a small fractional volume around the radiating element. For metallic platforms, however, the platform and antenna would need to be co-designed to account for electromagnetic interactions.

Tunable matching circuit: To accommodate the impedance variations caused by changing formation geometry, a tunable matching network was designed using a varactor diode. The L-section matching circuit consists of a fixed inductor ($L = 68$ nH), a fixed capacitor ($C_1 = 1.5$ nF), a varactor (C_2, controlled by a DC bias voltage V_B), and a 1:1 Balun transformer. This circuit can dynamically match the antenna impedance as the formation distance varies, enabling the driver antenna to also operate independently when the assistive elements are absent.

10.3.5 Fabrication and Measurement Results

The three-element coupled antenna array was fabricated and measured in the anechoic chamber at the University of Michigan. Key measured results include:

- **Bandwidth:** For $d = 12$ cm, the measured -10 dB bandwidth was 18.4 MHz (7.7% fractional bandwidth), compared to 2.4 MHz (1%) for the isolated single element—a 7.7-fold improvement.

- **Radiation efficiency:** Measured radiation efficiencies of 86.4%, 88.2%, and 80.4% for $d = 12$, 14, and 16 cm, respectively. The reduction from the simulated 97% was attributed to Balun transformer insertion loss ($\sim$0.7 dB).

- **Peak gain:** Approximately 1 dB higher than the isolated single element across the bandwidth.

- **Radiation pattern:** Patterns characteristic of a dipole antenna with somewhat higher directivity due to the larger effective aperture.

[INSERT FIGURE: Measured and simulated return loss for three separation distances ($d = 12$, 14, 16 cm) compared to the isolated single antenna. Based on Barani et al. [10], Figures 10 and 17.]

[INSERT FIGURE: Photograph of fabricated antennas in the anechoic chamber. Based on Barani et al. [10], Figure 16.]

The close agreement between simulation and measurement validates the design approach and confirms that the fragmented antenna concept can be successfully extended to multi-platform, formation-based configurations.

10.4 Machine Learning and AI-Accelerated Design

[PLACEHOLDER: This section will present the author's ongoing work on machine learning and artificial intelligence methods for accelerating the fragmented aperture antenna design process. The computational bottleneck in fragmented aperture design has always been the full-wave electromagnetic simulation (FDTD or equivalent) required to evaluate each candidate design. For the designs presented in earlier chapters, each GA generation requires running hundreds to thousands of FDTD simulations, and the total design cycle can consume days to weeks of computation time even on modern parallel computing resources.

Several promising approaches are being explored:

- **Surrogate-based optimization:** Training a machine learning model (neural network, Gaussian process, etc.) to approximate the mapping from pixel configuration to antenna performance, then using this fast surrogate in place of FDTD during the optimization loop.
- **Generative design:** Using generative models (variational autoencoders, generative adversarial networks, diffusion models) to learn the distribution of high-performing designs and directly generate candidate solutions.
- **Transfer learning:** Leveraging knowledge from previously optimized designs at one frequency or geometry to accelerate optimization at a different frequency or geometry.

The broader field of AI-assisted antenna design is surveyed in [11]. This section will be expanded as results become available.]

10.5 Summary

The fragmented aperture antenna concept, first introduced more than 25 years ago, continues to inspire innovation in the antenna community. This chapter has surveyed three active areas of development.

The Periodic Level Set Function (P-LSF) introduced by Saad-Falcon et al. [3] provides a mathematically elegant reformulation of the fragmented design space. By replacing the binary pixel states with a continuous, smooth function whose zero-crossings define the metal boundaries, the P-LSF converts the combinatorial optimization problem into a continuous one. This enables the use of powerful optimizers such as CMA-ES and accelerates convergence, while also producing designs with richer geometric features—smooth curves and arbitrary boundary shapes—that are not achievable with rectangular pixels.

The distributed fragmented antenna of Barani et al. [10] extends the fragmented aperture concept to mobile, multi-platform scenarios. By distributing miniaturized radiating elements across a formation of UAVs and exploiting near-field electromagnetic coupling, this approach achieves bandwidth and gain improvements that would be impossible with any single antenna small enough to fit on a UAV platform. The measured 7.7-fold bandwidth improvement demonstrates the practical potential of this approach for VHF communications in swarm robotics applications.

Machine learning and AI methods, currently under active development, promise to address the computational bottleneck that has been the primary limitation of the fragmented aperture design methodology since its inception.

These three innovations are largely complementary. One can envision, for example, using ML-accelerated optimization with a P-LSF parameterization to design the individual elements of a distributed coupled antenna system. As these and other advances mature, the fragmented aperture concept will continue to expand in capability and find new applications.

References

[1] D. Guirguis and M. F. Aly, “A derivative-free level-set method for topology optimization,” *Finite Elements in Analysis and Design*, vol. 120, pp. 41–56, 2016.

[2] D. Guirguis, D. Melek, W. W. Aly, and M. F. Aly, “High-resolution non-gradient topology optimization,” *Journal of Computational Physics*, vol. 372, pp. 107–125, 2018.

[3] A. Saad-Falcon, C. Howard, J. Romberg, and K. Allen, “Level set methods for gradient-free optimization of metasurface arrays,” *Scientific Reports*, vol. 14, p. 16674, Jul. 2024, arXiv preprint: 2307.07606.

[4] N. Hansen, S. D. Müller, and P. Koumoutsakos, “Reducing the time complexity of the derandomized evolution strategy with covariance matrix adaptation (CMA-ES),” *Evolutionary Computation*, vol. 11, no. 1, pp. 1–18, 2003.

[5] M. D. Gregory, Z. Bayraktar, and D. H. Werner, “Fast optimization of electromagnetic design problems using the covariance matrix adaptation evolutionary strategy,” *IEEE Transactions on Antennas and Propagation*, vol. 59, no. 4, pp. 1275–1285, 2011.

[6] K. Deb, A. Pratap, S. Agarwal, and T. Meyarivan, “A fast and elitist multiobjective genetic algorithm: NSGA-II,” *IEEE Transactions on Evolutionary Computation*, vol. 6, no. 2, pp. 182–197, 2002.

[7] C. T. Howard, A. Saad-Falcon, D. W. Landgren, and K. W. Allen, “Topology optimization of a wideband planar phased array element using periodic level set functions,” in *2024 IEEE International Symposium on Phased Array Systems and Technology (ARRAY)*, 2024, pp. 1–7.

[8] C. Howard *et al.*, “A loss tangent measurement surface for free space focused beam characterization of low-loss dielectrics,” in *2022 IEEE International Symposium on Phased Array Systems and Technology (PAST)*, 2022, pp. 1–6.

[9] A. F. Oskooi, D. Roundy, M. Ibanescu, P. Bermel, J. D. Joannopoulos, and S. G. Johnson, “MEEP: A flexible free-software package for electromagnetic simulations by the FDTD method,” *Computer Physics Communications*, vol. 181, no. 3, pp. 687–702, 2010.

[10] N. Barani, J. F. Harvey, and K. Sarabandi, “Fragmented antenna realization using coupled small radiating elements,” *IEEE Transactions on Antennas and Propagation*, vol. 66, no. 4, pp. 1725–1735, 2018.

[11] N. Sarker, P. Podder *et al.*, “Applications of machine learning and deep learning in antenna design, optimization and selection: A review,” *IEEE Access*, vol. 11, pp. 103 890–103 915, 2023.

Appendix A

Computational Modeling of Antennas

A.1 Acknowledgement

The author would like to personally thank Professor Glenn Smith, Georgia Tech Regents Professor Emeritus, for his tremendous help in compiling this appendix on the computational modeling of antennas. Much of this material was published in the Balanis Antenna Engineering Handbook [41] and earlier in the Taflove book on computational electrodynamics [7].

A.2 Introduction

The finite-difference time-domain (FDTD) method is a computational procedure for solving Maxwell's equations that is based on a clever algorithm first proposed by Kane S. Yee in 1966 [1]. When Yee proposed his algorithm, the method was computationally intensive in terms of both storage and run time, and only problems of very modest size could be solved using the best computational facilities (mainframe computers). Since then the power of computers has steadily increased, as has the popularity of the FDTD method. The first comprehensive analyses of practical antennas using the method were performed during the early 1990s, and today such computations are routinely performed on personal computers [2]–[6].

The purpose of this appendix is to introduce the reader to the fundamentals of the FDTD method as applied to practical antennas. After studying this material, the reader should understand both the power and the limitations of the method and be in a position to decide whether the FDTD method is suitable for analyzing a particular antenna problem. Because of the limited space, we cannot provide the details for implementing the method in a computer program. Readers interested in writing their own program are referred to [7] for the details; others may wish to use one of the commercially available FDTD computer codes.

A.3 The Basic FDTD Algorithm

In the Yee algorithm, both space and time are discretized, with the increments in space for rectangular coordinates being Δx, Δy, Δz and the increment in time being Δt [8], [9]. Figure A.1 is a schematic drawing showing a typical volume in which Maxwell's equations are to be solved. The volume is divided into unit cells, and the electromagnetic constitutive parameters ($\epsilon = \epsilon_r \epsilon_o$, $\mu = \mu_r \mu_o$, σ) can vary from cell to cell to define different objects within the volume.[1] The six components of the electromagnetic field $(E_x, E_y, E_z; H_x, H_y, H_z)$ are distributed over a unit cell (Yee cell) as shown in the inset of Figure A.1. Notice that all of the components are located at different points within the cell, and the components of H are displaced from those of E by one half of a spatial increment, e.g., $\Delta x/2$. Although not shown in the figure, the components of H are also evaluated at points displaced by one half of a time increment, $\Delta t/2$, from those of E.

The partial derivatives in Maxwell's equations are approximated by ratios of differences, for example,

$$\frac{\partial E_x}{\partial z} \approx \frac{\Delta E_x}{\Delta z}, \quad \frac{\partial H_y}{\partial t} \approx \frac{\Delta H_y}{\Delta t} \tag{A.1}$$

For the spatial derivatives, the increment in the numerator is formed by differencing corresponding field components from adjacent unit cells, and for the temporal derivatives, it is formed by differencing field components from two adjacent time steps, e.g., t and $t+\Delta t$. The discretized Maxwell's equations are arranged to form two sets of difference equations known collectively as "update equations." The first set, which we will call A, determines the change in the magnetic field, $H(t+\Delta t/2) - H(t-\Delta t/2)$, from the electric field at an intermediate time step, $E(t)$. The second set, which we will call B, determines the change in the electric field, $E(t+\Delta t) - E(t)$, from the magnetic field at an intermediate time step, $H(t+\Delta t/2)$.

At the start of the computation, we have the initial conditions: throughout the computational volume, the electric field is known at time $t = 0$, and the magnetic field is known at the earlier time $t = -\Delta t/2$. The update equations A are then used with the initial conditions to obtain the magnetic field at time $t = \Delta t/2$. Next, the update equations B are used with the magnetic field just obtained and the electric field at time $t = 0$ to obtain the electric field at time $t = \Delta t$. This procedure of alternately applying update equations A and B to advance the solution in time is known as "marching-in-time" or "stepping-in-time." It is repeated until the electromagnetic field is known throughout the computational volume at the desired time $t = t_{\text{max}} = N_t \Delta t$.

The choice for the increments of space and time (Δx, Δy, Δz, and Δt) is critical to the success of the algorithm, because their size determines how well the solution to the difference equations approximates the solution to Maxwell's equations. The spatial and temporal increments cannot be chosen independently; for convergence (as $\Delta x \to 0$, $\Delta t \to 0$, etc.) and stability of the algorithm, the increments must satisfy the Courant-Friedrichs-Lewy condition, which for free space is

[1] Here we mention only simple materials with constant permittivity, permeability, and electrical conductivity. In the FDTD method there are techniques to handle more complicated materials, such as those with dispersive and anisotropic properties [9].

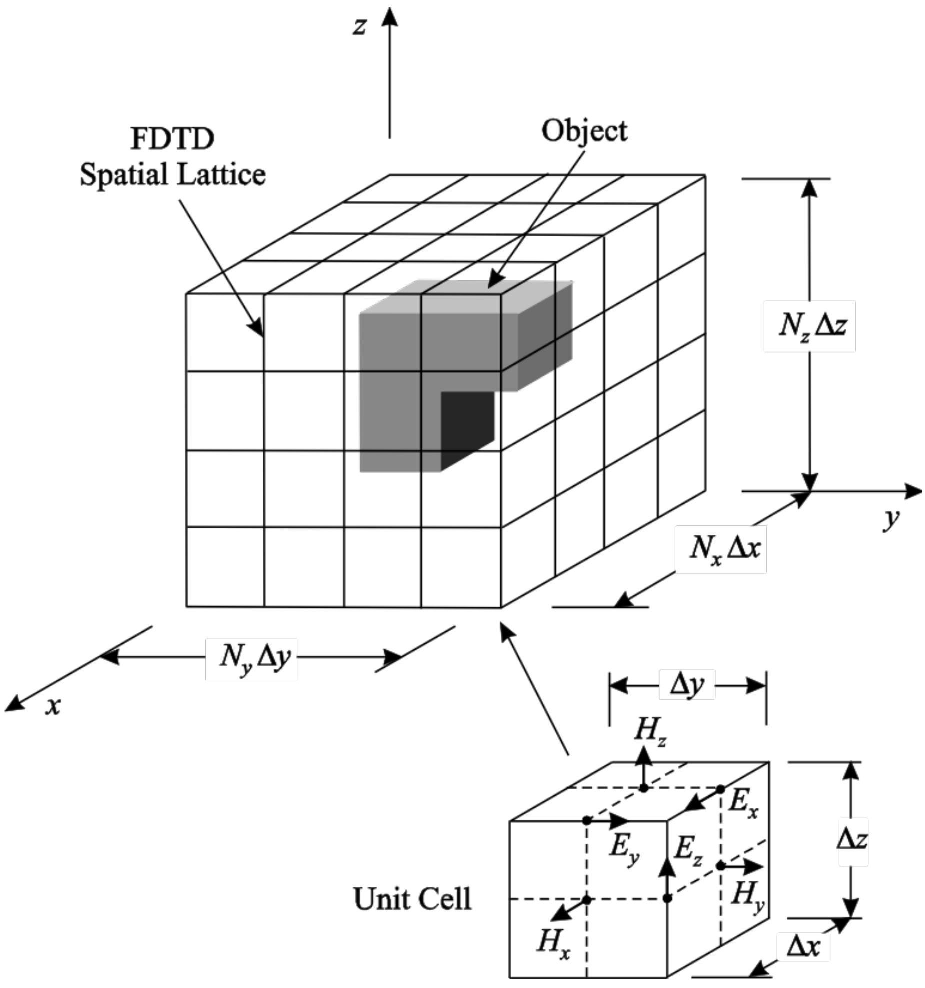

Figure A.1: Schematic drawing showing the computational volume, FDTD spatial lattice, and unit cell.

$$c\Delta t\sqrt{\frac{1}{\Delta x^2}+\frac{1}{\Delta y^2}+\frac{1}{\Delta z^2}} \leq 1. \tag{A.2}$$

For cubical cells, $\Delta x = \Delta y = \Delta z$, Equation (A.2) becomes $S = c\Delta t/\Delta x \leq \sqrt{1/3}$, where S is referred to as the "Courant number," and a reasonable choice is $S = 1/2$.

Additional restrictions on the spatial and temporal increments can only be obtained from knowledge of the variation of the field (the solution) in space and time. We must make Δz and Δt in Equation (A.1) small enough that the errors incurred by replacing the derivatives by the ratios of differences are acceptable. One obvious requirement is that the size of the spatial cells must be small enough to resolve all of the important structural features and the local field surrounding these features. Another requirement is that the error introduced by a phenomenon known as "numerical dispersion" must be negligible.

When there is numerical dispersion, a pulse that starts out with one shape ends up with a different shape after propagating through the FDTD lattice. Numerical dispersion is caused by the different frequency components of the pulse propagating through the lattice with different phase velocities. It can be quantified by considering a time-harmonic plane wave of angular frequency ω propagating in free space along one of the axes of the FDTD lattice, say the x axis. Assuming cubical cells, the numerical phase velocity, $\bar{v}_p$, for the wave, normalized to the speed of light in free space c, is

$$\frac{\bar{v}_p}{c} = \pi\left\{N_\lambda \sin^{-1}\left[\frac{1}{S}\sin\left(\frac{\pi S}{N_\lambda}\right)\right]\right\}^{-1}, \tag{A.3}$$

in which $N_\lambda = \lambda/\Delta x$ is the number of cells per wavelength [10]. Figure A.2 is a graph of this equation showing the relative error in the phase velocity in percent (solid line) and a related quantity, the error in the phase per cell in degrees (dashed line). Notice that the phase velocity is less than the speed of light, and that the error decreases monotonically with an increase in N_λ. For large N_λ (say $N_\lambda > 10$), the error in the phase velocity is approximately $(\pi^2/6)(1-S^2)/N_\lambda^2$, so halving the cell size reduces the error by a factor of four. In theory, any desired accuracy can be obtained by increasing N_λ.

Ideally, given an electromagnetics problem, we would like to estimate accurately the computational resources (computer memory and execution time) required to solve the problem using the FDTD method. This estimate is highly dependent on the problem and the computer being used. In practice, the estimate is usually made by comparing the requirements for the problem under consideration with those of a "benchmark problem" that has been run using a particular FDTD code on a particular computer. Even though the specific requirements are computer dependent, general rules for the scaling of the required memory and execution time with cell size are easily obtained.

Consider a computational volume that is a cube composed of cubical FDTD cells; then the total number of cells is $N = N_x^3$. Because only the most recent values of the electric and magnetic fields are needed at each step of the algorithm, the total storage required scales as N or N_x^3, i.e., as the third power of the number of cells along the edge of the cubical volume. The simulation must be run for a time roughly proportional to that required for light to cross the volume, $t_{\text{max}} \propto N_x\Delta x/c$. Thus, the number of time

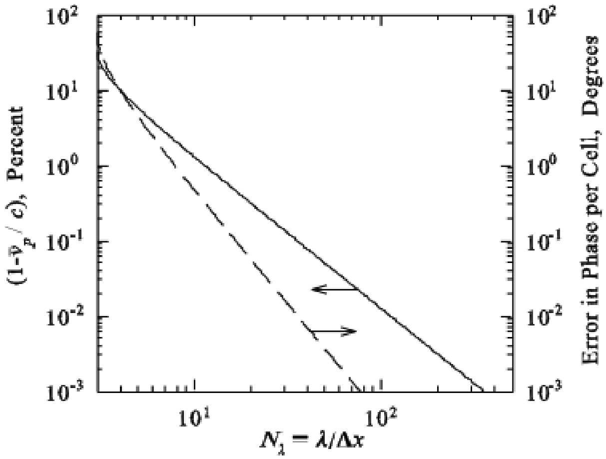

Figure A.2: Numerical dispersion as a function of the number of cells per wavelength, N_λ, for a time-harmonic plane wave propagating along one of the axes of an FDTD lattice of cubical cells. Solid line: the relative error in the phase velocity in percent. Dashed line: the error in the phase per cell in degrees. $S = 0.5$.

steps required is $N_t = t_{\text{max}}/\Delta t \propto N_x/S \propto N_x$. The execution time is proportional to the product of the number of cells with the number of times the cells must be updated: $N \times N_t \propto N_x^4$. The execution time therefore scales as the fourth power of the number of cells along the edge of the cubical volume. If we halve the dimensions of the cells, the storage will increase by a factor of 8, and the execution time will increase by a factor of 16.

A.4 Formulation of the Antenna Problem in the FDTD Method

Antennas are customarily used in two states: transmission and reception. While the two states are related through the reciprocity inherent in Maxwell's equations, not all quantities for one state can be obtained from the other. Thus, we must have two separate FDTD formulations for the antenna problem: one for the transmitting antenna and the other for the receiving antenna.

A.4.1 Transmitting Antenna

Figure A.3(a) is a schematic drawing showing the basic elements involved in the FDTD analysis of a transmitting antenna. The figure is for a cross section through the computational volume, and the antenna is located near the center of the volume. The arrangement used to excite the antenna is shown in Figure A.4(a). The antenna is connected to the source by a transmission line (waveguide) of characteristic impedance R_o, and the source is matched to the characteristic impedance (there is no reflection for a wave entering the source).[2] The specified excitation is the outward-propagating (incident) voltage wave $V_t^+(t)$ for a single mode at the reference plane in the line. At this reference plane there is also a voltage $V_t^-(t)$ associated with an inward-propagating (reflected) wave.

The finite computational volume in Figure A.3(a) is surrounded by an absorbing boundary. The objective for this boundary is to reproduce at its interior surface the same conditions for the electromagnetic field that would exist if the volume were infinite. Stated differently, if we consider the electromagnetic field within the volume to be composed of a spectrum of plane waves, both outward propagating and evanescent, all of these waves should be absorbed without reflection by the boundary. The most effective absorbing boundaries in use today are the perfectly matched layers (PMLs). Their implementation is discussed in the literature [11], [12].

The FDTD method provides the electromagnetic field for all lattice points within the finite computational volume. However, for many antenna applications, we need the radiated or far-zone field, which is the field in the limit as the radial distance from the antenna becomes infinite ($r \to \infty$). This field can be obtained by applying a near-field to far-field (NFFF) transformation. For this transformation, a closed surface S is placed around the antenna and inside the absorbing boundary, as shown by the dashed line in Figure A.3. The field (E^t and H^t) on this surface is obtained for the time period of interest and used to calculate the following electric and magnetic surface current densities:

$$J_s(r', t) = \hat{n} \times H^t(r', t), \tag{A.4}$$

$$M_s(r', t) = -\hat{n} \times E^t(r', t). \tag{A.5}$$

Here, as shown in Figure A.3(b), r' locates a point on the surface, and $\hat{n}$ is the outward-pointing unit vector normal to the surface at that point. Outside the surface S, these currents produce the same electromagnetic field as the transmitting antenna (E^t, H^t), and inside the surface they produce a null field ($E = 0$, $H = 0$).

At the position r, the radiated or far-zone field (indicated by the additional superscript r) is obtained using these currents with a version of Huygens' principle for electromagnetic fields [8]:

$$E^{tr}(r, t) = \frac{\mu_o}{4\pi r} \iint_S \left\{ \hat{r} \times \hat{r} \times \frac{\partial}{\partial t'} \left[J_s(r', t') \right] + \frac{1}{\eta_o} \hat{r} \times \frac{\partial}{\partial t'} \left[M_s(r', t') \right] \right\}_{t'=t_r} dS', \tag{A.6}$$

$$H^{tr}(r, t) = \frac{1}{\eta_o} \hat{r} \times E^{tr}(r, t), \tag{A.7}$$

in which the retarded time is

[2]Throughout this appendix we will assume that the characteristic impedance of a transmission line is real, a resistance.

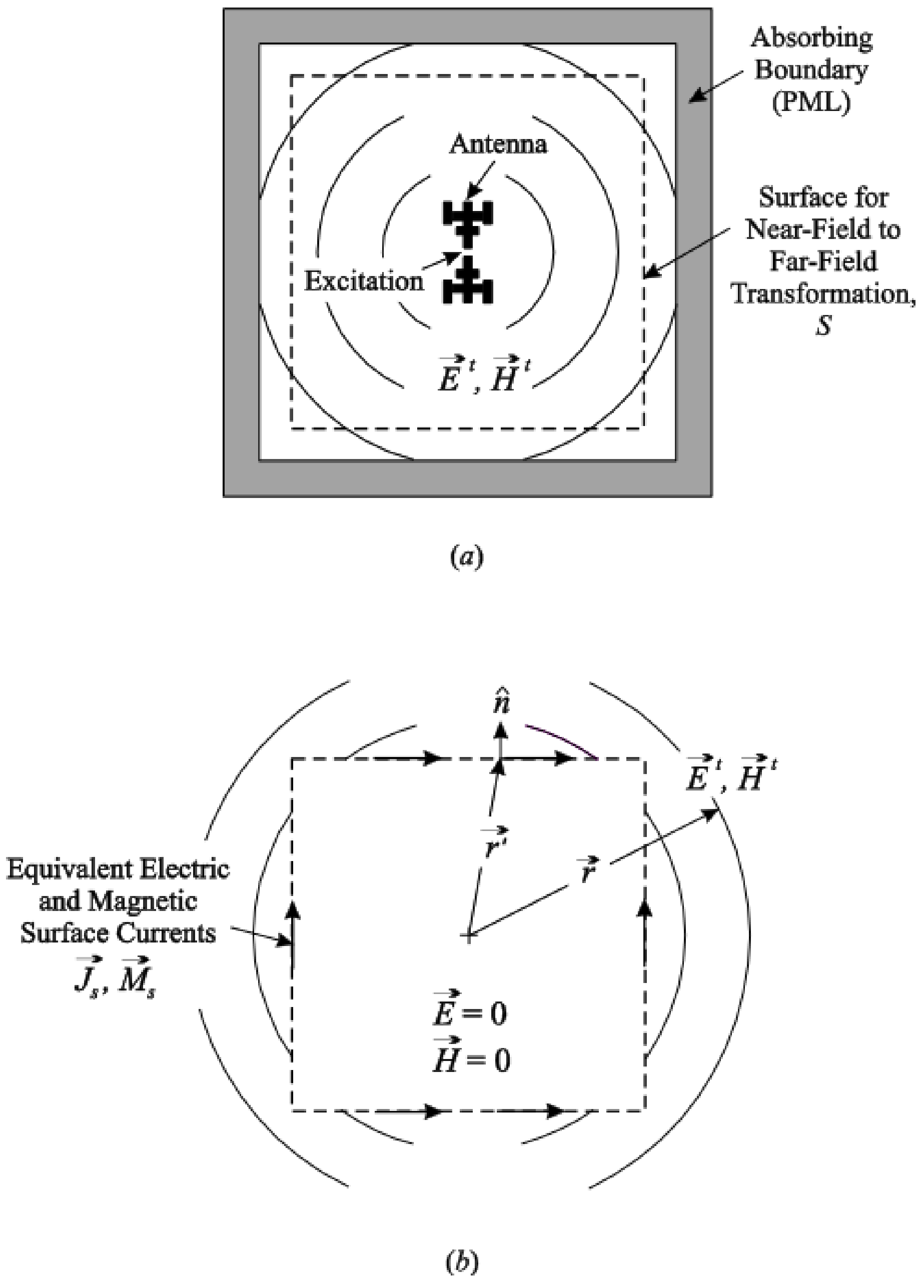

Figure A.3: (a) Schematic drawing showing the basic elements involved in the FDTD analysis of a transmitting antenna. (b) Details for the near-field to far-field transformation.

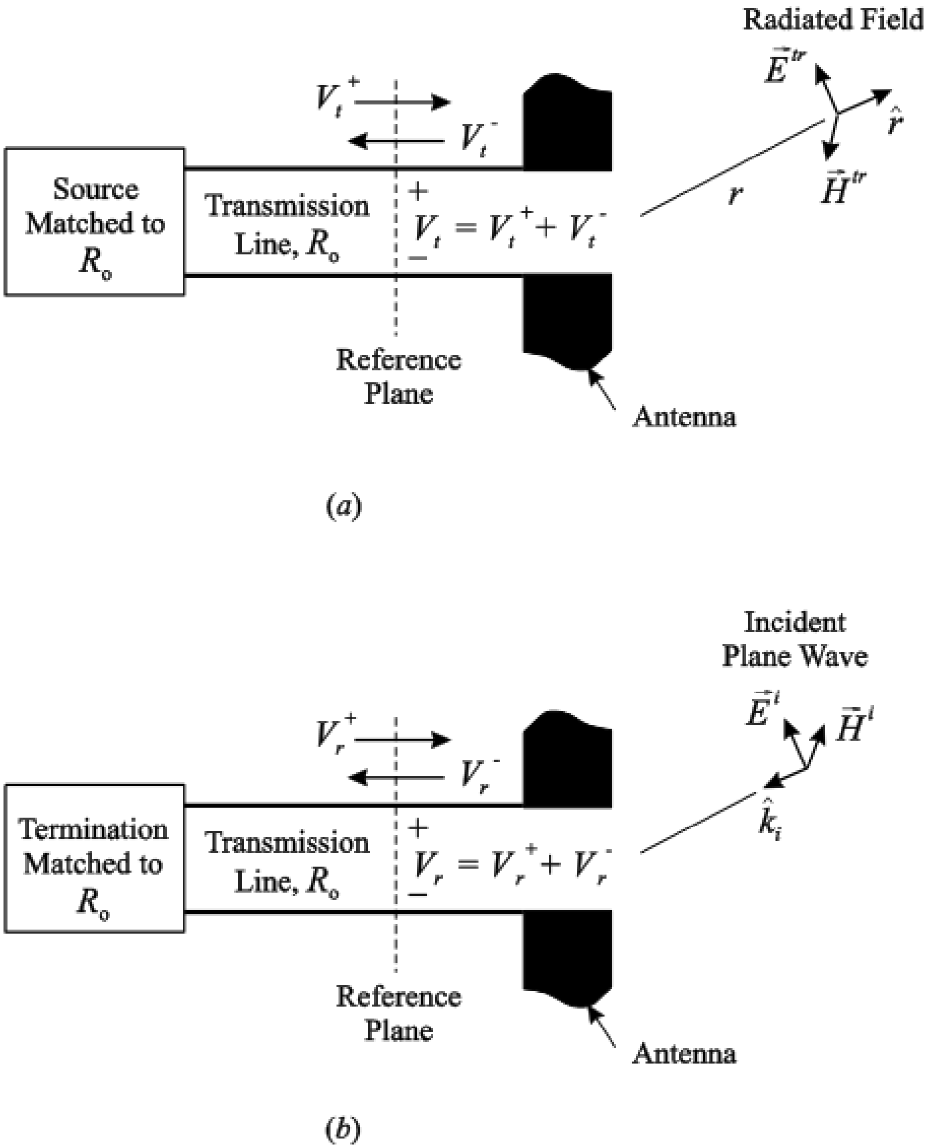

Figure A.4: The details for the feed region of (a) the transmitting antenna and (b) the receiving antenna. The characteristic impedance of the transmission line is R_o, and the source and termination are matched to this impedance.

$$t_r = t - (r - \hat{r} \cdot \vec{r}\,')/c \tag{A.8}$$

and $\eta_o = \sqrt{\mu_o/\epsilon_o}$ is the wave impedance of free space.

In some situations, we may require the near field at points that are so far from the antenna that it is impractical to extend the computational volume to include them. In such cases, a near-field to near-field (NFNF) transformation can be used: the FDTD analysis is performed for a volume such as that shown in Figure A.3(a), and the field on the surface of the volume is transformed to obtain the near field outside the volume. Details for the NFNF transformation can be found in [13], [14].

A.4.2 Receiving Antenna

Figure A.5(a) is a schematic drawing showing the basic elements involved in the FDTD analysis of a receiving antenna. As for the transmitting antenna, the figure is for a cross section through the computational volume, and the finite computational volume is surrounded by an absorbing boundary. The excitation for the antenna is an incident, transverse electromagnetic (TEM) plane wave propagating in the direction $\hat{k}_i$ with the field

$$E^i(r,t), \quad H^i(r,t) = \frac{1}{\eta_o}\hat{k}_i \times E^i(r,t). \tag{A.9}$$

Here, the vector E^i is transverse to $\hat{k}_i$, viz, $\hat{k}_i \cdot E^i = 0$.

The closed surface S with outward-pointing unit normal vector $\hat{n}$ is placed around the antenna and inside the absorbing boundary. As shown in Figure A.5(b), the following electric and magnetic surface current densities are placed on this surface to produce the incident field (E^i, H^i) inside the surface and a null field ($E = 0$, $H = 0$) outside the surface:

$$J_s(r,t) = -\hat{n} \times H^i(r,t), \quad M_s(r,t) = \hat{n} \times E^i(r,t). \tag{A.10}$$

For the receiving antenna, we generally want to know the voltage produced in the antenna by the incident wave. The arrangement used to accomplish this is shown in Figure A.4(b). The antenna is connected to the termination by a transmission line (waveguide) of characteristic impedance R_o, and the termination is matched to the characteristic impedance (there is no reflection for a wave entering the termination). The desired response is the inward-propagating voltage wave $V_r^-(t)$ for a single mode at the reference plane in this line.

The scattered field is the field produced by the currents induced in the antenna by the incident field. Notice from Figure A.5(a) that the field inside the surface S is the total field, i.e., the sum of the incident and scattered fields ($E^r = E^i + E^s$, $H^r = H^i + H^s$). However, the field outside the surface, in the region between the surface and the absorbing boundary, is only the scattered field (E^s, H^s). If we are interested in the scattering properties of the antenna, we can obtain them from knowledge of the field in this region. For example, the far-zone scattered field can be determined using a near-field to far-field transformation, as in the case for the transmitting antenna. The surface for the transformation must be placed between the surface for the plane-wave source and the absorbing boundary.

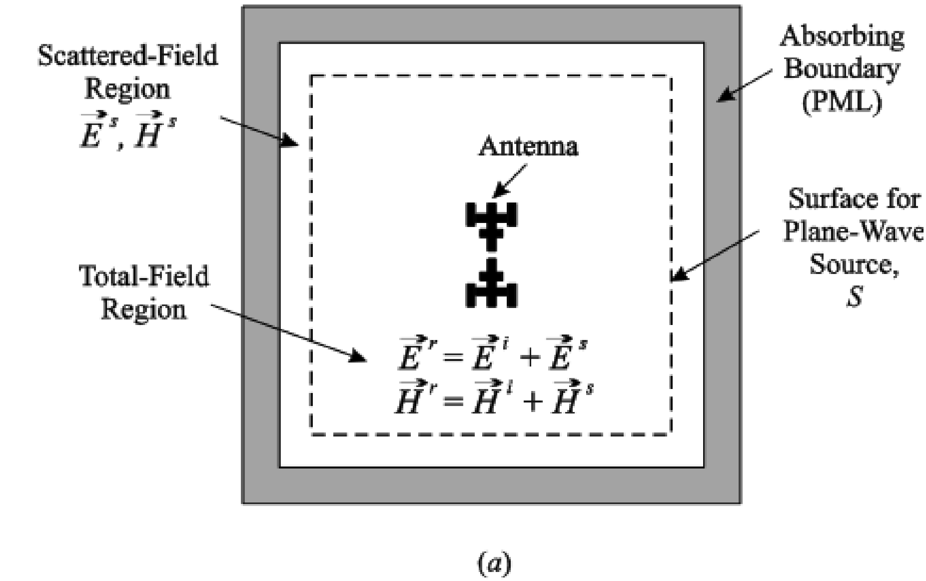

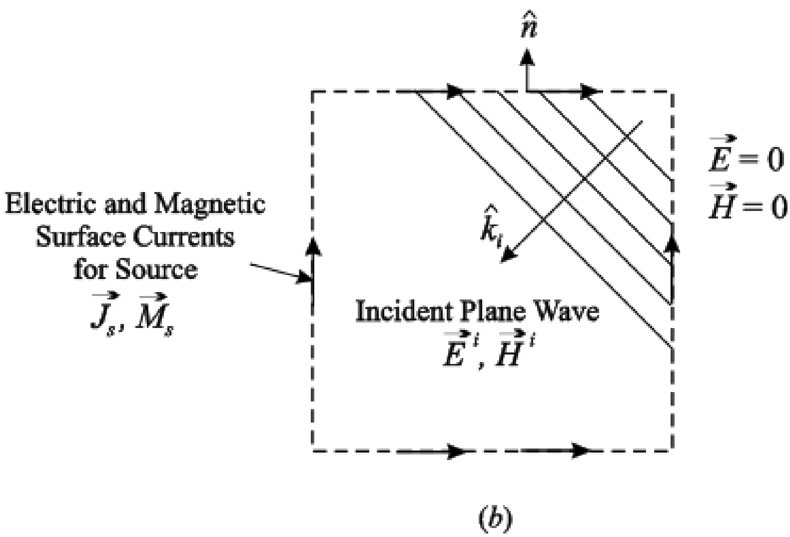

Figure A.5: (a) Schematic drawing showing the basic elements involved in the FDTD analysis of a receiving antenna. (b) Details for the plane-wave source.

A.4.3 Reciprocity

As mentioned earlier, some quantities for the states of transmission and reception are related through reciprocity. For example, when the arrangements shown in Figure A.4 are used for the source and termination, the following relationship applies [15]:

$$V_t^+(t) * V_r^-(t) = \frac{2\pi R_o}{\eta_o}\left[c\int\limits_{t'=-\infty}^{t} E^i(0,t')dt'\right] \cdot * \left[rE^{tr}(-r\hat{k}_i, t+r/c)\right], \quad \text{(A.11)}$$

in which $*$ indicates time convolution, and $\cdot *$ indicates the scalar product with time convolution. Here, the origin for the spherical coordinate system is centered on the antenna, as in Figure A.4(a), and the incident electric field E^i is evaluated at the origin ($r = 0$) of this system. The radiated electric field E^{tr} is evaluated at the radial distance r in the direction $(-\hat{k}_i)$ from which the incident field arrives and at the time $t + r/c$. This relationship can sometimes be used to eliminate the need for analyzing one of the two states (transmission or reception) when the other is known, or it can be used for verifying results from one state with results from the other.

A.4.4 Frequency Domain

The FDTD method is inherently a time-domain technique. When quantities are needed in the frequency domain (angular frequency ω), they are obtained using the discrete Fourier transformation, which is indicated by $V(t) \leftrightarrow V(\omega)$. The quantities customarily used for evaluating the performance of an antenna in the frequency domain are determined from the transformed variables. For the transmitting antenna, the voltage reflection coefficient Γ_A and input impedance Z_A are

$$\Gamma_A(\omega) = \frac{V_t^-(\omega)}{V_t^+(\omega)}, \quad \text{(A.12)}$$

$$Z_A(\omega) = R_o\left[\frac{1+\Gamma_A(\omega)}{1-\Gamma_A(\omega)}\right], \quad \text{(A.13)}$$

and the realized gain G_{Rel} (gain including mismatch) and gain G in the direction $\hat{r}$ are

$$G_{\text{Rel}}(\hat{r},\omega) = \frac{4\pi r^2 \hat{r}\cdot \text{Re}[S_c^{tr}(r,\omega)]}{\text{Power available from source}} = \frac{4\pi R_o r^2 |E^{tr}(r,\omega)|^2}{\eta_o |V_t^+(\omega)|^2}, \quad \text{(A.14)}$$

$$G(\hat{r},\omega) = \frac{4\pi r^2 \hat{r}\cdot \text{Re}[S_c^{tr}(r,\omega)]}{\text{Power accepted by antenna}} = \frac{1}{1-|\Gamma_A(\omega)|^2} G_{\text{Rel}}(\hat{r},\omega), \quad \text{(A.15)}$$

in which S_c is the complex Poynting vector.

For the receiving antenna, the realized effective area $A_{\text{Rel}}(\hat{k}_i,\omega)$ and the effective area $A_e(\hat{k}_i,\omega)$ for an incident plane wave propagating in the direction $\hat{k}_i$ are

$$A_{\text{Rel}}(\hat{k}_i,\omega) = \frac{\text{Power accepted by termination}}{\hat{k}_i \cdot \text{Re}[S_c^i(r,\omega)]} = \frac{\eta_o}{R_o}\frac{|V_r^-(\omega)|^2}{|E^i(\omega)|^2}, \tag{A.16}$$

and

$$A_e(\hat{k}_i,\omega) = \frac{\text{Power available from antenna}}{\hat{k}_i \cdot \text{Re}[S_c^i(r,\omega)]} = \frac{1}{1-|\Gamma_A(\omega)|^2} A_{\text{Rel}}(\hat{k}_i,\omega). \tag{A.17}$$

The gain and the effective area are related through reciprocity (Equation A.11); for a polarization match we have[3]

$$G(\hat{r},\omega) = \frac{4\pi}{\lambda^2} A_e(-\hat{r},\omega). \tag{A.18}$$

A.4.5 Input Signals

When we are interested in the performance of an antenna over a band of frequencies, a pulsed input signal is useful, followed by the Fourier transform to obtain the desired frequency-domain response. A natural choice for the pulse shape is the Gaussian pulse shown as a solid line in Figure A.6(a),

$$\begin{aligned} f(t) &= \exp\left[-(t/\tau_p)^2/2\right], \\ F(\omega) &= \sqrt{2\pi}\,\tau_p \exp\left[-(\omega\tau_p)^2/2\right], \end{aligned} \tag{A.19}$$

in which τ_p is the characteristic time. However, the spectrum for the Gaussian pulse contains significant low-frequency content (including dc), and this usually is not radiated by the antenna (the dc component never is). Thus, the field near the antenna may take an unacceptably long time to settle when a Gaussian pulse is used.

A better choice is the differentiated Gaussian pulse shown as a dashed line in Figure A.6(a),

$$\begin{aligned} f(t) &= -\left(\frac{t}{\tau_p}\right) \exp\left\{-\left[(t/\tau_p)^2 - 1\right]/2\right\}, \\ F(\omega) &= j\sqrt{2\pi}\,\omega\tau_p^2 \exp\left\{-\left[(\omega\tau_p)^2 - 1\right]/2\right\}, \end{aligned} \tag{A.20}$$

or the sinusoid of frequency ω_o amplitude modulated by a Gaussian pulse shown in Figure A.6(b),

$$\begin{aligned} f(t) &= \exp\left[-(t/\tau_p)^2/2\right]\sin(\omega_o t), \\ F(\omega) &= j\sqrt{\pi/2}\,\tau_p \left\{\exp\left[-(\omega+\omega_o)^2\tau_p^2/2\right] - \exp\left[-(\omega-\omega_o)^2\tau_p^2/2\right]\right\}. \end{aligned} \tag{A.21}$$

[3]For a polarization match, the state of polarization for the incident plane wave in a particular direction (reception) is matched to the state of polarization for the radiated field in the same direction (transmission). For example, if the radiated electric field is linearly polarized, the electric field of the incident plane wave is linearly polarized and points in the same direction. If the radiated electric field is right-handed circularly polarized, the electric field of the incident plane wave is right-handed circularly polarized.

Table A.1: Characteristics for Various Input Signals.

[Missing content: Table data for characteristics of various input signals was not provided in the source material.]

[Note: Verify the coefficient in Equation A.21; the Fourier transform expression was incomplete in the source material.]

The differentiated Gaussian pulse has a rather large fractional bandwidth that is fixed; for example, the bandwidth associated with the points at which the spectrum is 10% (-20 dB) of the maximum is **[missing value]**, where $\omega_{\text{pk}} = 1/\tau_p$ is the frequency at the peak. The modulated sinusoid has a variable fractional bandwidth that is controlled by the relative width of the modulating pulse, $\omega_o \tau_p$; for example, the bandwidth associated with the points at which the spectrum is 10% of the maximum is $\Delta\omega/\omega_o \approx 4.29/\omega_o\tau_p$ (when $\omega_o\tau_p \gg 1$). For the case shown in Figure A.6(b), $\omega_o\tau_p = 15$, so the fractional bandwidth is $\Delta\omega/\omega_o \approx 0.29$, which is much narrower than the fractional bandwidth for the differentiated Gaussian pulse shown in Figure A.6(a).

A.5 Examples of the Use of the Method for Antenna Analysis

In the previous sections, we presented the fundamentals of the FDTD method and described in general how the method is used to analyze an antenna for both transmission and reception. In this section, we show results obtained by applying the method to analyze particular antennas. These examples were chosen to illustrate specific issues that arise and must be dealt with when applying the method.

A.5.1 Cylindrical Monopole: Theoretical Model Versus Experimental Model

The ultimate test for any physical theory is how well its predictions agree with experimental measurements, and this is certainly the case for electromagnetic theory when applied to antennas. One of the most important factors that affect the agreement is how closely the theoretical model for the antenna matches the experimental model. To examine this issue we consider the FDTD analysis of the cylindrical monopole, the image equivalent of the cylindrical dipole, which is arguably the most fundamental antenna.

The monopole antenna, shown in Figure A.7(a), is formed by extending the metallic center conductor of a coaxial line the distance h above an infinite metallic image plane [2], [8]. The dimensions of the transmission line, inner conductor radius a and outer conductor radius b, are chosen so that only the TEM mode propagates in the line for the signals of interest. The FDTD model for the transmitting monopole is shown in Figure A.7(b). All of the conductors in the model are perfect (perfect electric conductors, PECs), and the structure is surrounded by a PML [16]. Because of the rotational symmetry of the structure and the excitation, a two-dimensional cylindrical lattice (ρ, z) with the spatial increments $\Delta\rho$ and Δz is used in the FDTD analysis. A "one-way source" excites the coaxial line, consisting of the electric and magnetic

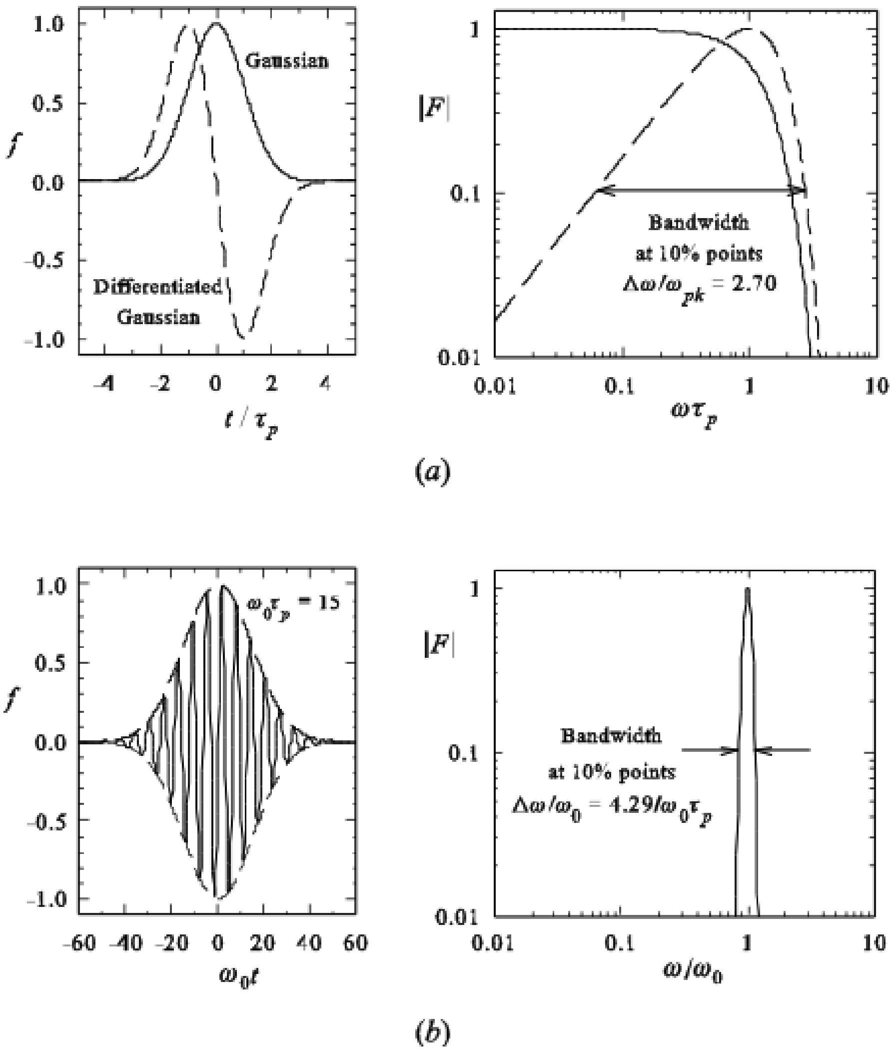

Figure A.6: (a) The Gaussian pulse (solid line) and the differentiated Gaussian pulse (dashed line) and the magnitude of their Fourier transforms. (b) The sinusoid of frequency ω_o amplitude modulated by a Gaussian pulse and the magnitude of its Fourier transform. All waveforms are normalized to have a maximum value of 1.0.

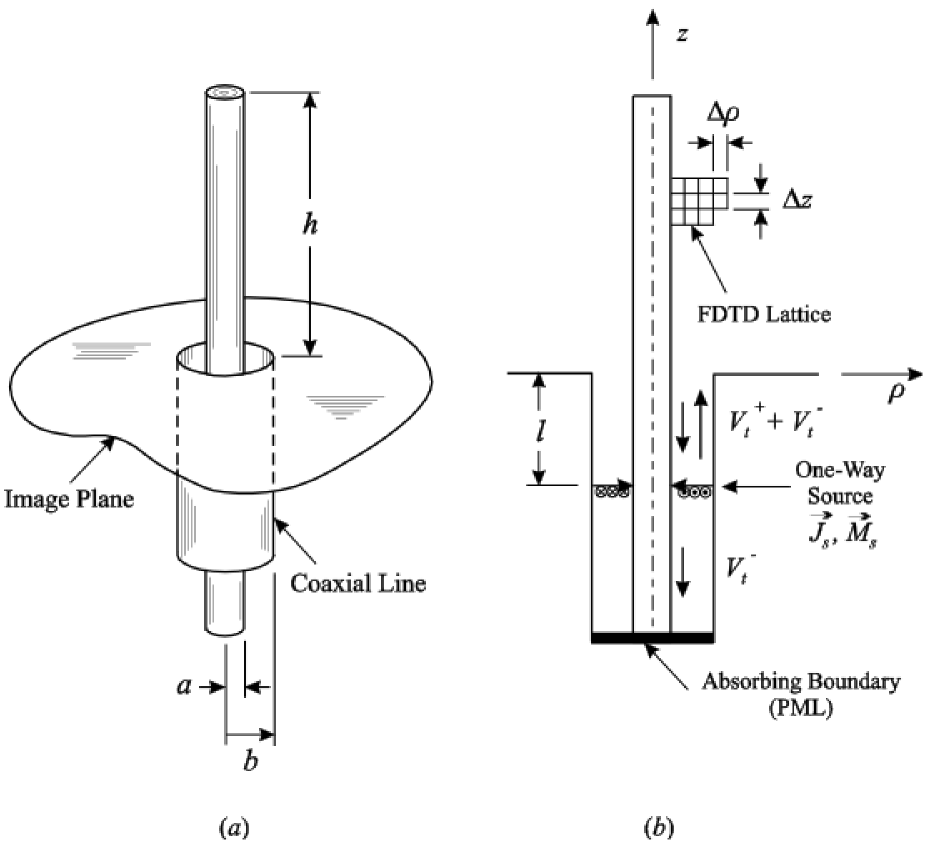

Figure A.7: (a) Cylindrical monopole antenna fed through an image plane from a coaxial transmission line. (b) FDTD model for the cylindrical monopole antenna. The PML that surrounds the computational space is not shown.

surface currents

$$J_s(\rho, t) = -\frac{V_t^+(t)}{2\pi R_o \rho}\hat{\rho}, \quad M_s(\rho, t) = -\frac{\eta_o V_t^+(t)}{2\pi R_o \rho}\hat{\phi} \tag{A.22}$$

on the plane $z = -l$ that produce the incident TEM voltage wave, V_t^+, above the source and a null field below the source. An absorbing boundary is placed at the bottom of the line. With this configuration, only the reflected TEM voltage wave, V_t^-, appears below the source, so it is easily determined. Notice the similarity of this arrangement to the plane-wave source used with the receiving/scattering antenna in Figure A.5.

Figure A.8 is a comparison of results from the FDTD simulation (solid line) with measurements (dots) made on an experimental model corresponding to the geometry in Figure A.7(a). The height of the monopole is $h = 5.0$ cm, and the dimensions of the coaxial line (precision line with APC-7 connector) are $a = 1.52$ mm, $b = 3.5$ mm, which gives a characteristic impedance of $R_o = (\eta_o/2\pi)\ln(b/a) = 50\ \Omega$. The excitation V_t^+ is a unit-amplitude Gaussian pulse in time (Equation A.19), with the characteristic time $\tau_p = 0.161\tau_a$, where $\tau_a = h/c$ is the time for light to travel the length of the monopole.

Figure A.8(a) is for the reflected voltage, V_t^-, in the transmission line, and Figure A.8(b) is for the electric field on the image plane at the radial distance $\rho/h = 12.7$; both are shown as a function of the normalized time t/τ_a. In Figure A.8(a), we see the initial reflection of the incident pulse from the drive point (A), followed by its initial reflection from the open end of the monopole (B). As expected, these events are separated by roughly the time for light to make a round trip on the monopole, $(t_B - t_A)/\tau_a \approx 2$. Additional reflections of decreased amplitude occur each time the pulse encounters the drive point and the open end. In Figure A.8(b), we see that radiation occurs each time the pulse encounters the drive point or the open end of the monopole. As expected, the initial radiation from the drive point (A) is separated from the initial radiation from the open end of the monopole (B) by roughly the time for light to travel the length of the monopole, $(t_B - t_A)/\tau_a \approx 1$. The agreement between the theoretical and measured results is very good.

The FDTD method inherently provides information about the electromagnetic field within the computational volume over the entire period of the simulation. Only a small fraction of this information is used when investigating conventional antenna parameters, such as the results shown in Figure A.8. Sometimes this additional information can be used to perform "numerical experiments" that improve our understanding of the radiation process for the antenna. This is illustrated in Figure A.9, which shows the instantaneous Poynting vector in the region surrounding the monopole [17]. On the right-hand side of these figures, the logarithm of the magnitude of the Poynting vector, $|S|$, is plotted on a color scale. The intensity of the field increases as the hue goes from blue to red, and the range for the values of $|S|$ displayed is $10^4 : 1$. On the left-hand side, the arrows indicate the direction of the Poynting vector, and the length of an arrow is proportional to the logarithm of $|S|$. The excitation is a Gaussian voltage pulse with $\tau_p = 0.0537\tau_a$. For this value of τ_p, about three non-overlapping pulses fit along the length of the monopole, so the reflections associated with different points are separated and easily identified.

In Figure A.9(a), the pulse has just left the drive point and is traveling up the monopole. A spherical wavefront W_1 centered on the drive point has formed, and it is attached to the outward-propagating pulses of charge/current on the monopole and image plane. In Figure A.9(b), the pulse has encountered the open end of the monopole, and it is traveling back down the monopole. A second spherical wavefront W_2 centered on the open end has formed, and it connects the inward-propagating pulse of charge/current on the monopole with the wavefront W_1. Additional wavefronts, W_2', W_3, etc., shown in Figure A.9(c), are produced each time the pulse encounters the drive point and the open end. All of these spherical wavefronts travel outward at the speed of light. The Poynting vectors are seen to be predominantly normal to the wavefronts, which indicates that energy is being transported away from both the drive point and the open end.

The input impedance or admittance $Y_A(\omega) = 1/Z_A(\omega) = G_A(\omega) + jB_A(\omega)$ of the monopole antenna is a useful parameter for practical applications, and it is also a sensitive measure of the accuracy of any theoretical model. It is easily calculated from

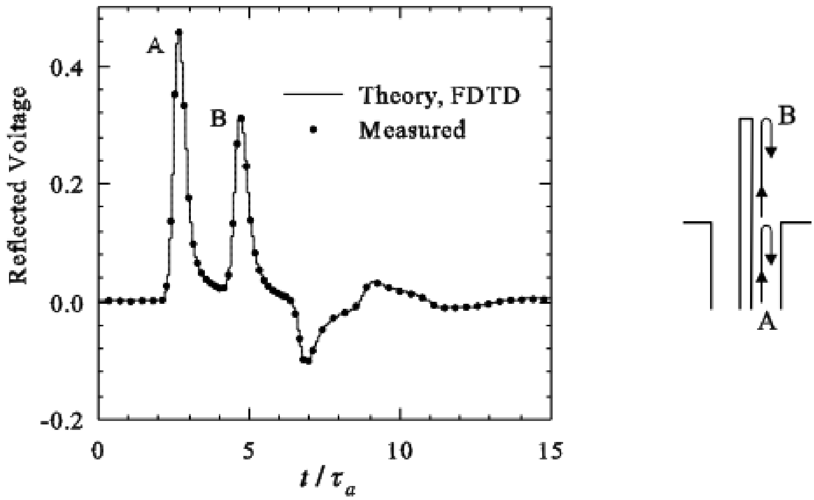

(*a*)

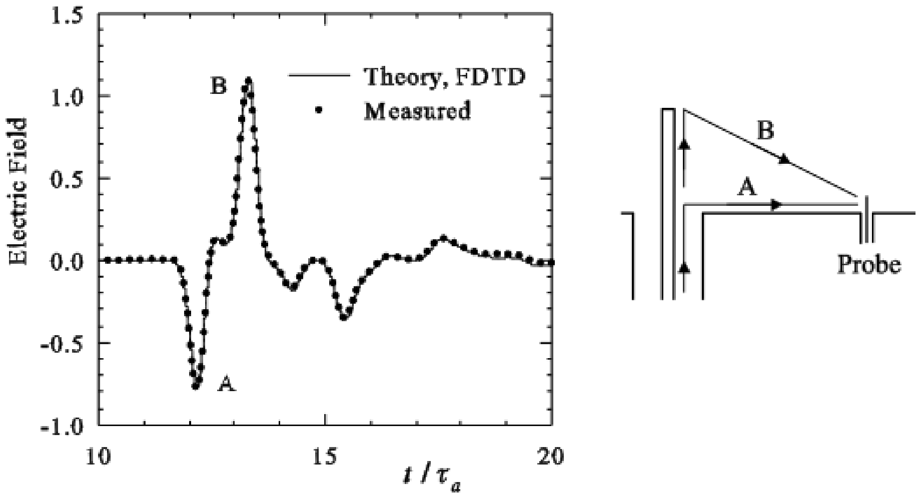

(*b*)

Figure A.8: Comparison of theoretical and measured results for the cylindrical monopole antenna. (a) Reflected voltage in the coaxial line. (b) Electric field on the image plane at $\rho/h = 12.7$.

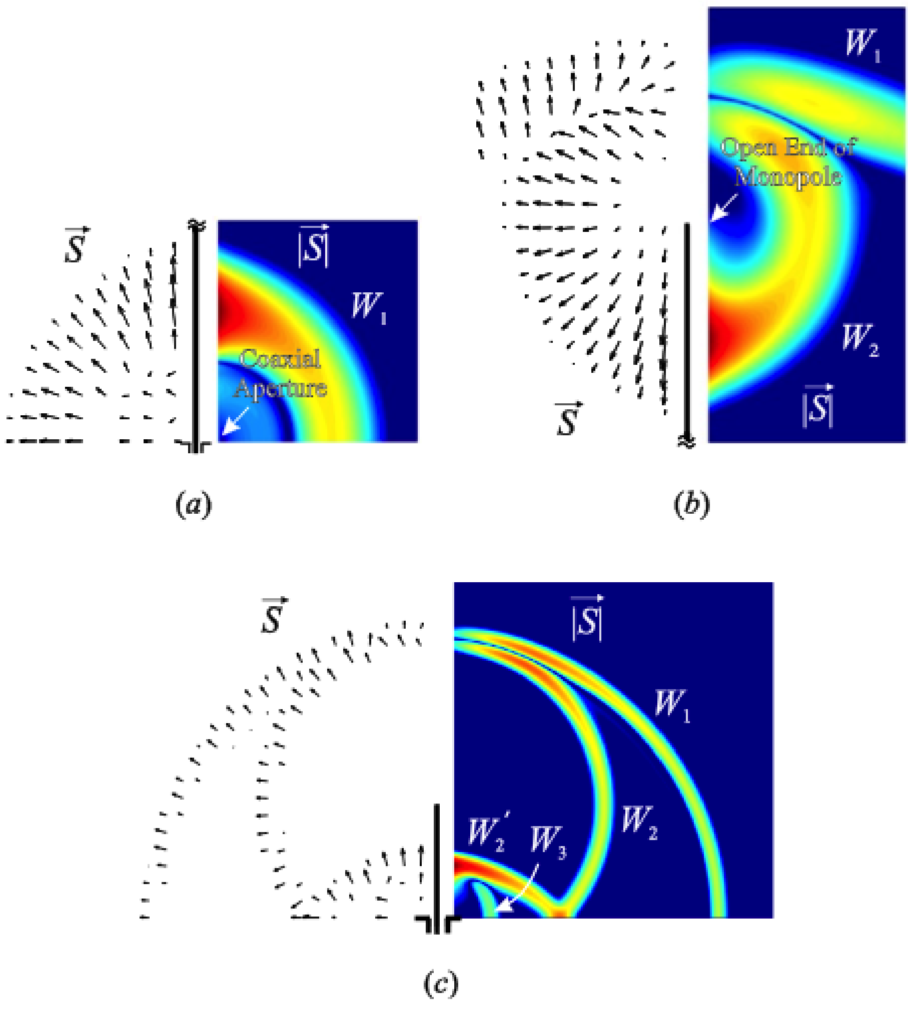

Figure A.9: Three snapshots in time showing the magnitude (right) and direction (left) of the Poynting vector surrounding the cylindrical monopole antenna. Logarithmic scaling is used for both plots. Notice that (a) and (b) only show a portion of the monopole. (After Smith and Hertel [17], © 2001 IEEE.)

Table A.2: FDTD Discretization Parameters for the Cylindrical Monopole Antenna.

[Missing content: Table data for discretization parameters (A, B, C) was not provided in the source material. Should include cell size, number of cells across the gap, number of cells along monopole, and cells per wavelength at the highest frequency.]

the FDTD time-domain results using Equations (A.12) and (A.13). In Figure A.10 the input admittance is graphed as a function of frequency for a monopole with the same dimensions as used for Figure A.8 [18]. FDTD results (lines) for three different levels of discretization (A, B, C) are compared with measurements (dots). The parameters for the three levels of discretization are given in Table A.2.

In this graph we observe the convergence of the FDTD method. Consider the input susceptance, B_A; the result for discretization A is slightly displaced from the measured values, while the results for discretizations B and C are essentially the same as the measured values. Hence, we can conclude that, for practical purposes, the FDTD results for the input admittance have converged to the measured values at discretization B, which corresponds to four FDTD cells across the gap in the coaxial line or 101 cells along the length of the monopole. Note that the dimensions of the FDTD cell for this example had to be chosen so that an integral number of cells fit along the dimensions of the antenna, so the cells are not perfectly square. Discretization B corresponds to 135 cells per wavelength at the highest frequency ($f = 4.5$ GHz) and a relative error in the phase velocity (Equation A.3 and Figure A.2 for $S = 0.5$) of only $6.77 \times 10^{-3}\%$. For this example, it is not the error in the phase velocity that determines the accuracy of the solution. The fine details of the structure must be accurately modeled, and this requires cells that are much smaller than needed for a small error in the phase velocity.

The very good agreement between the theoretical results and the measurements evident in Figures A.8 and A.10 is a consequence of the close match of the theoretical model for the monopole, Figure A.7(b), to the experimental model, Figure A.7(a). In some cases, additional constraints on the analysis require a reduction in the fidelity of the FDTD model, and such good agreement cannot be expected. To illustrate the effect a reduction in the fidelity of the model can have on the accuracy of the results, we examine some common simplifications used for the FDTD model of the monopole.

For the models shown in Figure A.11, the cylindrical conductor of the monopole has been replaced by an equivalent square conductor [19]. Thus, the monopole can now be analyzed using the conventional three-dimensional rectangular FDTD lattice rather than the two-dimensional cylindrical lattice of Figure A.7(b).

The excitation for the monopole has also been changed from that in Figure A.7(b). For the model in Figure A.11(a), the so-called "hard source" is used. This specifies the total voltage $V_t = V_t^+ + V_t^-$ across the gap of length l_g at the base of the monopole. For the model in Figure A.11(b), a virtual one-dimensional transmission line is connected across the gap at the base of the monopole [20]. This transmission line contains the same elements as the transmission line in Figure A.7(b), in particular, a one-way source that specifies the incident voltage V_t^+. We refer to this line as virtual because it does not appear in the FDTD lattice surrounding the monopole. It is in a different location and coupled to the monopole through the voltage and current at its terminals. The hard

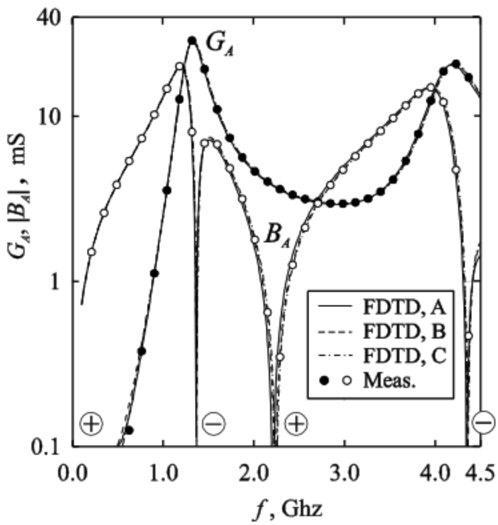

Figure A.10: Comparison of theoretical and measured results for the input admittance of the cylindrical monopole antenna. Results are shown for three levels of discretization (A, B, C) in the FDTD method. (After Hertel and Smith [18], © 2003 IEEE.)

source, while simple to implement, suffers from two drawbacks not present with the transmission line feed. There is no damping in the hard source, unless resistance is added, so the currents on the antenna can ring for a long period of time. Also, the total voltage is specified, so the reflected voltage, a quantity often of interest in time-domain simulations, is not readily available.

In Figure A.12, FDTD results for the input admittance for both models in Figure A.11 are compared with measurements made with the configuration shown in Figure A.7(b) [18]. The level of discretization used is such that the simulations have converged for practical purposes. The theoretical results for the input conductance, G_A, for both models are in very good agreement with the measurements; however, those for the input susceptance, B_A, differ from the measurements, particularly for the hard source (dashed line). The difference in susceptance is a consequence of the geometry for the simplified models not accurately representing the experimental model, Figure A.7(a), in the vicinity of the drive point (the aperture of the coaxial line). The susceptance for the simplified models can be brought into better agreement with the measured results by adding a small capacitance in parallel with the terminals of the monopole [18].

A.5.2 Metallic Horns and Spirals: Stair-Stepped Surfaces

For the monopole antennas discussed in the previous section, the boundaries of the FDTD cells as well as the boundaries of all material regions (PECs) coincided with surfaces of constant coordinate. Thus, the boundaries of material regions never passed obliquely through an FDTD cell. This is a special case that is not encountered for most antennas.

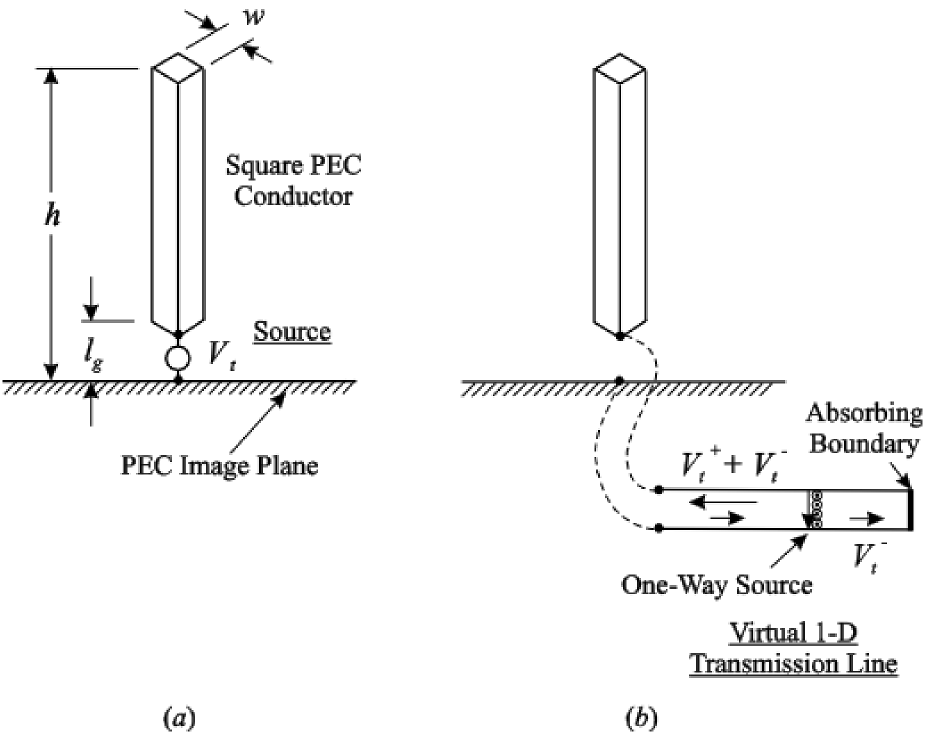

Figure A.11: Simplified models for the cylindrical monopole antenna. (a) Model incorporating a "hard source." (b) Model incorporating a virtual one-dimensional transmission line. The monopole conductor has a square cross section in both models.

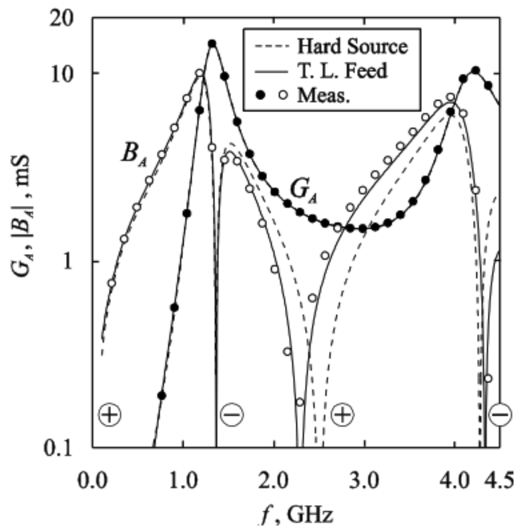

Figure A.12: Comparison of theoretical and measured results for the input admittance of the cylindrical monopole antenna. Results are shown for the two simplified FDTD models. (After Hertel and Smith [18], © 2003 IEEE.)

Figure A.13(a) illustrates the more general case. It shows the cross section of a PEC object with the rectangular FDTD lattice superimposed. The curved surface of the object does not coincide with any of the lattice lines. For the computation we only need to know the field in the FDTD cells that are exterior to the PEC, because both E and H are zero inside the PEC. There are different approaches that can be used for this case. One approach is to introduce non-rectangular FDTD cells that conform to the surface of the object; these cells could be used throughout the computational volume or just adjacent to the object [21]–[23]. Another much simpler approach, shown in Figure A.13(b), is to deform the curved surface of the object so that it conforms to the rectangular FDTD lattice. The surface of the object is said to be replaced by a "stair-stepped" or "staircase" approximation. The stair-stepped approximation will introduce an error, but often the error can be made negligible by choosing the size of the staircase to be small compared to the physical dimensions of the object [24], [25]. The stair-stepped approximation is commonly used, and it is the only approach we will consider in this introductory treatment.

We now consider two practical antennas for which the stair-stepped approximation was used in modeling the structure in the FDTD analysis. As these examples will show, when properly used, the approximation can yield results that are in good agreement with experimental measurements. The first example is the metallic, pyramidal horn shown in Figure A.14 (Flann Microwave Instruments Ltd. Model 1624-20). Antennas like this are used in many microwave applications, and sometimes they serve as gain standards (standard gain horns). The small drawings at the bottom of the figure show the lengths and angles that describe this particular horn antenna: $a = 10.95$ cm, $b = 7.85$ cm,

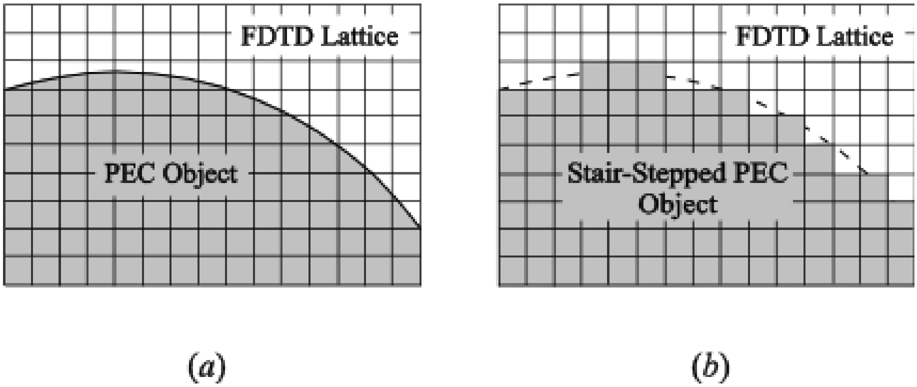

Figure A.13: (a) Rectangular FDTD lattice superimposed on the cross section of an object that is a perfect electric conductor (PEC). (b) The surface of the object has been deformed to conform to the rectangular lattice; the surface of the object has been replaced by a stair-stepped approximation.

$D = 2.284$ cm, $l_w = 5.08$ cm, $\alpha = 10.74°$, and $\beta = 8.508°$. The waveguide feeding the horn is type WR-90 (X-Band, with the operational bandwidth 8.2–12.4 GHz).

In the FDTD model, the cubical cells have the side length $\Delta x = 0.635$ mm, and the perfectly-conducting walls are plates two cells thick. The inset shows the faces of the individual cells that model the bottom wall of the horn; the cells are shown seven times actual size. The slanted sides of the horn are stair stepped, as indicated in the figure, with a "tread length-to-rise" of approximately six cells to one. The horn is fed by a probe inserted into the section of rectangular waveguide, and the incident and reflected voltages in a one-dimensional transmission line ($R_o = 50\ \Omega$) connected to the probe are used in the analysis.

The structure is symmetrical about the x-z plane, and this symmetry was used in the analysis to reduce the size of the computational volume, which was $519 \times 116 \times 183$ cells. The sides of the antenna were 20 cells from the PML absorbing boundary (10 cells thick), except the front side (radiating aperture), which was 40 cells from the absorbing boundary.

The pyramidal horn was first analyzed as a transmitting antenna. The excitation in the transmission line, $V_t^+(t)$, was a differentiated Gaussian pulse (Equation A.20) with the characteristic time $\tau_p = 1.59 \times 10^{-11}$ s. This pulse has significant energy over the operational bandwidth of the horn: 8.2–12.4 GHz. The peak of the spectrum for the pulse is at 10.0 GHz, and the spectrum drops to 10% of the peak at 600 MHz and 27.6 GHz.

At the highest frequency (shortest wavelength) within the operational bandwidth of the horn we have $\Delta x = 0.0226\lambda$, which corresponds roughly to 38 cells per wavelength. From this result, we can estimate the numerical dispersion using Figure A.2 or Equation (A.3). The relative error in the phase velocity is about 0.1%, which is equivalent to 8.1×10^{-3} degrees of phase error per cell, or a total error of 4.2 degrees of phase error for propagation across the longest side of the computational volume.

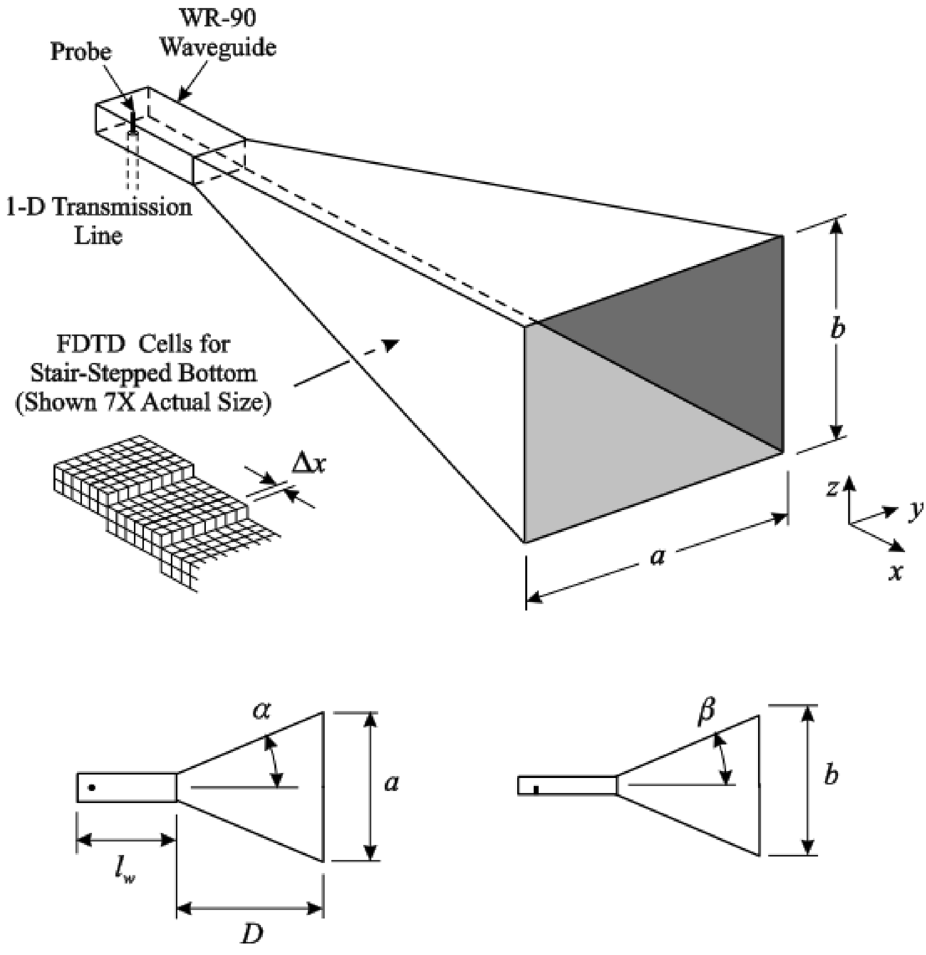

Figure A.14: Schematic drawing for the pyramidal horn antenna. The inset shows the FDTD cells used to model the bottom of the horn.

Figure A.15 is a comparison of the FDTD results (solid line) for this antenna with measurements (dots). The measured data were kindly supplied by Dr. David G. Gentle of the National Physical Laboratory, Teddington, Middlesex, U.K. Figures A.15(a) and A.15(b) show the E- and H-plane field patterns at the frequency 10 GHz, and Figure A.15(c) shows the gain on boresight as a function of frequency. The results from the FDTD calculations are in very good agreement with the measurements. The small differences that do exist in the H-plane field pattern are for angles at which the field is very weak, 50 dB below the peak. We note that the precise details of the probe feeding the waveguide in the FDTD model do not affect the calculation of the gain (Equation A.15) of the horn. This would not be the case if the realized gain (Equation A.14) were determined.

The pyramidal horn was also analyzed as a receiving antenna. For this case, a plane wave was incident from the boresight direction ($\hat{k}_i = -\hat{x}$) with the electric field pointing in the z direction. The incident electric field was a differentiated Gaussian pulse in time (Equation A.20) with the same characteristic time as used for the transmitting case, $\tau_p = 1.59 \times 10^{-11}$ s. The effective area obtained from the receiving analysis was converted to a gain using Equation (A.18), and the result is shown as a dashed line in Figure A.15(c). As expected from reciprocity, the results from the two FDTD calculations (transmitting and receiving) are nearly identical.

The FDTD method provides the field throughout the computational volume, and it can be used to construct graphical results that illustrate the process of radiation for the transmitting horn antenna. For such illustrations, we want an excitation whose spectrum lies within the operational bandwidth of the antenna. Frequencies outside of this band will either be cutoff in the waveguide or overmode the waveguide. A good choice for the voltage $V_t^+(t)$ is the sinusoid of frequency ω_o amplitude modulated by a Gaussian pulse, i.e., Equation (A.21) shown in Figure A.6(b). With $f_o = \omega_o/2\pi = 10.0$ GHz and $\tau_p = 7.96 \times 10^{-11}$ s, the spectrum for this signal is 10% of its peak at $f = 5.7$ GHz and $f = 14.3$ GHz.

Figure A.16 shows three gray-scale plots for the magnitude of the electric field on the x-z plane of the transmitting antenna. In Figure A.16(a) the pulse has entered the horn from the waveguide, but it has not reached the aperture. The spacing between the white lines (nulls) roughly corresponds to one half of a guide wavelength. Notice that this spacing decreases on going from the throat of the horn towards the aperture. In the rectangular waveguide, the guide wavelength is about 1.3 times the free-space wavelength, whereas at the aperture of the horn it is closer to the free-space wavelength. Figure A.16(b) is for a time when the pulse has reached the aperture. Notice that the white lines in the horn near the aperture are distorted; there is a small segment that is concave to the right. This is caused by the reflection from the aperture that is traveling back toward the throat of the horn. Directly in front of the aperture, the radiated wave is roughly planar. In Figure A.16(c), the field has propagated away from the horn, and a spherical wavefront has formed that is approximately centered on the aperture. The change in the shade of gray in going around the antenna (dark in front to light in back) clearly shows a large "front-to-back ratio" for the horn. In the forward direction, minima appear along the wavefront, and these minima will define the main beam in the far zone. Back in the horn, the field has several minima and maxima across its width, indicating the presence of higher-order modes that were excited when the initial pulse

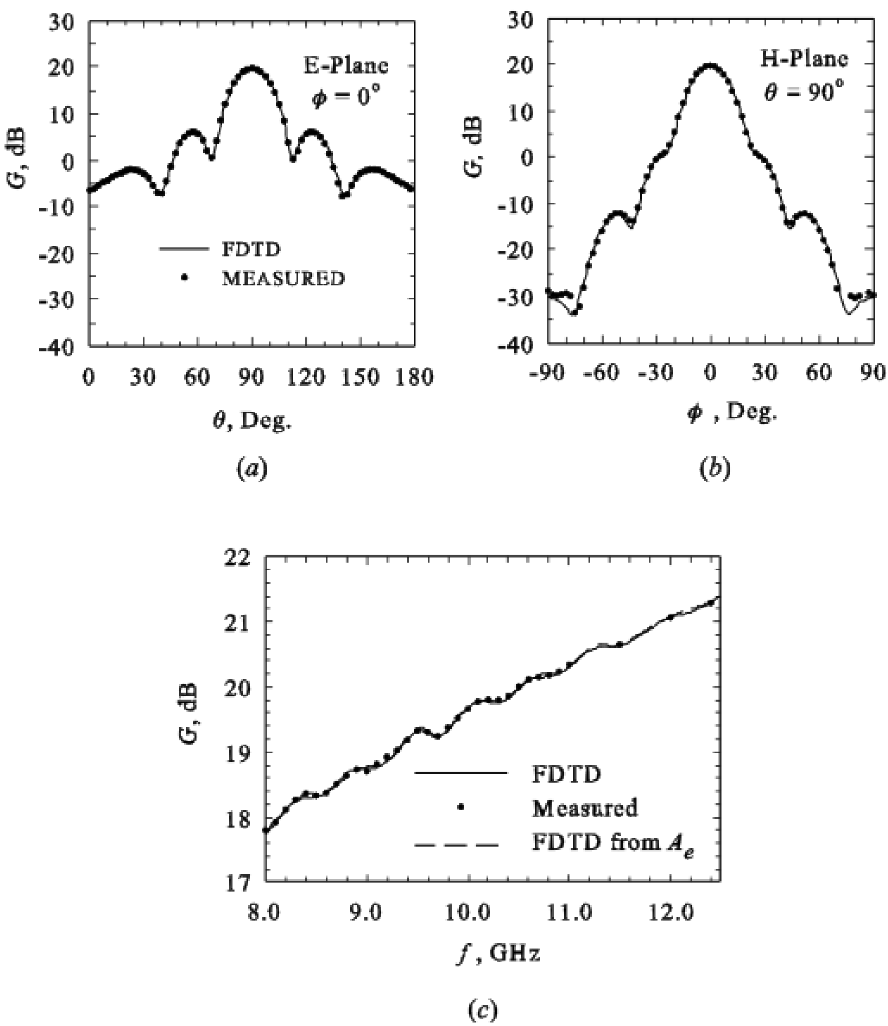

Figure A.15: Comparison of theoretical and measured results for the pyramidal horn antenna. (a) E-plane pattern and (b) H-plane pattern at 10 GHz. (c) Boresight gain versus frequency.

encountered the aperture.

The second example is the two-arm, conical spiral antenna shown in Figure A.17 [26]. It is used in applications that require an antenna to radiate circular polarization over a broad bandwidth. This antenna is formed by winding two metallic strips around the surface of a truncated cone. The angles and dimensions for the particular antenna we consider are $d = 1.9$ cm, $D = 15.2$ cm, $\theta_o = 7.5°$, $\alpha = 75°$, and $\delta = 90°$. It is designed to have constant gain and input impedance ($Z_A \approx 100\ \Omega$) over an operational bandwidth extending from $f_{\text{min}} = 0.5$ GHz to $f_{\text{max}} = 3.3$ GHz.

In the FDTD model, the arms of the spiral are formed by making selected faces of the cubical cells ($\Delta x = 0.8$ mm) PEC. The result is the stair-stepped approximation in Figure A.18. For clarity, only the lower 10% of the antenna is shown in the figure. The spiral is fed by a one-dimensional transmission line ($R_o = 100\ \Omega$) connected at the bottom of the antenna, the same arrangement as used with the monopole antenna in Figure A.11(b). The excitation in the transmission line, $V_t^+(t)$, is a differentiated Gaussian pulse (Equation A.20), whose spectrum is centered on the operational bandwidth of the antenna.

The computational volume was $691 \times 240 \times 240$ cells, with the sides of the antenna 15 cells from the PML absorbing boundary (10 cells thick), except the bottom side (main direction for radiation), which was 30 cells from the absorbing boundary. At the highest frequency (shortest wavelength) within the operational bandwidth of the antenna we have $\Delta x = 0.0093\lambda$, which corresponds roughly to 107 cells per wavelength. From this result, we can estimate the numerical dispersion using Figure A.2 or Equation (A.3). The relative error in the phase velocity is about 0.01%, which is equivalent to 3.6×10^{-4} degrees of phase error per cell, or a total error of 0.25 degrees of phase error for propagation across the longest side of the computational volume. As with the earlier case of the monopole antenna, it is not the error in the phase velocity that determines the accuracy of the solution but the degree to which the fine details of the structure are modeled.

Figure A.19 is a comparison of the FDTD results (solid line) for this antenna with measurements (dashed line). Figure A.19(a) shows the magnitude of the reflection coefficient at the terminals of the antenna, and Figure A.19(b) shows the realized gain (Equation A.14) at boresight ($-\hat{z}$ direction) as a function of frequency. The results from the FDTD calculations are in fairly good agreement with the measurements. The differences that do exist are most likely caused by elements in the experimental model that were not included in the theoretical model. In the experimental model, the metallic arms were on a very thin dielectric substrate (Kapton, thickness 0.051 mm), which was not included in the theoretical model. In addition, the terminal measurements were made through a balun, and the imperfections in the balun were not taken into account.

The FDTD method provides detailed information about the electromagnetic field surrounding the spiral, and it can be used to graphically illustrate how energy is radiated from this structure [27]. Figure A.20 shows three gray-scale plots of the magnitude of the x component of the electric field on the x-z plane. Each plot is for a different normalized time t/τ_L, where τ_L is the time for light to travel the length of the spiral arm. We can see that the radiation is roughly periodic with the spacing between the nulls (white lines) being $\lambda/2$. The frequency corresponding to this wavelength is indicated on each plot. These plots clearly show that the region from which radiation leaves

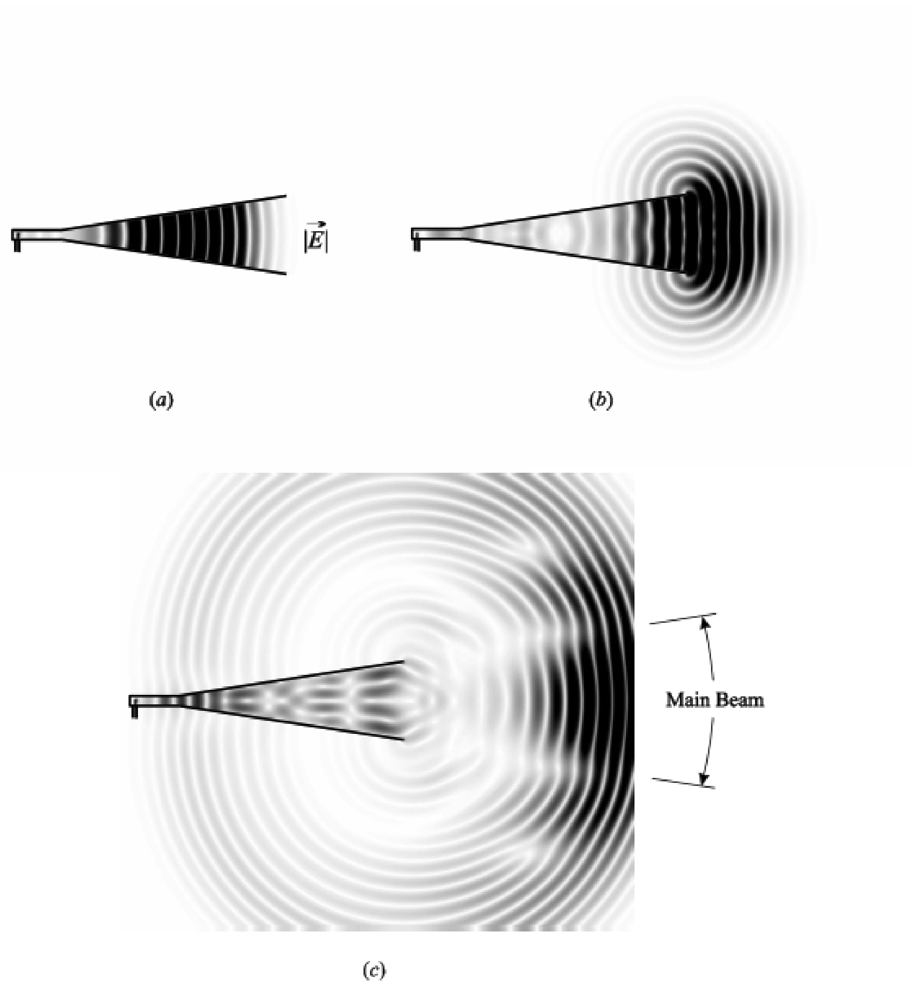

Figure A.16: Gray-scale plots for the magnitude of the electric field on the vertical symmetry plane of the transmitting horn antenna. The excitation is a sinusoid amplitude modulated by a Gaussian pulse.

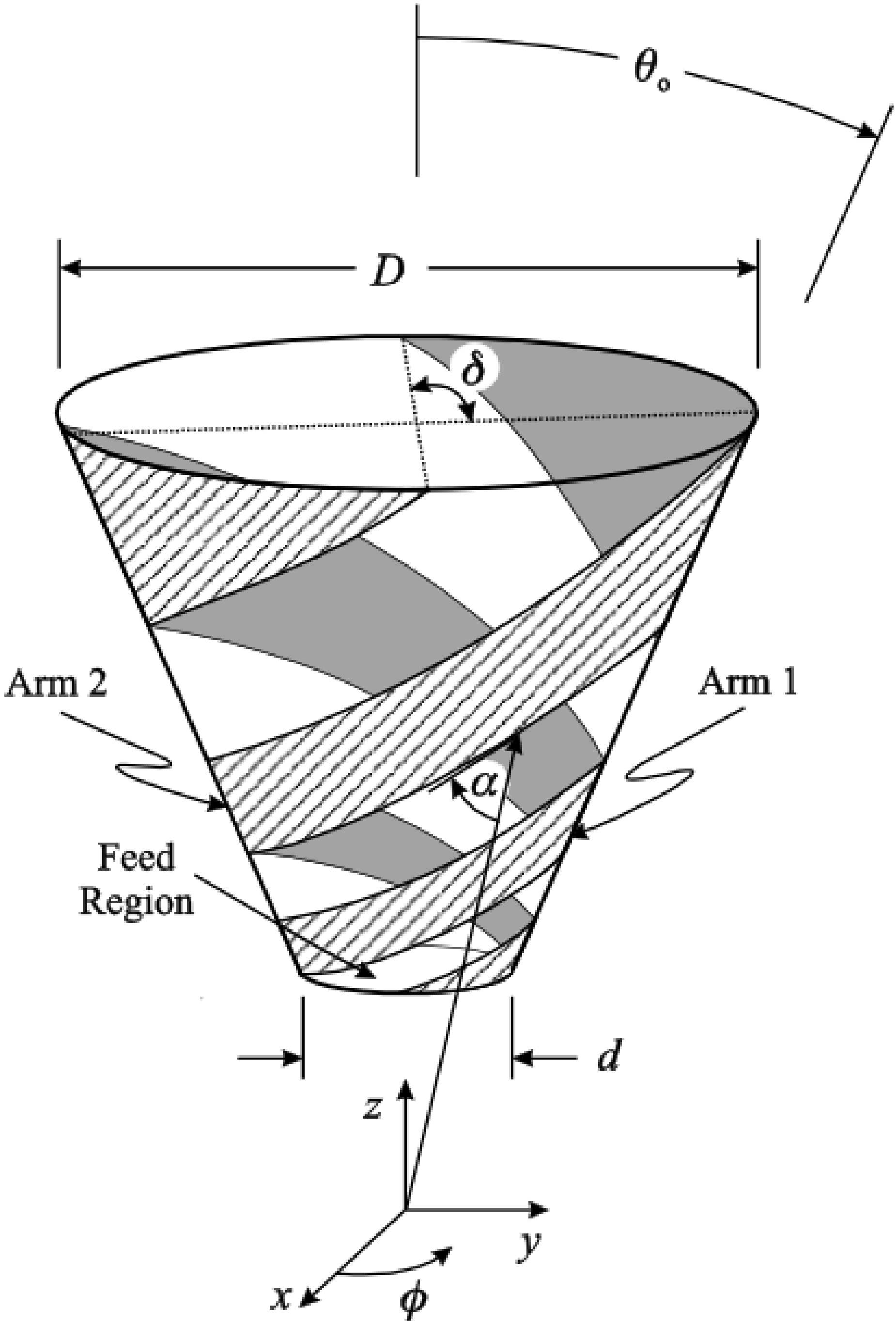

Figure A.17: Geometry for the two-arm conical spiral antenna. (After Hertel and Smith [26], © 2002 IEEE.)

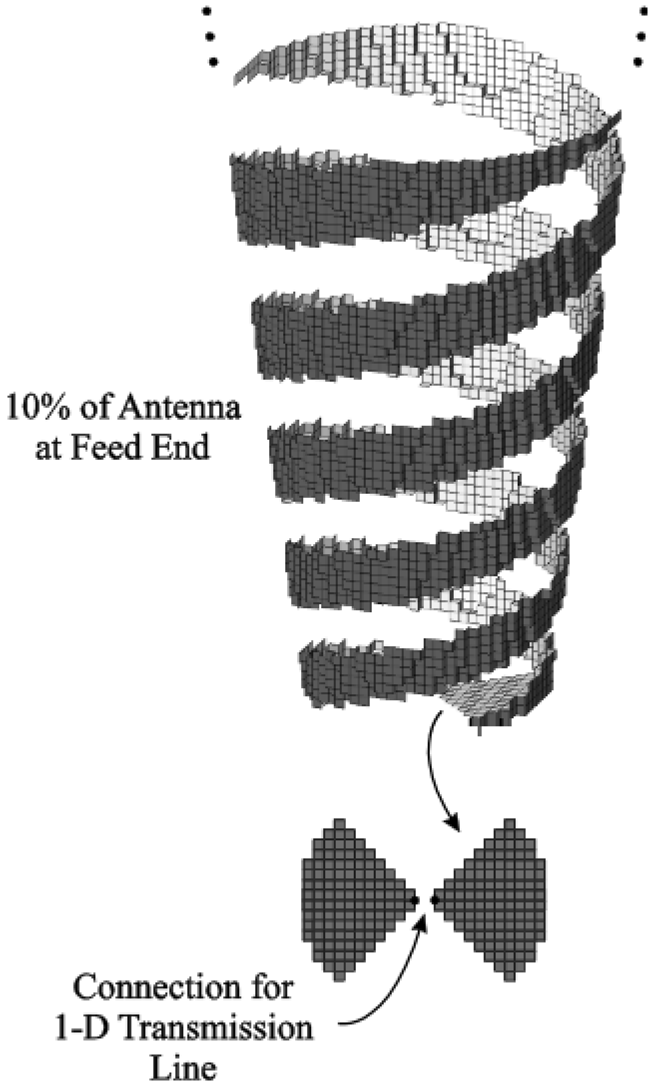

Figure A.18: Schematic drawing showing the arrangement of FDTD cells used to model the conical spiral antenna. For clarity, only the lower 10% of the antenna is shown. (After Hertel and Smith [26], © 2002 IEEE.)

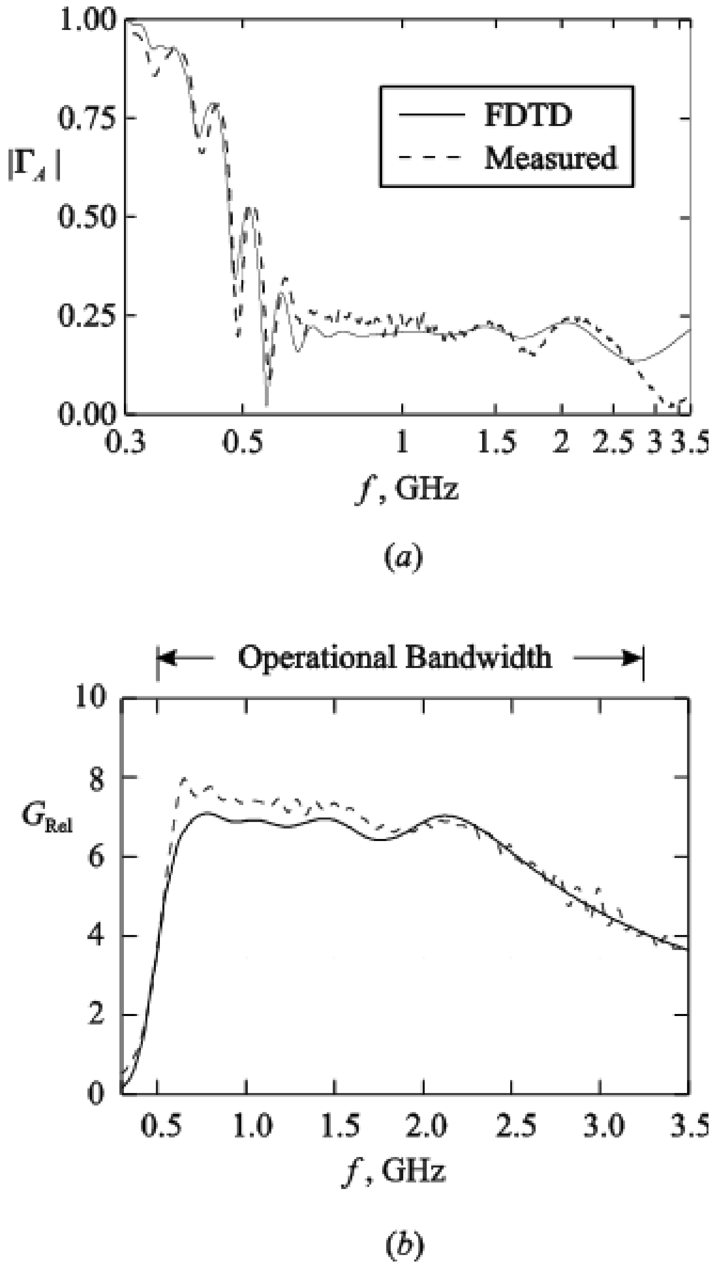

Figure A.19: Comparison of theoretical and measured results for the conical spiral antenna. (a) Magnitude of reflection coefficient versus frequency. (b) Realized gain in the boresight direction versus frequency. (After Hertel and Smith [26], © 2002 IEEE.)

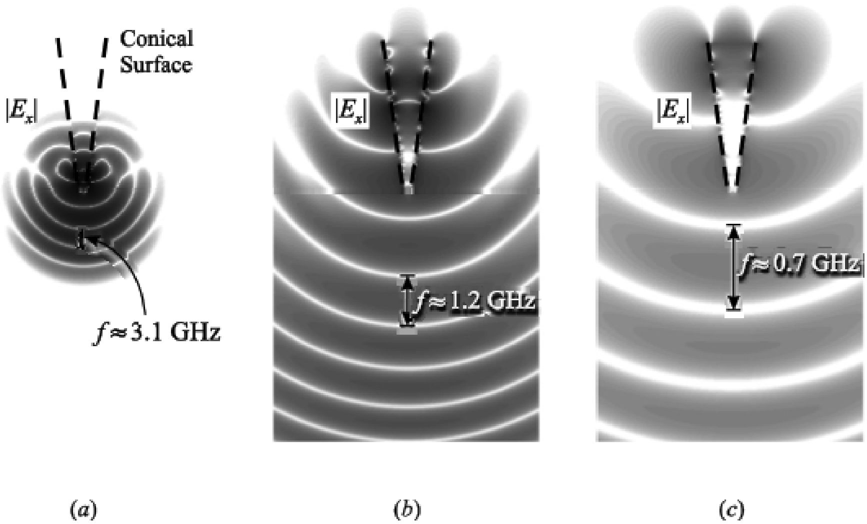

Figure A.20: Gray-scale plots for the magnitude of the electric field near the conical spiral antenna for three instants in time: (a) $t/\tau_L = 0.1$, (b) $t/\tau_L = 0.6$, and (c) $t/\tau_L = 1.1$, where τ_L is the time for light to travel the length of the spiral arm. (After Hertel and Smith [27], © 2003 IEEE.)

the antenna changes with the wavelength, moving from the small end (diameter d) for the shortest wavelengths (highest frequencies) to the large end (diameter D) for the longest wavelengths (lowest frequencies). This is in keeping with the "active-region concept," which states that the radiation originates at the cross section of the spiral that is approximately one wavelength in circumference [28].

In the previous two examples, the stair-stepped approximations used for the geometry of the antennas in the FDTD models were adequate for obtaining theoretical results in good agreement with the measurements. This is a consequence of choosing the size of the steps to be small compared to the dimensions defining the geometry of the antennas. For example, for the pyramidal horn, the height of the stair step is only about 10% of the smallest dimension of the antenna (the height of the rectangular waveguide). We will now consider a case in which the stair-stepped approximation leads to significant errors in the calculated results.

The transverse electromagnetic (TEM) horn is a simple antenna used for applications that require broad bandwidth. The FDTD model for the monopole version of this antenna is shown in Figure A.21(a). It is formed from a PEC plate that is an isosceles triangle of side length s and angle at the apex α. The plate is inclined at the angle $\beta/2$ to the PEC image plane, and the antenna is fed by a transmission line connected between the apex of the plate and the image plane. The plate/image plane forms a TEM transmission line, and for the example to be discussed ($\alpha = 25.4°$, $\beta = 11.2°$), the characteristic impedance of this line is $R_o \approx 50\ \Omega$ [29]–[31]. The transmission line feeding the antenna has the same characteristic impedance.

The plate for this antenna is stair stepped in the FDTD model in the manner shown in Figure A.21(b). Two different sizes for the staircase will be examined: Case A for which the rise is $\Delta z = 1$ mm and the tread length is $\Delta s = 1$ cm, and Case B for which $\Delta z = 2$ mm and $\Delta s = 2$ cm. Notice that the level of discretization for Case B is twice as coarse as that for Case A. The smallest dimensions for the horn are at the drive point, where the initial tread for both cases is 4 mm above the image plane. So for Case A, the rise of the staircase, Δz, is about 25% of the smallest dimension of the horn; whereas, for Case B it is about 50% of the smallest dimension.

Figure A.22(a) shows the reflected voltage, $V_t^-(t)$, in the feeding transmission line of the horn when the incident voltage, $V_t^+(t)$, is a unit-amplitude, differentiated Gaussian pulse (Equation A.20) with the characteristic time $\tau_p = 5.31 \times 10^{-11}$ s. The peak of the spectrum for the pulse is at 3.0 GHz. The solid line is for Case A and the dashed line is for Case B. The initial reflection from the drive point is evident and is similar for both cases, and the reflection from the open end of the horn has been windowed out. There is a pronounced ripple in the result for the coarser staircase, Case B. The ripple is clearly due to the staircase, because its period roughly corresponds to the round-trip time on a tread, which is $\Delta t = 2\Delta s_B/c \approx 2.5\tau_p$. Notice that the amplitude of the ripple decreases with time. This is because the reflections that occur later in time are from stair steps further out along the antenna, where the rise of the staircase, Δz, is a smaller fraction of the separation between the plate and the image plane.

Figure A.22(b) shows the magnitude of the Fourier transform (spectrum) of the reflection coefficient for the antenna. Notice that the results for the two cases, A and B, are quite different. Specifically, for Case B there is a distinct dip in the reflection coefficient near $2f\Delta s_B/c = 1$ ($f = 7.5$ GHz). At this frequency, $\Delta s_B/\lambda = 1/2$, so the small reflections from all of the steps in the staircase add in phase.

To avoid the problem described above, we must use a finer staircase, such as in Case A. For TEM horns with low characteristic impedance (generally small β), this can require a very fine level of discretization. A similar problem is encountered with bow-tie antennas with low characteristic impedance [32].

A.5.3 Microstrip Patches: Excessive Ringing for Narrow-Band Antennas

The antennas we examined in the previous section, a conical spiral and horns, are fairly wideband antennas. Now we consider the other extreme, namely, narrowband antennas. For our example, we use the basic, rectangular microstrip patch antenna shown in Figure A.23.

In the mid-1980s, Chang et al. made extensive measurements of this antenna, and first we compare our FDTD results with their measurements [33]. The dimensions for a patch designed for frequencies around $f = 7.0$ GHz are $s = 1.1$ cm, $w = 1.7$ cm, and $h = 3.175$ mm. As shown in the figure, the probe of the feeding coaxial line ($R_o = 50\ \Omega$) is displaced from the broad side of the patch by $l_p = 1.5$ mm. In the model, the dielectric substrate is 10 cm $\times$ 10 cm with the electrical properties $\epsilon_r = 2.33$ and $\sigma = 2.1 \times 10^{-3}$ S/m, and the ground plane is infinite. The inci-

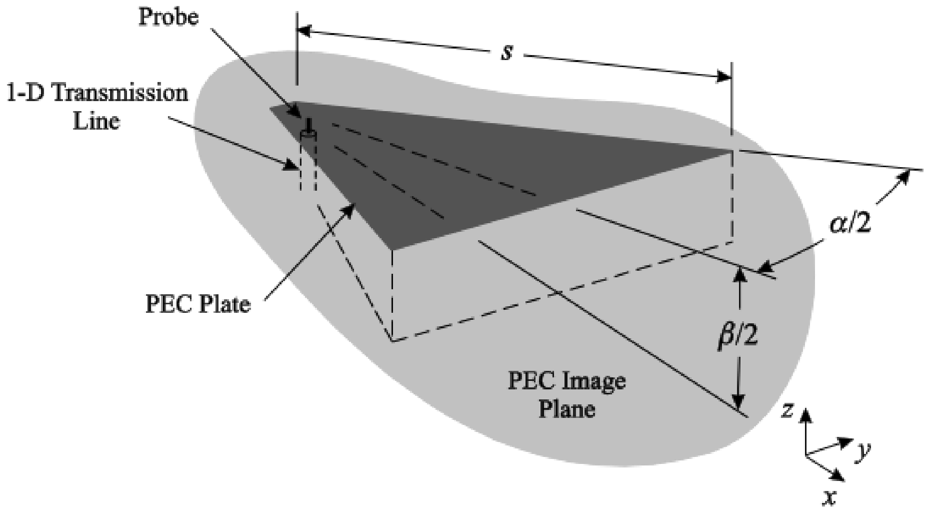

(a)

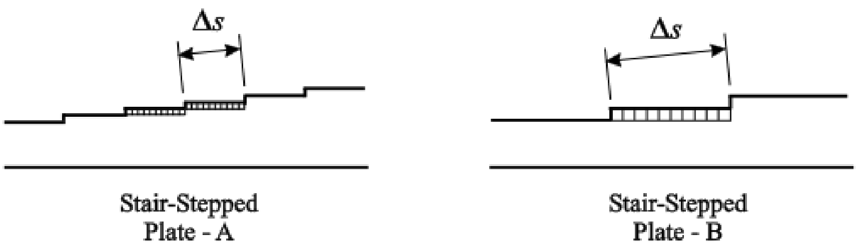

(b)

Figure A.21: (a) Schematic drawing for the TEM horn antenna (monopole configuration). (b) Cross sections showing the stair-stepped approximation to the plate for two different cases, A and B.

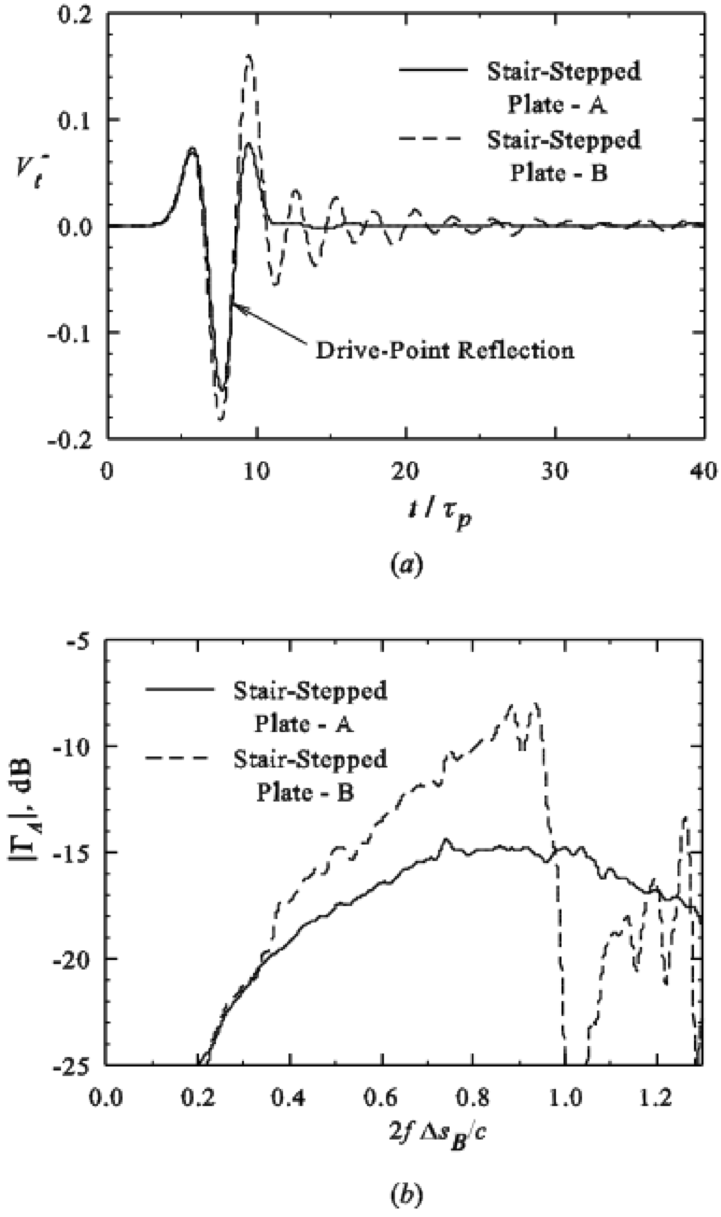

Figure A.22: Results for two different stair-stepped approximations (A and B) applied to the TEM horn antenna. (a) The reflected voltage in the feeding transmission line; the reflection from the open end of the horn has been windowed out. (b) The magnitude of the Fourier transform of the reflection coefficient for the antenna.

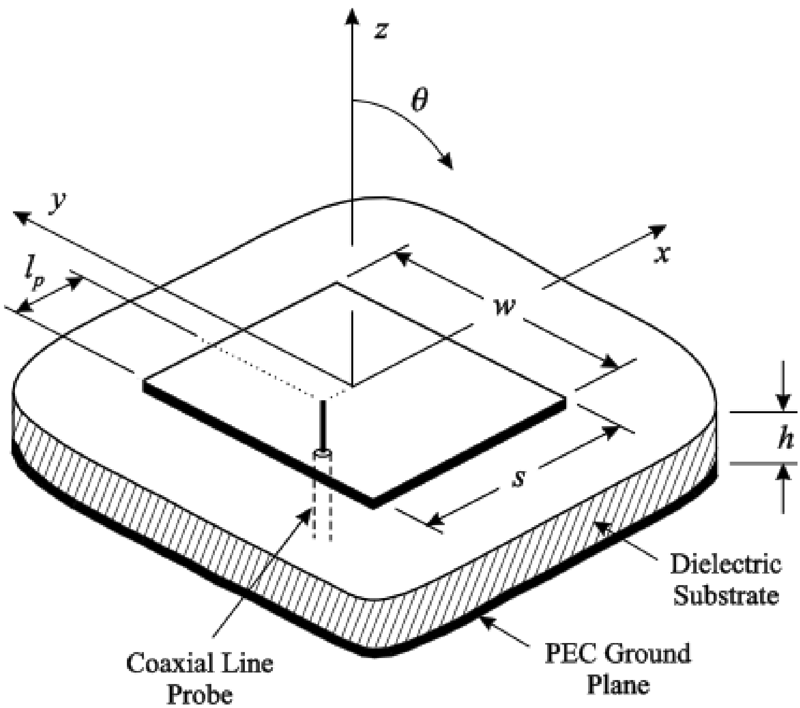

Figure A.23: Rectangular microstrip patch antenna fed by a coaxial line probe.

dent voltage, $V_t^+(t)$, in the feeding transmission line is a unit-amplitude, differentiated Gaussian pulse (Equation A.20) with the characteristic time $\tau_p = 2.65 \times 10^{-11}$ s. The peak of the spectrum for this pulse is at 6.0 GHz.

The dimensions of the FDTD rectangular cells ($\Delta x = 0.529$ mm, $\Delta y = 0.500$ mm, $\Delta z = 0.500$ mm) were chosen so that all of the details of the coaxial feed line could be included in the model, and the time step was $\Delta t = 9.44 \times 10^{-13}$ s. The number of time steps, N_t, required for the simulation was determined by observing the magnitude of the reflected voltage $|V_t^-|$ in the feeding transmission line versus the normalized time $t/\Delta t$; this is shown in Figure A.24(a). Notice that the vertical scale is logarithmic. When $t/\Delta t = 3000$, the reflected voltage has dropped by six orders of magnitude from its peak, and it is at the noise level for the computation. So any number of time steps greater than three thousand was deemed adequate for the simulation ($N_t = 4000$ was actually used).

Figure A.25 is a comparison of the FDTD theoretical results with the measurements. The graph in Figure A.25(a) shows the magnitude of the reflection coefficient versus frequency: theory (solid line) and measurement (dots). The agreement is reasonably good, particularly when we consider that some of the geometrical detail for the measurement, such as the precise geometry at the feed, were not known for use in the FDTD model.

The field patterns were measured with the 10 cm $\times$ 10 cm substrate mounted at the center of a circular aluminum image plane of diameter 1 m. We chose not to model this configuration with the same fine resolution used for the FDTD calculation of the reflection coefficient, because of the large amount of memory that would be required. Instead, larger cells were used with the dimensions $\Delta x = 1.59$ mm, $\Delta y = 1.42$ mm, $\Delta z = 1.57$ mm. The use of the larger cells causes little error in the far-zone field patterns. The FDTD and measured field patterns for the frequency $f = 6.8$ GHz are compared in Figure A.25(b). These plots show the gain (Equation A.15) versus angle, normalized to 0 dB at the peak. Results are given for both the E plane (x-z plane, solid line and dots) and the H plane (y-z plane, dashed line and triangles). Again the agreement is reasonably good.

For our second example, we chose a rectangular microstrip patch antenna designed to operate around $f = 1.9$ GHz that is similar to one reported in the literature [34]. The dimensions for the patch are $s = 5.12$ cm, $w = 6.0$ cm, and $h = 1.575$ mm, and the probe of the feeding coaxial line ($R_o = 50\ \Omega$) is displaced from the broad side of the patch by $l_p = 1.64$ cm. The dielectric substrate ($\epsilon_r = 2.2$ and $\sigma = 1.1 \times 10^{-3}$ S/m) and the ground plane are the same size: 11.5 cm $\times$ 11.5 cm. The incident voltage, $V_t^+(t)$, in the feeding transmission line is a unit-amplitude, differentiated Gaussian pulse (Equation A.20) with the characteristic time $\tau_p = 1.061 \times 10^{-10}$ s, and the peak of the spectrum for this pulse is at 1.5 GHz. Again, the parameters for the FDTD simulation allow complete modeling of the details of the coaxial feed line ($\Delta x = 0.529$ mm, $\Delta y = 0.500$ mm, $\Delta z = 0.500$ mm, $\Delta t = 9.91 \times 10^{-14}$ s). The electrical thickness of the substrate for this example is about one eighth of that for the previous example, $h/\lambda = 0.010$ (for $f = 1.9$ GHz) versus $h/\lambda = 0.077$ (for $f = 7.3$ GHz), so we expect this antenna to have a significantly narrower bandwidth [35].

Figure A.24(b) shows the magnitude of the reflected voltage $|V_t^-|$ in the feeding transmission line (logarithmic scale) versus the normalized time $t/\Delta t$. As a conse-

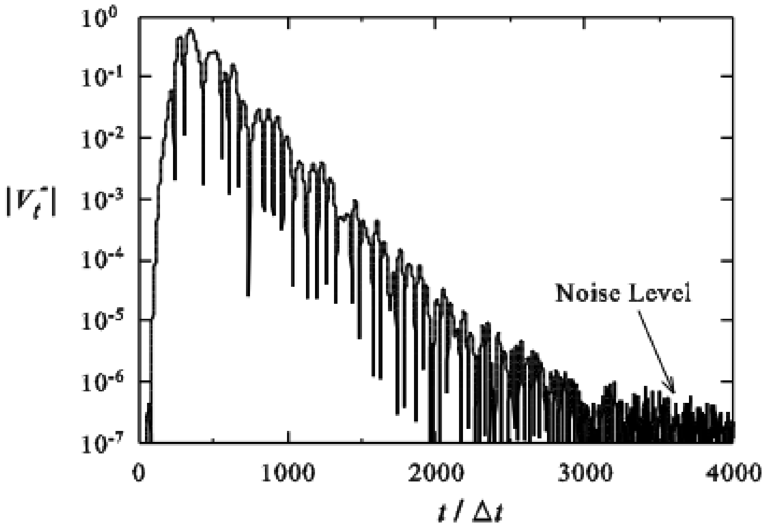

(a)

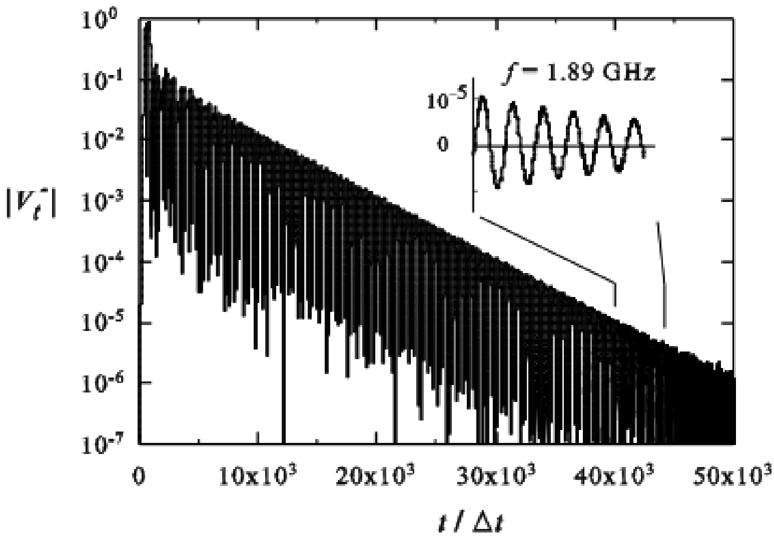

(b)

Figure A.24: The magnitude of the reflected voltage in the feeding coaxial line versus the normalized time. (a) Rectangular microstrip patch. (b) Narrow-band, rectangular microstrip patch.

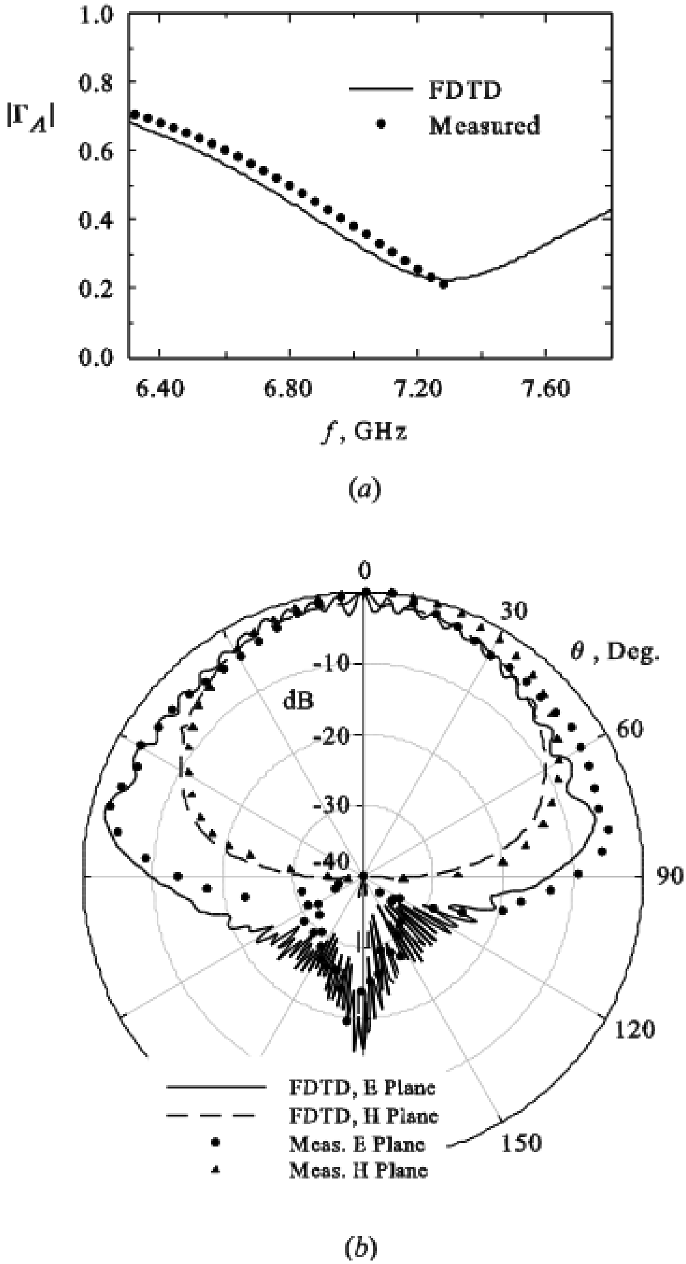

Figure A.25: Comparison of theoretical and measured results for the rectangular microstrip patch antenna. (a) Magnitude of reflection coefficient versus frequency. (b) Field patterns for E and H planes at the frequency $f = 6.8$ GHz. Measured results from [33].

quence of the narrower bandwidth, the reflected voltage decreases much more slowly with increasing $t/\Delta t$ than in the previous example, Figure A.24(a). The reflected voltage has dropped by six orders of magnitude from its peak and is approaching the noise level for the computation when $t/\Delta t = 50{,}000$. So about fifty thousand time steps ($N_t = 50{,}000$) are required for the simulation, as compared to three thousand for the previous example! The inset in Figure A.24(b) shows the magnitude of the reflected voltage, plotted on a linear scale, for times around $t/\Delta t = 40{,}000$. The voltage is seen to be a slowly decaying sinusoid at the frequency $f \approx 1.89$ GHz.

In Figure A.26 we show the magnitude of the reflection coefficient versus frequency for simulations with different numbers of time steps: $N_t = 8{,}000$, $N_t = 24{,}000$, and $N_t = 50{,}000$. For each case, a Hanning window is applied in time to eliminate truncation artifacts. The antenna is seen to be matched at the frequency $f = 1.89$ GHz, and the "apparent" bandwidth for the match is seen to depend on the number of time steps used for the simulation. Thus, if one were to underestimate the number of time steps required for the simulation to converge, one would think that the antenna had a much wider bandwidth for the reflection coefficient than it actually has. With the detailed analysis presented above, this point may appear to be obvious. However, sometimes, particularly when a computation is automated, this degree of analysis may not be performed every time a parameter for the antenna, such as the thickness of the substrate, is changed.

In some cases, special techniques can be applied to shorten the computation for a narrow-bandwidth antenna. For example, because of the well-defined, decaying sinusoidal waveform in the reflection coefficient for this antenna, a shorter computation time, say $N_t = 20{,}000$, could be used with an extrapolation for the remainder of the waveform. Such techniques are discussed in the literature [36].

A.6 Summary and Conclusions

In this appendix, we have presented an introduction to the finite-difference time-domain method, aimed at readers who have little or no experience with the method. We have limited the presentation to the basics of the method, avoiding mention of many refinements that are generally restricted to particular applications. To give the reader a sense of the breadth of application allowed by these refinements, we present a partial list below.

- Techniques for handling materials with dispersive properties (properties that are a function of the frequency), anisotropic properties (properties that depend on the direction of the field components), and nonlinear properties.
- Methods for incorporating impedance boundary conditions.
- Subcell methods for treating material sheets that are thinner than an FDTD cell.
- Methods for incorporating periodic boundary conditions, which are useful in treating antenna arrays.
- Higher-order FDTD schemes that have lower error (numerical dispersion) than the conventional Yee algorithm.

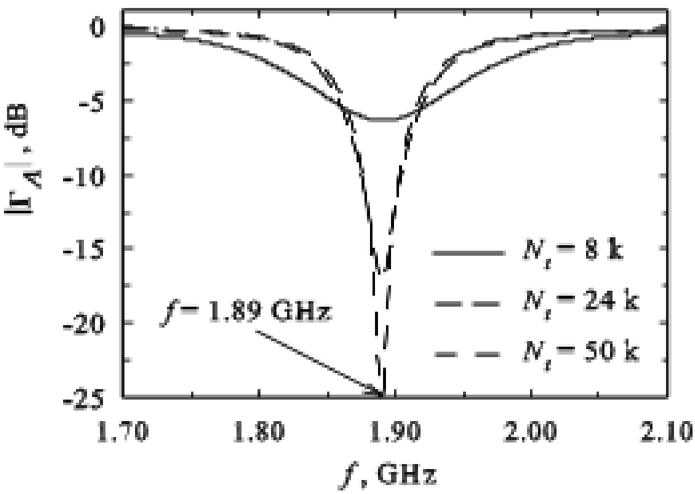

Figure A.26: Narrow-band, rectangular microstrip patch antenna. Magnitude of reflection coefficient versus frequency for three different numbers of time steps.

- Techniques for incorporating nonuniform and nonorthogonal grids.
- Special procedures for handling objects that are bodies of revolution.

The brevity of this appendix precluded the derivation of the mathematical formulas associated with the method, e.g., FDTD update equations, equations for the perfectly matched layer, etc. These formulas can be found in the comprehensive treatment of the method contained in the book edited by Taflove and Hagness [9]. A comprehensive web site on the method is maintained by J. B. Schneider at Washington State University: `www.fdtd.org`. This site contains searchable lists of books, journal papers, conference papers, and dissertations.

To assess the popularity of the FDTD method, a search was done with INSPEC for documents that included either “finite-difference time-domain” or “FDTD” in the title.[4] The results of the search, presented in Figure A.27, clearly show the rapid growth in the popularity of the method over the last twenty-five years.

The emphasis throughout this appendix has been on the application of the FDTD method to the analysis of antennas. After brief discussions of the special formulations associated with transmitting and receiving antennas, the details for the analysis of a few different types of antennas were presented. Because of the brevity of this appendix, no attempt was made to mention all of the different antennas that have been analyzed with the method. Many individuals have used the method to treat antennas; as an indication

[4]A few of these documents apply the finite-difference time-domain method to problems other than electromagnetic, such as acoustic problems.

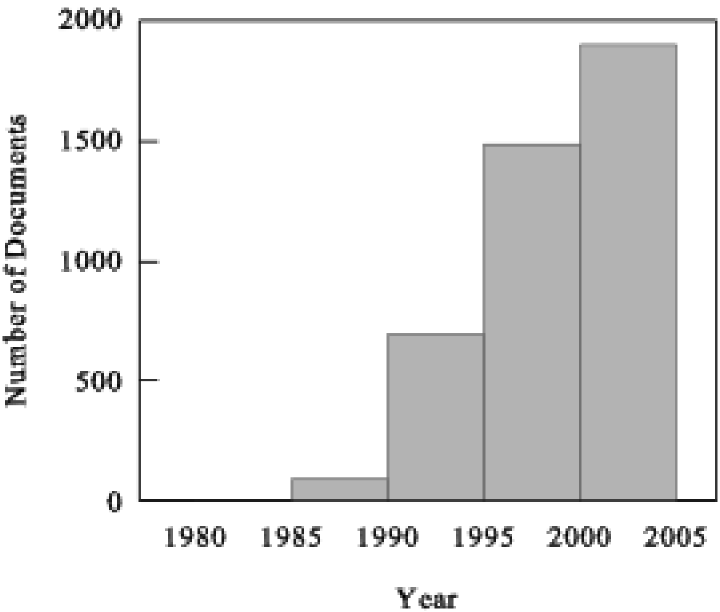

Figure A.27: Number of documents published over a twenty-year span that include the words “finite-difference time-domain” or “FDTD” in the title. Each bar shows the total number of documents published during a five-year period.

of the number, the INSPEC search mentioned above listed over 500 documents with FDTD and antenna(s) in the title.

All of the numerical results presented in the examples were obtained by the authors or their students. Thus, we have very detailed knowledge for each example and can make fairly accurate statements about the results. These examples were chosen not only to show the power of the FDTD method, particularly the good agreement with experimental measurements, but also to show that the method has some limitations—albeit, the limitations are sometimes due to the crudeness of the theoretical model for the antenna or the choice of the parameters for the simulation. The refinement of the FDTD method and its application to practical problems is an ongoing story, and undoubtedly there will be some exciting accomplishments made in the future.

One area with great promise is the use of the method for antenna synthesis. Here we do not mean the conventional approach in which the method is coupled with an optimization routine and used to choose the parameters for a standard antenna (dipole, horn, etc.) so that certain criteria for the performance are met. What we have in mind for antenna synthesis is quite different—a more modern approach. In this approach, the structure of the antenna is not completely predetermined with only a few parameters to be chosen, but the structure of the antenna is actually developed as part of the synthesis. The FDTD method is well suited for use in such schemes; because of the flexibility of the method, a new structure can easily be introduced. The antenna structure is changed by simply changing the electromagnetic constitutive parameters associated with individual cells. *The earlier chapters in this book describe the "fragmented aperture" concept, which relied heavily on the FDTD method as described in this appendix* [37]–[40].

References

[1] K. S. Yee, "Numerical Solution of Initial Boundary Value Problems Involving Maxwell's Equations in Isotropic Media," IEEE Trans. Antennas Propagat., Vol. AP-14, pp. 302–307, May 1966.

[2] J. G. Maloney, G. S. Smith, and W. R. Scott, Jr., "Accurate Computation of the Radiation from Simple Antennas Using the Finite-Difference Time-Domain Method," IEEE Trans. Antennas Propagat., Vol. AP-38, pp. 1059–1068, July 1990.

[3] J. J. Boonzaaier and C. W. Pistorius, "Thin Wire Dipoles: A Finite-Difference Time-Domain Approach," Electronics Lett., Vol. 26, pp. 1891–1892, October 1990.

[4] D. S. Katz, M. J. Picket-May, A. Taflove, and K. R. Umashankar, "FDTD Analysis of Electromagnetic Wave Radiation from Systems Containing Horn Antennas," IEEE Trans. Antennas Propagat., Vol. AP-39, pp. 1203–1212, August 1991.

[5] P. A. Tirkus and C. A. Balanis, "Finite-Difference Time-Domain Method for Antenna Radiation," IEEE Trans. Antennas Propagat., Vol. AP-40, pp. 334–340, March 1992.

[6] R. J. Luebbers and J. Beggs, "FDTD Calculation of Wide-Band Antenna Gain and Efficiency," IEEE Trans. Antennas Propagat., Vol. AP-40, pp. 1403–1407, November 1992.

[7] J. G. Maloney and G. S. Smith, "Modeling of Antennas," Chapter 7 in A. Taflove, Editor, Advances in Computational Electrodynamics, The Finite-Difference Time-Domain Method, pp. 409–460, Artech House, Boston, 1998. Also, J. G. Maloney, G. S. Smith, E. Thiele, O. Gandhi, N. Chavannes, and S. Hagness, Chapter 14 in A. Taflove and S. Hagness, Editors, Computational Electrodynamics: The Finite-Difference Time-Domain Method, 3rd Edition, pp. 607–676, Artech House, Boston, 2005.

[8] G. S. Smith, An Introduction to Classical Electromagnetic Radiation, Cambridge University Press, Cambridge, UK, 1997.

[9] A. Taflove and S. C. Hagness, Editors, Computational Electrodynamics: The Finite-Difference Time-Domain Method, 3rd Edition, Artech House, Boston, 2005.

[10] J. B. Schneider and C. L. Wagner, "FDTD Dispersion Revisited: Faster-Than-Light Propagation," IEEE Microwave and Guided Wave Lett., Vol. 9, pp. 54–56, February 1999.

[11] S. Gedney, "An Anisotropic Perfectly Matched Layer-Absorbing Medium for the Truncation of FDTD Lattices," IEEE Trans. Antennas Propagat., Vol. AP-44, pp. 1630–1639, December 1996.

[12] S. Gedney, "Perfectly Matched Layer Absorbing Boundary Conditions," Chapter 7 in A. Taflove and S. C. Hagness, Editors, Computational Electrodynamics: The Finite-Difference Time-Domain Method, 3rd Edition, pp. 273–328, Artech House, Boston, 2005.

[13] K. L. Shlager and G. S. Smith, "Near-Field to Near-Field Transformation for Use With FDTD Method and Its Application to Pulsed Antenna Problems," Electronics Lett., Vol. 30, pp. 1262–1264, August 1994.

[14] K. L. Shlager and G. S. Smith, "Comparison of Two Near-Field to Near-Field Transformations Applied to Pulsed Antenna Problems," Electronics Lett., Vol. 31, pp. 936–938, June 1995.

[15] G. S. Smith, "A Direct Derivation of a Single-Antenna Reciprocity Relation for the Time Domain," IEEE Trans. Antennas Propagat., Vol. AP-52, pp. 1568–1577, June 2004.

[16] J. G. Maloney, M. P. Kesler, and G. S. Smith, "Generalization of PML to Cylindrical Geometries," 13th Annual Review of Progress in Applied Computational Electromagnetics, Monterey, CA, pp. 900–908, March 1997.

[17] G. S. Smith and T. W. Hertel, "On the Transient Radiation of Energy from Simple Current Distributions and Linear Antennas," IEEE Antennas Propagat. Magazine, Vol. 43, pp. 49–62, June 2001.

[18] T. W. Hertel and G. S. Smith, "On the Convergence of Common FDTD Feed Models for Antennas," IEEE Trans. Antennas Propagat., Vol. AP-51, pp. 1771–1779, August 2003.

[19] R. W. P. King, The Theory of Linear Antennas, p. 20, Harvard Univ. Press, Cambridge, MA, 1956.

[20] J. G. Maloney, K. L. Shlager, and G. S. Smith, "A Simple FDTD Model for Transient Excitation of Antennas by Transmission Lines," IEEE Trans. Antennas Propagat., Vol. AP-42, pp. 289–292, February 1994.

[21] S. Dey and R. Mittra, "A Locally Conformal Finite-Difference Time-Domain (FDTD) Algorithm for Modeling Three-Dimensional Perfectly Conducting Objects," IEEE Microwave and Guided Wave Lett., Vol. 7, pp. 273–275, September 1997.

[22] A. Taflove, M. Celuch-Marcysiak, and S. Hagness, "Local Subcell Models of Fine Geometrical Features," Chapter 10 in A. Taflove and S. C. Hagness, Editors, Computational Electrodynamics: The Finite-Difference Time-Domain Method, 3rd Edition, pp. 407–462, Artech House, Boston, 2005.

[23] S. Gedney, F. Lansing, and N. Chavannes, "Nonuniform Grids, Nonorthogonal Grids, Unstructured Grids, and Subgrids," Chapter 11 in A. Taflove and S. C. Hagness, Editors, Computational Electrodynamics: The Finite-Difference Time-Domain Method, 3rd Edition, pp. 463–516, Artech House, Boston, 2005.

[24] A. C. Cangellaris and D. B. Wright, "Analysis of the Numerical Error Caused by the Stair-Stepped Approximation of a Conducting Boundary in FDTD Simulations of Electromagnetic Phenomena," IEEE Trans. Antennas Propagat., Vol. AP-39, pp. 1518–1525, October 1991.

[25] R. Holland, "Pitfalls of Staircase Meshing," IEEE Trans. Electromagnetic Compatibility, Vol. 35, pp. 434–439, November 1993.

[26] T. W. Hertel and G. S. Smith, "Analysis and Design of Two-Arm Conical Spiral Antennas," IEEE Trans. Electromagnetic Compatibility, Vol. 44, pp. 25–37, February 2002.

[27] T. W. Hertel and G. S. Smith, "On the Dispersive Properties of the Conical Spiral Antenna and Its Use for Pulsed Radiation," IEEE Trans. Antennas Propagat., Vol. AP-51, pp. 1426–1433, July 2003.

[28] J. D. Dyson, "The Characteristics and Design of the Conical Log-Spiral Antenna," IEEE Trans. Antennas Propagat., Vol. AP-13, pp. 488–499, July 1965.

[29] K. L. Shlager, G. S. Smith, and J. G. Maloney, "Accurate Analysis of TEM Horn Antennas for Pulse Radiation," IEEE Trans. Electromagnetic Compatibility, Vol. 38, pp. 414–423, August 1996.

[30] R. T. Lee and G. S. Smith, "On the Characteristic Impedance of the TEM Horn Antenna," IEEE Trans. Antennas Propagat., Vol. AP-52, pp. 315–318, January 2004.

[31] R. T. Lee and G. S. Smith, "A Design Study for the Basic TEM Horn Antenna," IEEE Antennas Propagat. Magazine, Vol. 46, pp. 86–92, February 2004.

[32] K. L. Shlager, G. S. Smith, and J. G. Maloney, "Optimization of Bow-Tie Antennas for Pulse Radiation," IEEE Trans. Antennas Propagat., Vol. AP-42, pp. 975–982, July 1994.

[33] E. Chang, S. A. Long, and W. F. Richards, "An Experimental Investigation of Electrically Thick Rectangular Microstrip Antennas," IEEE Trans. Antennas Propagat., Vol. AP-34, pp. 767–772, June 1986.

[34] H. Abdallah, W. Wasylkiwskyj, K. Parikh, and A. Zaghloul, "Comparison of Return Loss Calculations with Measurements of Narrow-Band Microstrip Patch Antennas," ACES Journal, Vol. 19, pp. 184–186, November 2004.

[35] D. R. Jackson and N. G. Alexopoulos, "Simple Approximate Formulas for the Input Resistance, Bandwidth, and Efficiency of a Resonant Rectangular Patch," IEEE Trans. Antennas Propagat., Vol. AP-39, pp. 407–410, March 1991.

[36] S. Chebolu, R. Mittra, and W. D. Becker, "The Analysis of Microwave Antennas Using the FDTD Method," Microwave Journal, Vol. 39, pp. 134–150, January 1996.

[37] J. G. Maloney, P. H. Harms, M. P. Kesler, T. L. Fountain, and G. S. Smith, "Novel, Planar Antennas Designed Using the Genetic Algorithm," 1999 USNC/URSI Radio Science Meeting, Orlando, FL, p. 237, July 1999.

[38] J. G. Maloney, M. P. Kesler, P. H. Harms, T. L. Fountain, and G. S. Smith, "The Fragmented Aperture Antenna: FDTD Analysis and Measurement," Millennium Conference on Antennas and Propagation (AP 2000), Davos, Switzerland, 4 pages, April 2000.

[39] J. G. Maloney, M. P. Kesler, P. H. Harms, and G. S. Smith, Fragmented Aperture Antennas and Broadband Ground Planes, U.S. Patent No. 6,323,809 B1, November 27, 2001.

[40] L. N. Pringle, P. H. Harms, S. P. Blalock, G. N. Kiesel, E. J. Kuster, P. G. Friederich, R. J. Prado, J. M. Morris, and G. S. Smith, "A Reconfigurable Aperture Antenna Based on Switched Links Between Electrically Small Metallic Patches," IEEE Trans. Antennas Propagat., Vol. AP-52, pp. 1434–1445, June 2004.

[41] **[Incomplete reference: Balanis Antenna Engineering Handbook chapter — need full citation with chapter number, page range, edition, and year.]**